

1-1-1988

High resolution observations of the L1551, B335 and L723 bipolar molecular outflows using maximum entropy image reconstruction.

Gerald H. Moriarty-Schieven
University of Massachusetts Amherst

Follow this and additional works at: https://scholarworks.umass.edu/dissertations_1

Recommended Citation

Moriarty-Schieven, Gerald H., "High resolution observations of the L1551, B335 and L723 bipolar molecular outflows using maximum entropy image reconstruction." (1988). *Doctoral Dissertations 1896 - February 2014*. 1763.
https://scholarworks.umass.edu/dissertations_1/1763

This Open Access Dissertation is brought to you for free and open access by ScholarWorks@UMass Amherst. It has been accepted for inclusion in Doctoral Dissertations 1896 - February 2014 by an authorized administrator of ScholarWorks@UMass Amherst. For more information, please contact scholarworks@library.umass.edu.

UMASS/AMHERST



312066007696326

**High Resolution Observations of the
L1551, B335 and L723
Bipolar Molecular Outflows
Using Maximum Entropy Image Reconstruction**

A Dissertation Presented
by
Gerald H. Moriarty-Schieven

Submitted to the Graduate School of the
University of Massachusetts in partial fulfillment
of the requirements for the degree of
Doctor of Philosophy
February, 1988
Department of Physics and Astronomy

© Copyright by Gerald Henry Moriarty-Schieven 1988

All Rights Reserved

High Resolution Observations of the
L1551, B335 and L723
Bipolar Molecular Outflows
Using Maximum Entropy Image Reconstruction

A Dissertation Presented

by

Gerald H. Moriarty-Schieven

Approved as to style and content by:



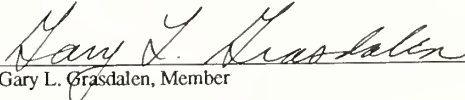
Ronald L. Snell, Chairman




Stephen H. Strom, Member



F. Peter Schloerb, Member



Gary L. Grasdalen, Member



Hajime Sakai, Member



R. B. Hallock, Department Head
Department of Physics and Astronomy

Acknowledgements

It is always difficult to thank all those who have helped to make a work such as this possible. One is always conscious that someone who should have been named will, in all likelihood, be left out. Nevertheless, I shall try to remember all who were most responsible.

Although my parents were never entirely sure what it was I was doing or why, they have always been most supportive and have always encouraged me to pursue my interests and to do it well. My achievements are their achievements.

My wife, Cindy, whom I met three days after arriving at UMass, and my daughter, Sasha, born nineteen months ago, have made life a continuous joy for me and have made all the trials of being a graduate student easy to bear.

To my fellow graduate students and friends among the faculty, post-docs and others, I pledge my eternal loyalty for their fellowship during my four and a half years here.

I am indebted to the Five College Radio Astronomy Observatory and to Bill Irvine, its director, for providing me with so much observing time, and for support during much of my time here. I also wish to thank the Department of Physics and Astronomy, and Steve Strom, for other support. I would like, in addition, to thank Steve Strom for suggesting this topic to me and for much valuable assistance and discussion.

Most of all, I wish to express my appreciation to Ron Snell, my advisor, who, more than anyone else, has been the guiding force behind this work. He has spent much effort in helping me through every stage, and has taught me the excitement and fun of research.

All of these, and many others, have made the time I've spent here the most enjoyable, exciting, fun, and wonderful period of my life (so far). I am fortunate to have them as family and friends.

"Powerless though I be to rise to the heavens of Thy glory and soar in the realms of Thy knowledge, I can but recount Thy tokens that tell of Thy glorious handiwork."

'Abdu'l-Bahá

ABSTRACT

**High Resolution Observations of the
L1551, B335 and L723
Bipolar Molecular Outflows
Using Maximum Entropy Image Reconstruction
February, 1988**

by

**Gerald H. Moriarty-Schieven
H.B.Sc., University of Western Ontario
M.Sc., Queen's University
Ph.D., University of Massachusetts**

Directed by

Ronald L. Snell

The application of maximum entropy image reconstruction to maps made at millimetre wavelengths to enhance their angular resolution, is discussed. We present complete maps of the high velocity ^{12}CO emission in the L1551 outflow, a map of the CS core of the L1551 molecular cloud, and a ^{13}CO map of the entire cloud. The molecular wind has been swept into a thin shell surrounding a cavity, and has broken out of the cloud at one position. Both lobes show an acceleration of high velocity emission away from IRS-5, caused by true acceleration produced by a hydromagnetically driven wind, or perhaps a geometric effect caused by a latitude dependent wind driving the molecular gas. The blue lobe experiences an abrupt narrowing and velocity decrease where it becomes recollimated. Red-shifted emission in the blue lobe and vice versa is likely due to an increased velocity

dispersion in these regions. The optical depth of high-velocity emission is larger than expected. The outflow mass may be more than $3.5M_{\odot}$. The energy within the outflow is greater than the total energy within the cloud. The outflow has sufficient momentum to disrupt the cloud core. The CS core shows no evidence for a rotating disk. Dense clumps exhibit shearing due to the outflow. Our data are most consistent with a model in which the molecular material is swept up by a high velocity, perhaps latitude dependent, wind originating near IRS-5.

The B335 outflow was also mapped and has structure similar to L1551. Limb brightening, and red-shifted emission in the center of the blue lobe and vice versa suggest a shell structure. The outflow is oriented $\sim 9^{\circ}$ out of the sky. The energy of the outflow is greater than that of the molecular cloud core, and there is sufficient momentum to disrupt the cloud core. The L723 outflow is very narrow and highly collimated, and has not been resolved by these observations. There is no evidence for a shell structure at this resolution. The outflow appears to have two axes of symmetry nearly perpendicular to each other, perhaps indicating that the outflow axis has precessed.

TABLE OF CONTENTS

Acknowledgements	iv
Abstract.....	vi
List of Tables	x
List of Figures	xi
Chapter	
1. Introduction.....	1
2. The Maximum Entropy Algorithm and the L1551 Molecular Outflow: An Expanding, Accelerated Shell.....	4
I Introduction.....	4
II Observations	5
III Image Reconstruction.....	7
IV Results.....	9
V Discussion.....	12
VI Summary	18
3. The Dense Core of the L1551 Molecular Cloud.....	44
I Introduction.....	44
II Observations.....	44
III Results.....	46
IV Discussion.....	48

4.	Structure and Kinematics of the L1551 Bipolar Molecular Outflow	61
	I Introduction	61
	II Observations	61
	a) ^{12}CO Observations	61
	b) ^{13}CO Observations	62
	III Results	63
	IV Optical Depths, Mass, and Energetics	66
	V Structure and Kinematics	75
	VI Summary	81
5.	The B335 and L723 Bipolar Molecular Outflows.....	100
	I Introduction	100
	II Observations	101
	III Results	101
	a) B335	101
	b) L723	105
	IV Mass and Energetics	108
	V Summary	111
6.	Summary	130
	I Maximum Entropy	130
	II Bipolar Outflows	131
	III Further Observations	133
Appendices		
	A. Derivation of the Maximum Entropy Algorithm.....	136
	B. Maximum Entropy FORTRAN Program	138
References	154

LIST OF TABLES

Table 2.1	Mass of High-Velocity Molecular Gas.....	13
Table 4.1	Mass of the L1551 Molecular Outflow.....	68
Table 4.2	Momentum and Energy in Outflow.....	72
Table 5.1	Mass, Energy and Momentum of B335 Outflow	109
Table 5.2	Mass, Energy and Momentum within the L723 Outflow	112

LIST OF FIGURES

Figure 2.1	The Regions mapped in the present study are shown as boxes superimposed on a contour map of the L1551 outflow as mapped by Snell and Schloerb (1985).....	21
Figure 2.2	Three point source profiles of relative strengths 30,60 and 120 were convolved with a gaussian beam profile of FWHP 45 arcsec and then reconstructed using the maximum entropy algorithm.....	23
Figure 2.3	This figure demonstrates the effect of increasing the value of λ on the effective resolution of the map.	25
Figure 2.4	A "true source profile" was generated with similar strength and size scales to the BLV image (see Figure 2.6).....	27
Figure 2.5	A simulated data set was generated by creating a "true" image (top left panel), then convolving it with a gaussian beam profile of FWHP of 45" and adding a normal distribution of noise such that the signal-to-noise was approximately 8 (shown in the second panel), a value slightly less than the S/N of the L1551 data.....	29
Figure 2.6	The broad, blue-shifted line wing was divided arbitrarily into four velocity intervals representing low velocity (BLV +3 to +5 km s ⁻¹), medium low velocity (BMLV, +1 to +3 km s ⁻¹), medium high velocity (BMHV, -2 to +1 km s ⁻¹), and high velocity (BHV, -5 to -2 km s ⁻¹) molecular gas.....	31
Figure 2.7	The images of each velocity interval (reference the caption to Figure 2.6) of the blue lobe of L1551 were reconstructed using the maximum entropy algorithm and are shown above as gray-scale images.....	33
Figure 2.8	The broad red-shifted line wing of the L1551 outflow was divided into four velocity intervals: RLV (+8 to +9 km s ⁻¹), RMLV (+9 to +11 km s ⁻¹), RMHV (+11 to +14 km s ⁻¹), and RHV (+14 to +18 km s ⁻¹).....	35
Figure 2.9	Shown is an I-band CCD image of the optical reflection nebula associated with the L1551 outflow, from Snell <i>et al.</i> (1985).....	37
Figure 2.10	The red and blue lobes were divided into six concentric, nested, parabolic shells or zones, three to four spectra wide.....	39
Figure 2.11	Shown opposite are three spatial-velocity diagrams made along cuts perpendicular to the flow axis at selected points along the axis of the blue lobe of the L1551 outflow.	41

Figure 2.12	A simple model was generated in which material was constrained to move along the walls of a cone with opening angle 50° and whose axis was inclined 15° out of the plane of the sky.....	43
Figure 3.1	A contour map of the reconstructed CS emission from the narrow ambient cloud spectral line, averaged over the interval 5.5 km s^{-1} to 8 km s^{-1} V_{LSR} is shown.....	52
Figure 3.2	Three artificial point sources with strengths similar to those found for features in the CS maps and with relative strengths 1, 2 and 4, were convolved with a 60 arcsec gaussian beam profile and were then reconstructed using the maximum entropy technique described in the article.....	54
Figure 3.3	These spatial-velocity diagrams were generated using spectra whose angular resolution was enhanced by maximum entropy.....	56
Figure 3.4	This spatial-velocity diagram was generated using the raw spectra (<i>ie.</i> those whose angular resolution has not been enhanced by maximum entropy.....)	58
Figure 3.5	This spatial-velocity diagram represents a cut running east-west (position angle -90°) through the peak located 0.8 arcmin south of IRS-5.....	60
Figure 4.1	Shown are halftone/contour maps of the blue- and red-shifted emission of the L1551 molecular outflow at different velocity intervals.....	85
Figure 4.2	The unreconstructed maps of the L1551 outflow are presented here.....	87
Figure 4.3	The reconstructed integrated antenna temperature (T_R^*) over the entire spectral line wing are displayed here as halftone/contour maps.....	89
Figure 4.4	The entire L1551 molecular cloud was mapped in ^{13}CO	91
Figure 4.5	Shown here are four spatial-velocity diagrams which have been generated from unreconstructed spectra of the outflow.....	93
Figure 4.6	This figure presents a comparison of ^{13}CO spectra with ^{12}CO spectra taken at the same position.....	95
Figure 4.7	The optical depths within the spectral line wings were calculated using the spectra presented in Figure 4.6 and are shown here, along with their standard errors, as a function of velocity interval and Y offset position.....	97
Figure 4.8	A simple kinematic model of the outflow is presented, where the molecular wind is being driven by a high-velocity, latitude dependent neutral wind.....	99
Figure 5.1	Displayed here are maps of the B335 bipolar outflow which were made by finding the integrated intensity ($\int T_R^* dv$) over the velocity interval indicated and were then reconstructed using maximum entropy.....	115

Figure 5.2	The raw, unreconstructed maps of the B335 outflow are shown in this figure.....	117
Figure 5.3	The integrated reconstructed intensity over the line wings from 3 to 7 km s ⁻¹ and from 10 to 14 km s ⁻¹ are presented.....	119
Figure 5.4	These spatial-velocity maps were made from the unreconstructed spectra along cuts through the outflow parallel to the outflow axis.....	121
Figure 5.5	In this figure are presented halftone/contour maps of the red-shifted and blue-shifted emission of the L723 molecular outflow at different velocity intervals..	123
Figure 5.6	The raw, unreconstructed maps of the L723 outflow are shown in this figure	125
Figure 5.7	The integrated intensity over the entire red- and blue-shifted line wings are presented here.....	127
Figure 5.8	Shown here are three spatial-velocity diagrams which have been generated from unreconstructed spectra of the L723 outflow.	129
Figure 6.1	The L1551 outflow has also been mapped by Uchida <i>et al.</i> (1987) using the Nobeyama Radio Observatory which has an angular resolution of 15" at the ¹² CO J=1-0 transition.....	135

Chapter 1

Introduction

It is now generally believed that most and perhaps all stars experience a stage of very energetic mass ejection during their evolution to the main sequence. This stage is often manifested by bipolar outflows of molecular gas. The study of bipolar molecular outflows provides an excellent means of probing these energetic mass ejections. Some outflows are known to have radio continuum or optical jets, but these are usually very weak and only detectable over short distances from the central star. The extent of this emission is typically of the order of arcseconds, and in the case of radio continuum emission, provides no kinematic information. Optical spectral lines from some young stellar objects provide velocities of the outflowing material, but it is very difficult to estimate the momentum and energy in the outflow. Some outflows have compact, shock-excited Herbig-Haro objects associated with them which often have velocities of 100 to 200 km s⁻¹, but these objects are small and provide only limited information about the wind. This mass loss phenomenon occurs when the young star is still deeply embedded in its parental material, and thus the energetic winds impact this predominantly molecular material and accelerates it. Emission from the accelerated molecular gas can be the most effective method to study the morphology and kinematics of these outflows. In the molecular clouds within which these presumably early stage young stellar objects are undergoing mass ejection, ¹²CO is ubiquitous and easily excited so that one can obtain morphological and kinematic structure within these outflows from near the origin to the end of the outflow. In addition, other molecules such as CS, which traces the dense molecular gas, can probe the dense gas in the vicinity of the young stellar object.

It is necessary, however, to have high angular resolution in order to resolve this structure. Even relatively nearby outflows have size-scales of a few arcminutes, while until recently the angular resolution of millimeter telescopes was about an arcminute.

Consequently, only the largest-scale structures could be seen in these outflows, and, lacking detailed knowledge of the geometry, the kinematics could be only crudely estimated and models for the structure only guessed at. Two different means are now available for improving angular resolution. Millimetre interferometers now in operation can provide very high resolution maps, but at the expense of losing the larger scale structure. An alternative method involves using a single dish telescope such as the Five College Radio Astronomy Observatory and then applying an image reconstruction technique to improve the angular resolution of the resultant maps. The technique used in this work is the Maximum Entropy Statistical Method (MESM) which was developed by Willingdale (1981) for use on X-ray images, and modified for use in infrared imaging by Grasdalen, Hackwell and Gehrz (1983). MESM is a non-linear inversion technique which fits a non-linear transform to a set of noisy, incomplete data, subject to the constraint that the "entropy" of an image (defined by entropy $S = -\ln I$) be maximized. In other words, the reconstructed image contains the minimum information or assumptions based on the raw data. In practise, the technique enhances the angular resolution of an image where the signal-to-noise ratio is large, while it provides smoothing without loss of resolution where the signal-to-noise is small to moderate. A derivation of the maximum entropy algorithm used is shown in Appendix A, a discussion of the use of the algorithm is found in Chapter 2, and the FORTRAN source code of the algorithm is presented in Appendix B.

Higher angular resolution observations, obtained through the use of maximum entropy techniques, will permit a better understanding of the geometry, and thus the morphological and kinematic structure of molecular outflows. In Chapter 2, high angular resolution maps of the inner few arcminutes of the L1551 bipolar molecular outflow are presented, and the kinematic structure seen is discussed. The dense core of the L1551 molecular cloud in the vicinity of the central star, L1551/IRS-5, was mapped at high angular resolution and the disruptive effects of the outflow on the cloud are discussed in Chapter 3. The entire L1551

outflow is presented in Chapter 4, and the overall morphology and energetics are examined. Chapter 5 contains high resolution maps of two other molecular outflows, B335 and L723, and their similarity to the structure seen in L1551 is discussed. A summary of the conclusions drawn by the study of these three outflows is presented in Chapter 6.

Chapter 2

The Maximum Entropy Algorithm

and

The L1551 Molecular Outflow: An Expanding, Accelerated Shell

I. Introduction

During the past decade, it has become clear that mass outflows represent an important phase in the lifetime of young stars. A significant fraction of these outflows appear to be bipolar (Lada 1985), presumably as a result of the interaction of collimated winds emanating from these young stars with ambient molecular gas. To date, most effort in studying outflows has been directed toward the discovery of molecular outflows and the measurement of their energy and momentum content. Little work has been done to describe the details of the velocity field and density structure of the molecular gas within the flow because, in most cases, the flows are not well resolved by filled aperture telescopes.

High spatial resolution studies offer the promise of a significant increase in our understanding of flow origin and propagation. Snell and Schloerb (1985) recently took advantage of a fortuitous lunar occultation of the bipolar outflow L1551 to obtain a high (7") resolution cut through the blue-shifted lobe. They observed a structure which they interpreted as an expanding, shell-like structure of molecular material swept up by a wind from the presumed source of the outflow, IRS-5. That this structure had not been suspected from lower resolution mapping emphasized the necessity of mapping these bipolar outflows at high spatial resolution.

The L1551/IRS-5 bipolar molecular outflow lends itself well to high resolution observations because of its proximity of 160 pc (Snell 1981) and hence large angular extent, and its prominent CO high velocity spectral line wings. These observations are essential to distinguish various proposed models such as: a) the expanding shell model of Snell, Loren and Plambeck (1980), in which a wind from a young star embedded in a

molecular cloud sweeps up ambient material into a shell which is itself expanding, or b) a hydromagnetic wind model (*eg.* Pudritz and Norman 1983) where a molecular wind is launched directly from a large, rotating, magnetized, molecular disk centred on a young stellar object. In addition, high angular resolution observations are necessary to compare in detail the molecular outflows with their optical counterparts, *ie.* optical jets or optical and infrared tracers of the wind/cloud interface (see Snell *et al.* 1985).

For this work, we have carried out higher spatial resolution observations of several nearby outflows. Our strategy involves heavily oversampling each beam area and then enhancing the spatial resolution using a maximum entropy statistical reconstruction method which is described in §III of this chapter. Although this technique is not competitive with millimetre interferometers in angular resolution, it does allow imaging of large regions at moderate resolution while maintaining an accurate determination of the total flux density. This chapter reports the first application of this technique to the central region of the bipolar outflow associated with L1551/IRS-5.

II. Observations

The bipolar nature of the L1551 outflow was first discovered by Snell, Loren and Plambeck (1980). The outflow, with angular dimensions of $\sim 24' \times 8'$, appears centered on an embedded young stellar object, L1551 IRS-5, which has a bolometric luminosity of $38 L_{\odot}$ (Emerson *et al.* 1984). The blue lobe extends 14 arcmin to the southwest (along position angle -135°) from IRS-5 while the red lobe extends 10 arcmin to the northeast (along position angle 45°) from IRS-5.

The observations presented in this chapter were obtained with the 14m telescope of the Five College Radio Astronomy Observatory in October and November, 1984 and January, 1985, using the $^{12}\text{CO } J = 1-0$ transition at 115 GHz. The beamwidth of the telescope at this frequency is well fit by a gaussian profile with FWHP of $45''$, as found by mapping 3C84 in azimuth and elevation several times during the observations. The L1551 outflow

was mapped by position-switching with a typical integration time of 20 seconds per spectrum, where the "off" source spectrum (located 60 arcmin west of IRS-5) was shared by many "on" source spectra. Samples were taken at 12 arcsec intervals along rows oriented in the sky perpendicular to the outflow axis. The mapped region encompasses an area of 6.4×5.4 arcmin (924 points) covering approximately one-half of the blue-shifted lobe of the outflow, as well as an area of 7.8×5.4 arcmin (1120 points) covering part of the red lobe. The areas mapped are shown in Figure 2.1 superimposed on a ^{12}CO map of the entire flow obtained by Snell and Schloerb (1985). The data were originally recorded using a 256 channel filterbank spectrometer with a resolution of 250 KHz (0.65 km s^{-1}), and later smoothed and resampled to a resolution of 1 km s^{-1} . The double sideband receiver temperature of the cooled mixed receiver, measured at the feed horn, was 70 K (Predmore *et al.* 1984). The calibration was accomplished using the standard chopper wheel method with an image sideband rejection filter in place throughout the observations. The antenna temperatures were corrected to the T_{R}^* temperature scale recommended by Kutner and Ulich (1981) assuming $\eta_{\text{FSS}}=0.7$. We have assumed that the outflow fills only the main beam, and have used the main beam efficiency, determined from measurements of the planets, to estimate the source coupling efficiency. An additional correction for the source coupling efficiency, estimated to be 0.72, has been incorporated into the computations of the column density and mass of high velocity gas emission.

The spectral lines of molecular outflow sources are characterized by broad wings, indicating the presence of high velocity molecular material. In most cases, maps are made by plotting the antenna temperature integrated over wide velocity intervals, a practice which, while locating the red and blue lobes of the flow, may hide interesting velocity and kinematic structure. The line wings for L1551 were divided into four velocity intervals, corresponding to low velocity (LV), medium-low velocity (MLV), medium-high velocity (MHV) and high velocity (HV) gas for both the blue-shifted (B) and red-shifted (R) lobes

of emission. Specifically, the blue-shifted lobe was divided into BLV (+3 to +5 km s⁻¹), BMLV (+1 to +3 km s⁻¹), BMHV (-2 to +1 km s⁻¹) and BHV (-5 to -2 km s⁻¹) velocity intervals, and the red-shifted lobe was similarly divided into RLV (+8 to +9 km s⁻¹), RMLV (+9 to +11 km s⁻¹), RMHV (+11 to +14 km s⁻¹) and RHV (+14 to +18 km s⁻¹) velocity intervals. The integrated antenna temperature (T_R^*) within each velocity interval was determined. Each map was then processed and reconstructed using the maximum entropy statistical method described below.

III. Image Reconstruction

The maximum entropy method has become an important tool in astronomy. As an image reconstruction technique, it has been demonstrated to be an effective means of recovering high spatial resolution from high signal-to-noise data which has been heavily oversampled over the beam area. Discussions of this technique are presented in the context of X-ray astronomy observations by Willingdale (1981), and in IR images of HII regions and young stellar objects by Grasdalen *et al.* (1983). A recent review of this technique has been presented by Narayan and Nityananda (1986).

The technique begins by mapping a region of interest with the radio telescope, oversampling heavily. In our case we chose to sample every 12 arcsec, giving us ~16 points per half power beam area of the telescope. The resulting map is then reconstructed. The maximum entropy solution is found by iterative solution of the transcendental equation

$$\mathbf{R} = \mathbf{N} \exp(\lambda (\mathbf{B} * \mathbf{D} - \mathbf{B} * \mathbf{B} * \mathbf{R})) \quad (2.1),$$

where \mathbf{R} is the reconstructed image, \mathbf{B} is the beam profile (a gaussian profile is used), \mathbf{D} is the raw data, $*$ is the convolution operator, \mathbf{N} is a normalizing constant to preserve flux constancy, and λ is a parameter used in the reconstruction process. This equation is derived in Appendix A. By solving this equation, we reconstruct the smoothest image consistent with the beam and raw data. It should be emphasized that, even with a moderate signal-to-noise ratio, the maximum entropy algorithm smooths the data without loss of

resolution where the signal-to-noise is moderate to large and returns only non-negative data points. The procedure involves starting at a low value of λ (the $\lambda = 0$ solution is a flat, constant flux image and is used as an initial trial solution), and gradually increasing λ with each solution (a listing of the FORTRAN source code for this procedure is presented in Appendix B). Increasing the value of λ effectively increases the resolution of the image solution. This is shown in Figure 2.2 where we show the results of a numerical simulation. The goal of the simulation was to recover a point source convolved with a beam profile by applying the maximum entropy algorithm. Plotted is the effective half-power beam-width (HPBW) of the reconstruction versus the parameter λ multiplied by the point source strength, for three point sources of strengths chosen to represent features in the L1551 maps. Because of the non-linearity of the maximum entropy algorithm, the rapidity with which a feature is reconstructed, and hence its effective angular resolution, depends on the strength of the feature multiplied by the parameter λ . Hence for a given value of λ , a strong feature will have a greater angular resolution than a weak feature, as can be seen in Figure 2.2. The effect of increasing the value of λ on a map can be seen in Figure 2.3.

An important consideration is the stopping point of the reconstruction process. When does increasing λ cause the solution to reconstruct noise rather than the true signal? This can be tested by creating a true source profile with similar strength and a priori structure size-scales to the L1551 bipolar outflow, convolving it with a beam profile similar to the beam profile of the telescope, and adding noise so that the signal-to-noise ratio in the simulated data is the same as in the real data to be tested. This we call the simulated "raw" data. A test of the maximum entropy algorithm was performed by reconstructing five different simulated raw data sets. The goodness-of-fit was tested by both comparing the chi-square between the simulated raw data and the reconstructed image convolved with the beam profile, and also comparing the chi-square between the true source profile and the

reconstructed image (Figure 2.4). For the former chi-square test (lower panel of Figure 2.4), in the case when no noise has been added to the simulated raw data, the chi-square vs. λ shows a continuous drop with increasing λ . When noise has been added to the simulated raw data, the chi-square drops steadily until the value approaches that of the added noise. For the comparison of the chi-square between the true source profile and the reconstructed image (upper panel of Figure 2.4), when noise has been added, the chi-square drops until a minimum value is reached, and then increases. Thus at this point, the maximum entropy solution is beginning to reconstruct noise and not the true source. Based on this numerical modeling, the reconstruction of L1551 was stopped at $\lambda = 12$, which gives us an effective beam-width of the reconstructed maps of about 20 arcsec for strong features, increasing the spatial resolution of our maps by a factor of 2. One of these model tests is presented in Figure 2.5. Shown are the "true" image, the simulated "raw" data which was created by convolving the "true" image with a 45" gaussian beam profile and adding noise, and the reconstructions of this "raw" data at increasing values of λ .

IV. Results

The raw and reconstructed data for the blue lobe are shown as gray-scale images, for the four velocity intervals defined earlier, in Figures 2.6 and 2.7. Each image has been auto-scaled so that the maximum intensity in each map is the same gray-scale level. Thus the raw BHV image appears the noisiest because the emission has been scaled by the largest factor. Because the maximum entropy algorithm generates spurious features at the abrupt edge of an incomplete map, the last four rows (which corresponds to the resolution of the telescope) have been removed from the reconstructed images. The images shown in Figures 2.6 and 2.7 are oriented such that "up" in the images is to the north-east (position angle 45°). The offsets for the images are relative to the position r.a.(1950) 04h28m40.6s, dec.(1950) 18°01'49". IRS-5 is located on the images at a point 0.2 arcmin (1 pixel) below the (0,0) offset position. The reconstructed red lobe is shown in Figure 2.8.

Comparison of the raw and reconstructed images of the blue lobe (shown in Figures 2.6 and 2.7) illustrates that all features present in the reconstructed images are visible in the raw data. The most striking feature in the reconstruction of the blue lobe is the distinct, parabolic, shell structure seen in the BLV gas, which is also apparent in the "raw images" (Figure 2.6). The higher velocity gas in the BMLV interval also shows a shell-like structure located within the outer shell and somewhat broader in width. The highest velocity BHV gas is found in the centre of the region where the BLV was weakest. The structure, therefore, appears as a series of concentric parabolic shells with the lowest velocity gas in the outermost shell and the highest velocity gas in the centre. We thus confirm the qualitative behavior reported by Snell and Schloerb (1985) and find that it persists over at least the inner $4' \times 6'$ region of the flow.

The BLV emission appears coincident with the bright edge of the optical reflection nebula. This is evident in Figure 2.9, in which a solid line representing the ridge of maximum intensity along the shell-like structure of the BLV emission is superimposed on an I-band CCD image of the L1551 nebula from Snell *et al.* (1985). Also shown as dotted lines are the half-power contour level of the ridge. The north-west edge of the bright optical nebula is well traced by the ridge and contours of the BLV emission and follows as well the spur near the west edge of the optical reflection nebula. The lower surface brightness south-east edge of the optical nebula (not easily visible) is almost as well traced by the BLV ridge.

Gray-scale images of the four velocity intervals for the reconstructed red lobe are shown in Figure 2.8. The orientation of these images is the same as the blue lobe; the (0,0) position of these images corresponds to r.a.(1950) $04^{\text{h}}28^{\text{m}}40.6$, dec.(1950) $+18^{\circ}01'33''$. IRS-5 is located on the images at a position 0.2 arcmin to the left of the (0,0) offset position. Overall, the red lobe has a similar morphological and kinematic structure to the blue lobe, but is much more fragmented and clumpy.

From Figures 2.7 and 2.8 it is apparent that where the highest velocity gas is dominant, the low velocity gas is almost absent. What is not so apparent is that there is weak high velocity gas throughout the outflow, even where the lowest velocity gas is dominant. In order to show the velocity structure in more detail, the red and blue lobes were divided into a series of six parabolic-shaped "zones" chosen to mimic the "shell" structure present. Zone 1 is a region three to four points wide which traces the outside edge of the red or blue lobe where the strong emission in the BLV and RLV intervals are found. Successive zones are nested, thin, parabolic regions, with zone 6 falling in the centre where the highest velocity gas is most prominent. All of the spectra within each zone were averaged together and plotted in Figure 2.10 with zone 1 at the bottom and zone 6 at the top. Also plotted for comparison is a spectrum of the ambient cloud, found by averaging spectra from a region where there was no evidence for high-velocity gas. Note the very smooth transition in profile shape from one zone to the next, and the striking symmetry between the spectra in the red and blue lobes. Although the red lobe has a more clumpy appearance, both the red and blue-shifted outflows must have similar overall kinematic structure.

Another feature of note in the BLV map are the pronounced undulations with angular period 1-2 arcmin (.05 - .09 pc at a distance of 160 pc). Similar undulations are more difficult to detect in the RLV because the red lobe is much more fragmented. The BMHV and BHV images show a much clumpier structure than does the lower velocity gas. Four prominent fragments can be identified in these images with sizes ~ 30 arcsec (.02 pc). These clumps are not obviously associated with optical knots or Herbig-Haro objects (Snell *et al.* 1985). A previous study of the CO emission in this outflow (Phillips *et al.* 1982) found indirect evidence that the flow may be clumpy with a filling factor of ~ 0.3 . Such clumpy structure and undulations are not surprising since the outflow is highly supersonic and the interstellar medium is very inhomogeneous.

It is interesting also to note that the position of IRS-5 is distinctly separate from the shell structure seen in both the BLV and RLV gas. IRS-5 lies between the two conical shells, separated by $\sim 30''$ to the blue-shifted shell, and $\sim 20''$ to the red-shifted shell. Thus, either there is no high velocity molecular gas within $20''$ of IRS-5, or the velocity of the outflow molecular material is low enough that it cannot be distinguished from the ambient cloud emission. In fact, the blue conical shell appears to originate from the end of the optical jet found by Mundt and Fried (1983), which can be seen in Figure 2.9.

The mass of molecular material within each velocity interval was calculated in a manner identical to that outlined by Snell and Schloerb (1985). It is assumed that the relative abundance of CO is 10^{-4} of H_2 and that the spectral line wings are optically thin. The computed mass estimates are presented in Table 2.1. The total mass of molecular wind observed is $\sim 0.24 M_{\odot}$, which is about one-quarter the mass of the entire flow observed by Snell and Schloerb (1985). Since Snell and Schloerb (1985) have shown that the optical depth in the line wings is greatest at low velocities, the masses calculated for the BLV and RLV intervals are most likely to be underestimated. However, even without any optical depth corrections, most of the mass of high velocity gas is restricted to the shell-like structure defined by the LV and MLV gas.

V. Discussion

The determination of the morphology and kinematics of the high velocity molecular gas in the L1551 outflow is one of the fundamental goals of this study. Two models for the structure of this outflow were described by Snell and Schloerb (1985) and differ primarily in the extent to which the lobes are filled with high velocity molecular gas. The first model that Snell and Schloerb considered is one in which the high velocity molecular emission arises from gas that fills the volume of the lobes and has a velocity structure such that the highest velocity gas is located at the center and is surrounded by successively lower velocity gas. This situation might arise if the molecular gas is entrained in a stellar wind

Table 2.1: Mass of High-Velocity Molecular Gas

<u>Velocity Interval</u>	<u>Blue Lobe</u>	<u>Red Lobe</u>
LV	.049 M_{\odot}	.042 M_{\odot}
MLV	.027	.041
MHV	.027	.027
HV	.010	.014

from IRS-5 and is decelerated at the boundary of the outflow. In the second model, the high velocity emission may arise entirely from a thin shell surrounding a cavity evacuated of molecular material and filled with the stellar wind from IRS-5. To reproduce the observed velocity structure in this latter model requires this shell to be expanding. In this picture the front and back sides of the shell are expanding toward us and away from us. One distinction between these two geometries is the distribution of low velocity outflowing gas. In the first model, the low velocity gas should be distributed throughout the lobe, while in the latter model the low velocity gas should be found only at the periphery of the lobe, where the expansion is tangential to the line of sight. The paucity of low velocity molecular gas toward the center of the lobe is illustrated both in the maps in Figures 2.7 and 2.8, and in the spatial-velocity maps (shown in Figure 2.11) which are made along cuts 1.2' and 2.2' from IRS-5 oriented perpendicular to the outflow axis.

There are many additional arguments to suggest that the molecular outflow forms a conical shell surrounding a mostly evacuated cavity. First is the presence of ultra-high-velocity ($>100 \text{ km s}^{-1}$) Herbig-Halo objects located near the central axis of the outflow (Cudworth and Herbig 1979). The acceleration and excitation of these objects must be a result of the direct impact of a high-speed wind that is possible only if this region is mostly evacuated of molecular material. Secondly, the optical reflection nebula HH102 (which appears to define the north-west rim of the region containing the blue-shifted high velocity gas), is consistent with being single-scattered light from IRS-5 as determined from polarization measurements by Draper *et al.* (1985). Furthermore, the colours of the reflected light from IRS-5, when compared with that expected for an illuminating star of spectral type K0 (as determined for IRS-5 by Mundt *et al.* 1985), demand that $A_V < 1$ magnitude along the paths from IRS-5 to HH102 (Stocke *et al.* 1987). Next, the largest column density of the outflowing molecular gas is found at the periphery of the outflow, as would be expected from a limb-brightening due to a shell. Finally, the coincidence of the

shell-like structure traced by the BLV gas with the outside edge of the optical reflection nebula (Figure 2.9) indicates that both are tracing the same wind/cloud interface. We conclude from these arguments that the bulk of the molecular wind is found in a shell surrounding a cavity probably filled with a much faster wind that arises from close to IRS-5.

Although we believe that the high velocity molecular gas is largely confined to a shell, there are still a number of phenomena which need to be explained. These include: 1) a systematic increase in the outflow velocity along the axis of the outflow away from IRS-5, 2) the segregation into parabolic shells of the emission at different velocities, in which the HV gas is found closest to the flow axis and the LV gas found closest to the limb of the outflow, 3) the separation of the BLV and RLV emission from IRS-5, and 4) the absence of strong red-shifted emission in the blue lobe and blue-shifted emission in the red lobe. These points can be explained qualitatively by a simple model in which molecular material is accelerated away from IRS-5 and is allowed to expand outward to form a conical shell similar to the models of Snell and Schloerb (1985) and Uchida *et al.* (1986). An example of such a model is shown in Figure 2.12. It was assumed that the opening angle of the cone was 50° , the cone was tilted toward the observer by 15° (Snell and Schloerb 1985), and the velocity of the gas increases linearly away from IRS-5 to a terminal velocity of 16 km s^{-1} . Figure 2.12 shows the iso-velocity contours for this model with respect to the velocity of the ambient cloud; the insert to this figure shows schematically the geometry assumed. Acceleration of the molecular gas then produces a systematic velocity increase with distance from IRS-5 as is observed, with the highest velocities found interior to the lowest velocities. The ambient cloud line profile has a FWHM of roughly 2 km s^{-1} , which would hide the slightly red-shifted emission from the backside of the shell and also the blue-shifted material found close to IRS-5. Alternatively, the molecular outflow may originate from the end of the optically visible jet, thus explaining the absence of high

velocity molecular emission near IRS-5. The striking similarity of kinematics and morphology between the red lobe and the blue lobe suggests that the same model will be applicable for both. Thus, there are many points in favour of such a model, although slightly different parameters or geometries could also be used to explain the data.

Although this model can adequately explain the morphology and kinematics of the outflowing gas, it does not provide an explanation for its origin. The high velocity molecular gas probably originated from either near IRS-5 and is part of molecular wind flowing from this star, or the gas may be primarily ambient cloud gas that has been swept up by a stellar wind from IRS-5. The mass of high velocity molecular gas of nearly $1 M_{\odot}$ (Snell and Schloerb 1985) is comparable to the total mass of the molecular disk ($2 M_{\odot}$) found by Kaifu *et al.* (1984), and considerably greater than the mass of the disk found by Strom *et al.* (1986). It seems unlikely that the mass of material near IRS-5 is sufficient to generate such a massive molecular wind. Instead, it seems more likely that most of the high velocity molecular gas is swept-up ambient cloud material. In fact, the mass of high velocity gas is consistent with the hypothesis that the outflowing molecular material is entirely composed of matter which has been swept out of the present-day cavity by a stellar wind from IRS-5.

If the high velocity molecular gas is ambient material swept up by a wind from IRS-5, what then is the origin of this wind? Several models have been proposed, such as pressure driven winds (Torbett 1984) in which the winds are driven by the thermalized orbital kinetic energy of accreting disk material, or hydromagnetic models (Pudritz and Norman 1983; Uchida and Shibata 1985) in which a large, rotating, magnetized disk hydromagnetically launches a wind from the disk surface, and accelerates it out to the Alfvén radius. The observed kinematics of the L1551 outflow seem to require an acceleration of material away from IRS-5, a conclusion that was also reached by Fridlund *et al.* (1984). Thus, to produce the gradual acceleration requires a force acting on the wind

material at great distances from IRS-5, which is precisely the prediction of the hydromagnetic model. Pudritz and Norman (1985) have applied their hydromagnetic model to a number of outflows, including that in L1551, and have made specific predictions on the properties of the disk and outflows in this source. As pointed out by Pudritz and Norman (1985) the most concrete test of their model is based on the prediction that the outflow will co-rotate with the disk out to the Alfvén radius, thus it is important to look for rotation of the outflow.

The spatial-velocity diagrams presented in Figure 2.11, which were constructed perpendicular to the outflow axis, should show the rotation of the outflow most readily. The cuts made at 0.2, 1.2, and 2.2 arcmin south-west of IRS-5 are all within the Alfvén radius, if the disk is as large as that found by Kaifu *et al.* (1984); thus the outflow should show rotation. The prediction by Pudritz and Norman (1985) of the disk rotation speed is 0.57 km s^{-1} ; therefore if the outflow co-rotates with the disk, the rotation speed should be greater due to its larger diameter. We attempted to measure the rotation of the outflow by determining the degree of asymmetry of the spatial-velocity diagrams at the two positions 1.2 and 2.2 arcmin south-west of IRS-5. The effect of rotation on the spatial-velocity diagram is discussed by Uchida *et al.* (1986), and is shown in Figure 2.11 of their paper. Examination of the spatial-velocity maps show that the high velocity blue-shifted gas looks quite symmetric above and below the outflow axis. We found no evidence for rotation of the outflow and set a three sigma limit on the rotational velocity of $\pm 0.3 \text{ km s}^{-1}$ and $\pm 0.6 \text{ km s}^{-1}$ at 1.2 and 2.2 arcmin from IRS-5 respectively. Thus, we can rule out the rotation of the outflow at the rate predicted by Pudritz and Norman (1985), although it is possible for the disk to be considerably smaller and thus have a smaller rotation rate and a smaller Alfvén radius, and consequently no observable outflow rotation. If, however, the molecular outflow is largely made up of swept-up ambient gas, it is not surprising that any signature of the putative origin of the wind (*e.g.* rotation) has been obscured within the

outflowing molecular material.

Uchida *et al.* (1987) have pointed out the presence of red-shifted gas in the blue lobe and blue-shifted gas in the red lobe. Examination of our data shows similar structure. Some of the red-shifted emission present in the blue lobe can be seen in the spatial-velocity map made 2.2 arcmin from IRS-5 (Figure 2.11). Unlike the interpretation of Uchida *et al.* who interpret this result as a signature of rotation, we believe these kinematic features are instead related to the overall asymmetry of the outflow. On the northern rim of the blue lobe and the southern rim of the red lobe the column density of high velocity gas and the velocity dispersion of this gas is the largest. In addition, it is in only these two regions that the high velocity CS emission has been detected (Snell and Schloerb 1985). We believe that the high velocity gas in this region has an unusually large velocity dispersion and is not related to the overall rotation of the flow. It is noteworthy that the jets as traced optically by Mundt and Fried (1983) and in radio continuum emission (Bieging, Cohen and Schwartz 1985) point toward these peculiar regions rather than along the axis of the larger scale molecular outflow.

VI. Summary

Portions of both the red and blue lobes of the L1551 bipolar outflow were mapped and images reconstructed using a maximum entropy algorithm. This technique has proven to be very successful in increasing the angular resolution of data obtained with the 14m radio telescope and should be generally applicable to the study of a number of problems related to the interstellar medium.

Morphologically, the L1551 outflow exhibits a shell-like structure, with the lowest velocity wind dominant along the limb of the flow, and the highest velocity wind dominant along the axis of the flow. The transition from low-velocity dominant region to high-velocity dominant region is smooth, and symmetrical between the red and blue lobes. The red-shifted flow has a similar morphological appearance to the blue-shifted flow, but is

much more fragmented.

We find that our data are consistent with a model in which the molecular material is primarily swept-up ambient gas concentrated into an expanding shell which is being accelerated away from IRS-5. The acceleration seems to proceed out to a distance of at least 4 arcmin (0.15 pc), which may be driven by a hydromagnetic wind from a disk surrounding IRS-5. Although we do not find evidence for rotation, this effect may be obscured.

Figure 2.1

The regions mapped in the present study are shown as boxes superimposed on a contour map of the L1551 outflow as mapped by Snell and Schloerb (1985). The broken contours represent the integrated antenna temperature (T_R^*) of the blue-shifted line wing (-5 to $+5$ km s $^{-1}$) and the solid contours, the integrated antenna temperature of the red-shifted line wing ($+8$ to $+18$ km s $^{-1}$). Contours are every 4.5 K km s $^{-1}$.

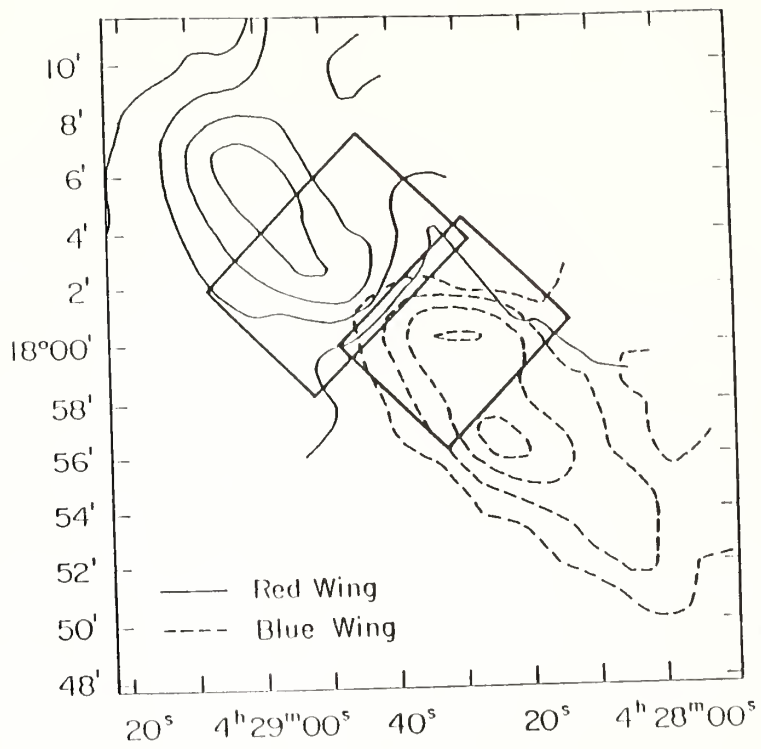


Figure 2.2

Three point source profiles of relative strengths 30, 60 and 120 were convolved with a gaussian beam profile of FWHP 45 arcsec and then reconstructed using the maximum entropy algorithm. The effective widths (in arcseconds) of these reconstructed point sources as a function of the parameter λ are plotted above. We conclude that the effective resolution of the L1551 reconstructions ($\lambda=12$) is approximately 20 arcsec.

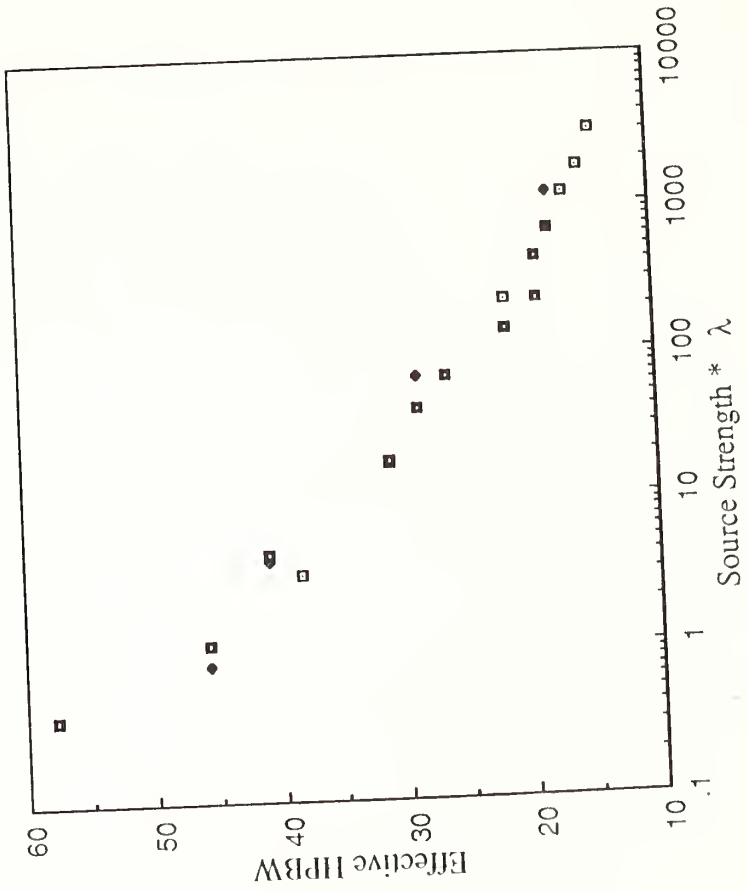


Figure 2.3

This figure demonstrates the effect of increasing the value of λ on the effective resolution of the map. Each map represents the 3 to 6 km s⁻¹ velocity interval of the B335 bipolar outflow (see Figure 5.1), reconstructed to a different value of λ . The contours are 0.25, 0.5, 1.0, 1.5, 2.0, ... K km s⁻¹. Note how increasing this value depresses the average background flux and sharpens the individual features in the map.

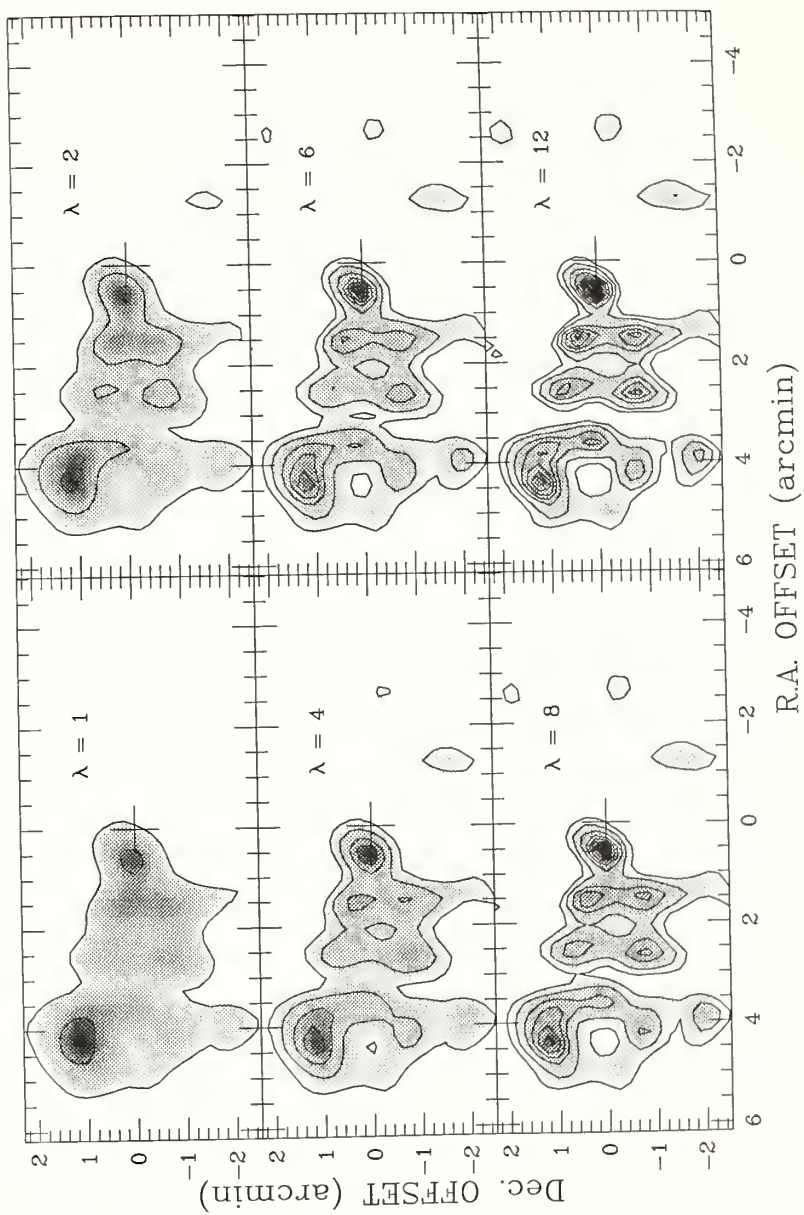


Figure 2.4

A "true source profile" was generated with similar strength and size scales to the BLV image (see Figure 2.6). This profile was convolved with a gaussian beam of FWHP 45 arcsec and artificial noise added (normalized to provide a similar signal-to-noise ratio to the BLV image), to generate several different "simulated raw data" sets; these artificial data were then reconstructed using the maximum entropy algorithm. The lower panel of this figure shows the chi-square of the simulated raw data compared to the reconstructions convolved with the beam profile. The lower branch corresponds to the case when no noise is added to the simulated data, and the upper branch corresponds to the cases when noise is added. The upper panel represents the chi-square of the "true source" compared to the reconstructed (noisy) data. Based on the above figure, our reconstructions were stopped at a value of $\lambda=12$.

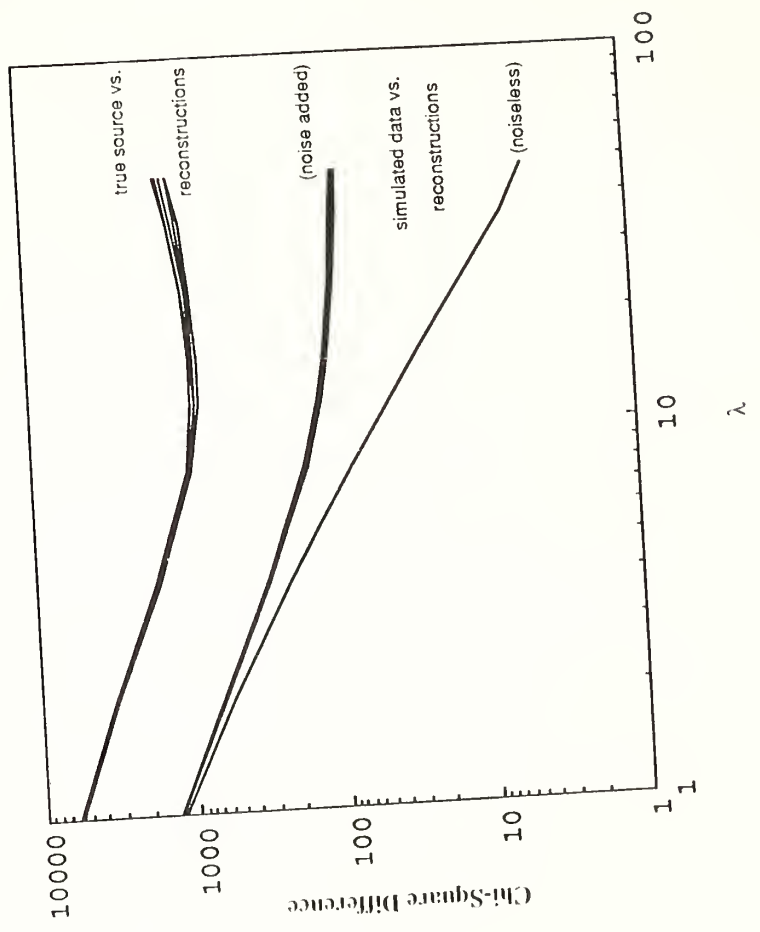


Figure 2.5

A simulated data set was generated by creating a "true" image (top left panel), then convolving it with a gaussian beam profile of FWHP of 45" and adding a normal distribution of noise such that the signal-to-noise was approximately 8 (shown in the second panel), a value slightly less than the S/N of the L1551 data. The simulated data set was then reconstructed using the maximum entropy algorithm described in the text. The resultant maximum entropy images as a function of λ are shown in the remaining panels.

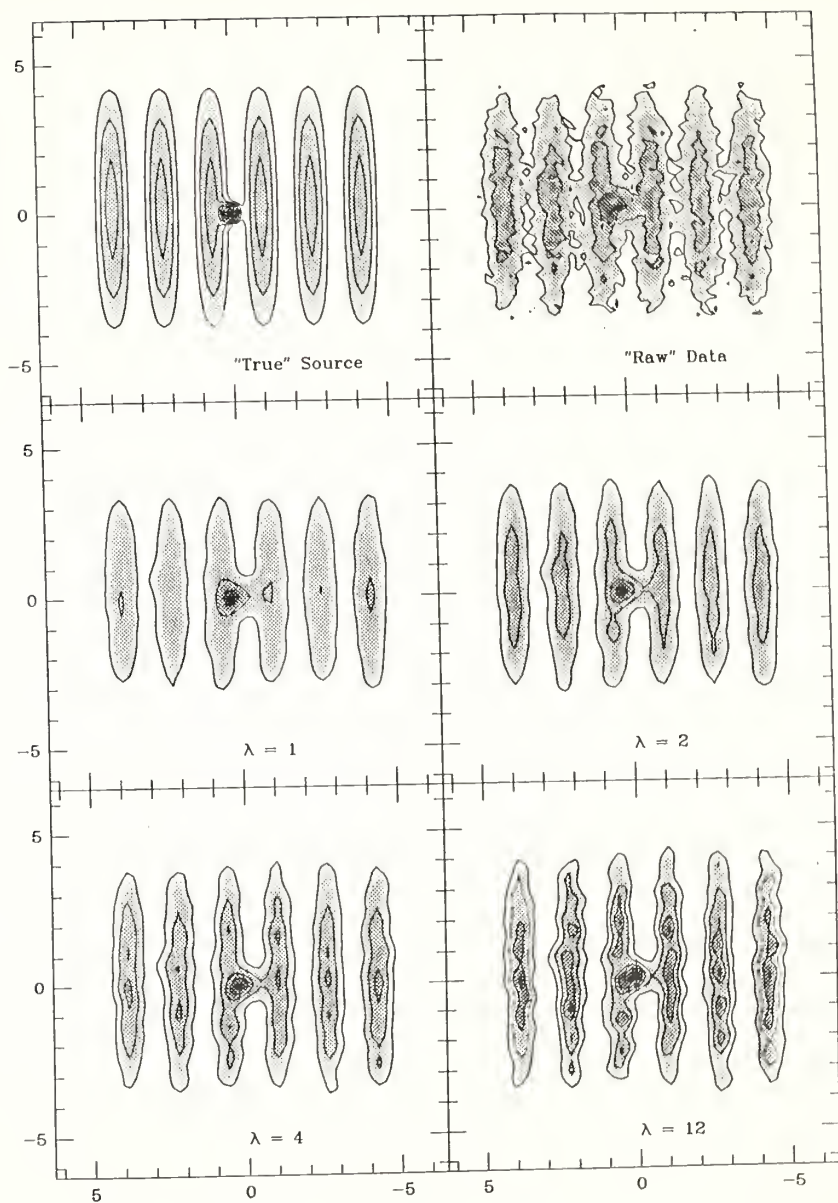


Figure 2.6

The broad, blue-shifted spectral line wing was divided arbitrarily into four velocity intervals representing low velocity (BLV +3 to +5 km s⁻¹), medium low velocity (BMLV, +1 to +3 km s⁻¹), medium high velocity (BMHV, -2 to +1 km s⁻¹), and high velocity (BHV, -5 to -2 km s⁻¹) molecular gas. The integrated antenna temperatures (T_R^*) within each velocity interval are displayed above as gray-scale images. Each image is scaled so that the pixel with the highest intensity is darkest. The values of the peak intensities are: BLV 14.5 K km s⁻¹, BMLV 8.1 K km s⁻¹, BMHV 13.1 K km s⁻¹, and BHV 5.7 K km s⁻¹. The (0,0) position of the images corresponds to r.a.(1950) 04h28m40.6s, dec.(1950) 18°01'49", and IRS-5 is offset 0.2 arcmin below this position. The top edge of the figure faces in the north-east direction (position angle 45°).

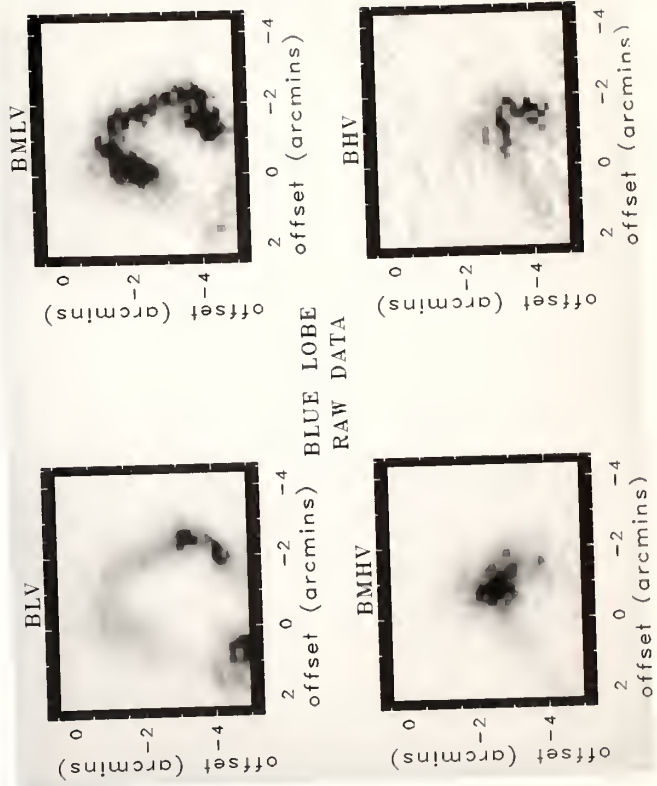


Figure 2.7

The images of each velocity interval (reference the caption to Figure 2.6) of the blue lobe of L1551 were reconstructed using the maximum entropy algorithm and are shown above as gray-scale images. Each is again scaled to the maximum value within each map. These values are: BLV 38.2 K km s⁻¹, BMLV 12.4 K km s⁻¹, BMHV 16.0 K km s⁻¹, and BHV 7.1 K km s⁻¹. Offsets are as in Figure 2.5. The four bottom rows of each image (corresponding to roughly one beamwidth) are not shown because of uncertainties in the reconstruction of the edges of the map. Note that all features visible in the reconstructed images are also present in the raw images, but are smoother and sharper. A number of important points are illustrated in these images. First, the HV gas is strongest in the regions where LV is weakest, secondly the velocity gradually increases further from IRS-5, and finally, the LV shell is distinctly separated from IRS-5. Also, the clumpy nature of the flow at all velocity intervals, and the pronounced undulations in the BLV image can be seen.

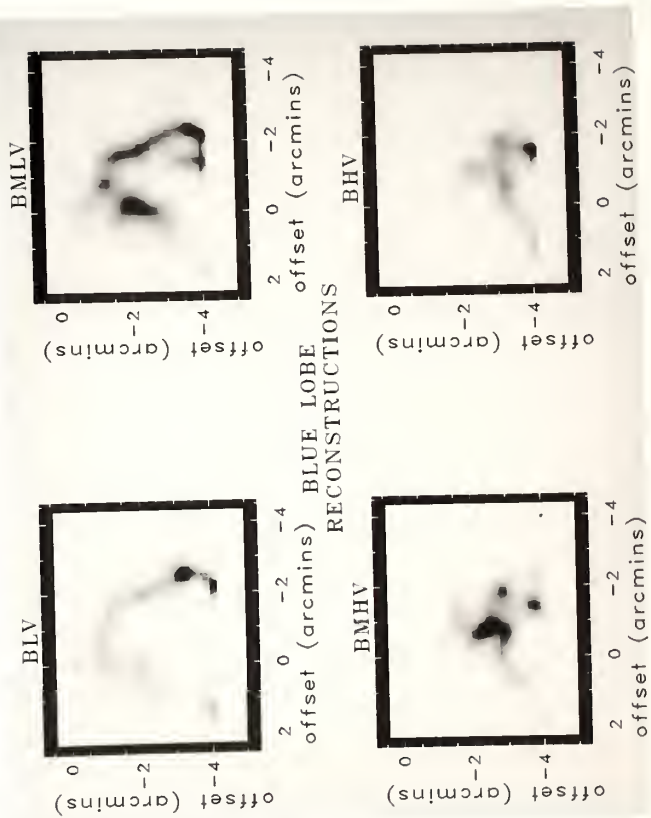


Figure 2.8

The broad red-shifted spectral line wing of the L1551 outflow was divided into four velocity intervals: RLV (+8 to +9 km s⁻¹), RMLV (+9 to +11 km s⁻¹), RMHV (+11 to +14 km s⁻¹), and RHV (+14 to +18 km s⁻¹). The integrated antenna temperatures (T_R^*) within each velocity interval were found, and the resultant images reconstructed using a maximum entropy algorithm. The reconstructed maps are shown above as gray-scale images, scaled to the maximum value within each map. These values are: RLV 16.7 K km s⁻¹, RMLV 21.2 K km s⁻¹, RMHV 19.1 K km s⁻¹, and RHV 9.1 K km s⁻¹. The (0,0) position of these images corresponds to r.a.(1950) 04h28m40.6, dec.(1950) +18°01'33", and IRS5 is offset from this position by 0.2 arcmin to the left. The top four rows of each image (corresponding to roughly one beam-width) are not shown because of uncertainties in reconstruction at the edges of the map. Note the similarity in morphology between the red and blue lobes, although the red lobe is much more fragmented.

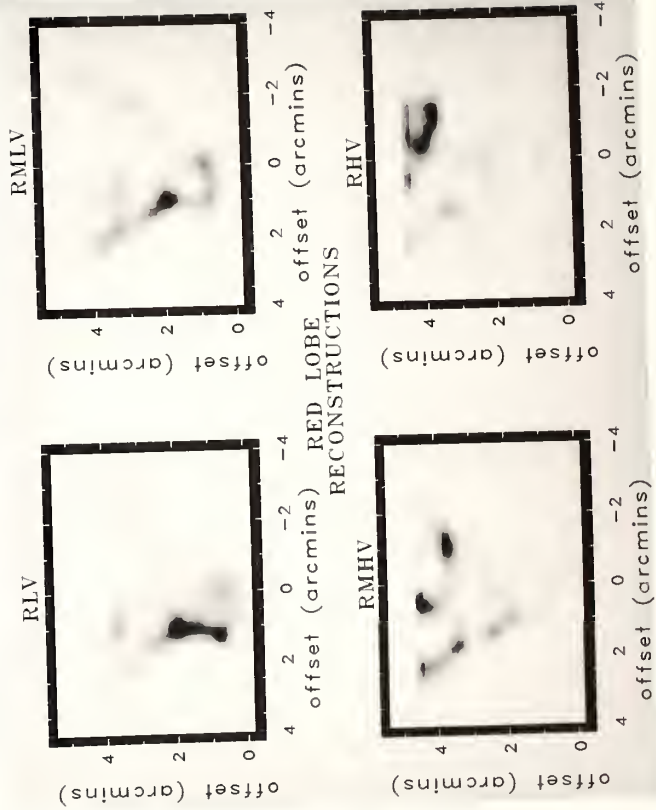


Figure 2.9

Shown is an I-band CCD image of the optical reflection nebula associated with the L1551 outflow, from Snell *et al.* (1985). Superimposed on this image is a solid line representing the "ridge" of maximum column density along the shell-like BLV feature (see Figure 2.7). The broken lines represent the half-power contour along the ridge.

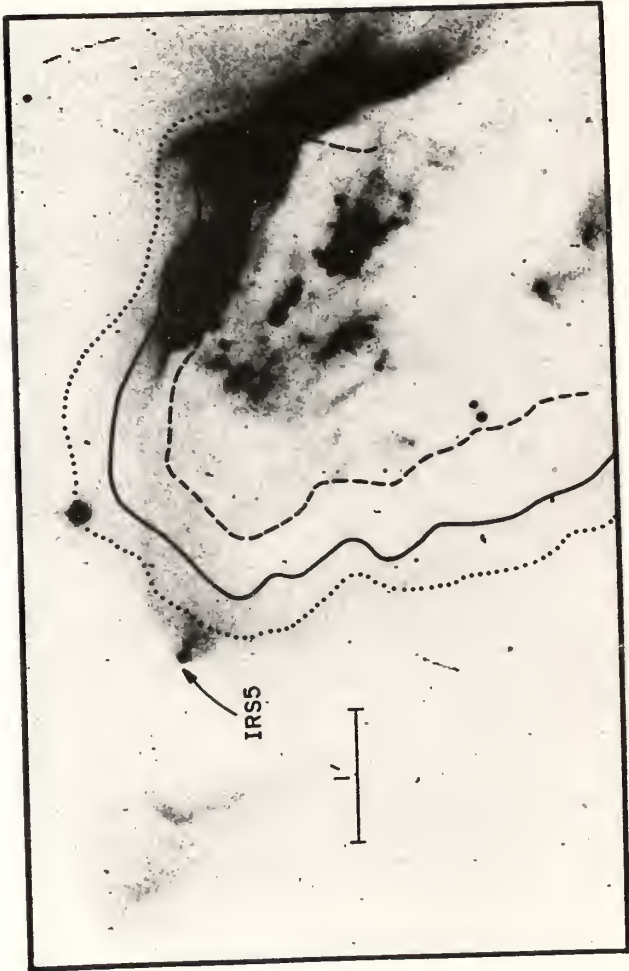


Figure 2.10

The red and blue lobes were divided into six concentric, nested, parabolic shells or zones, three to four spectra wide. Zone 1 corresponds roughly to the shell-like structure seen in the BLV and RLV images. Zone 2 forms a parabolic shell interior to zone 1 and each successive zone is nested within the previous shell. Zone 6 is found in the centre of the region where RHV and BHV are most prominent. All of the spectra within each zone were averaged and are plotted above. Also shown, superimposed on each zone spectrum, is an ambient line profile found by averaging many spectra located well away from the outflow. Antenna temperatures are T_A^* . Note the smooth transition from one zone to the next, and the presence of high-velocity gas in all zones.

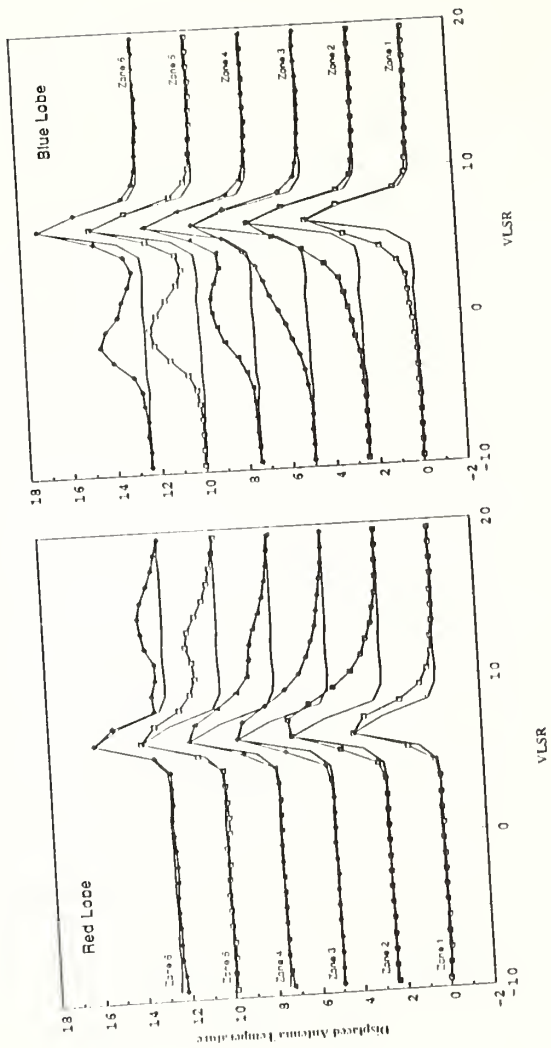


Figure 2.11

Shown opposite are three spatial-velocity diagrams made along cuts perpendicular to the flow axis at selected points along the axis of the blue lobe of the L1551 outflow. The cuts are made at 0.2, 1.2 and 2.2 arcmin south-west of IRS-5. Contour levels are at 0.5 K intervals. The blue-shifted line wing is nearly symmetric about the flow axis. Red-shifted gas in the blue lobe seems to be related to bright knots along the limb of the outflow, rather than to rotation.

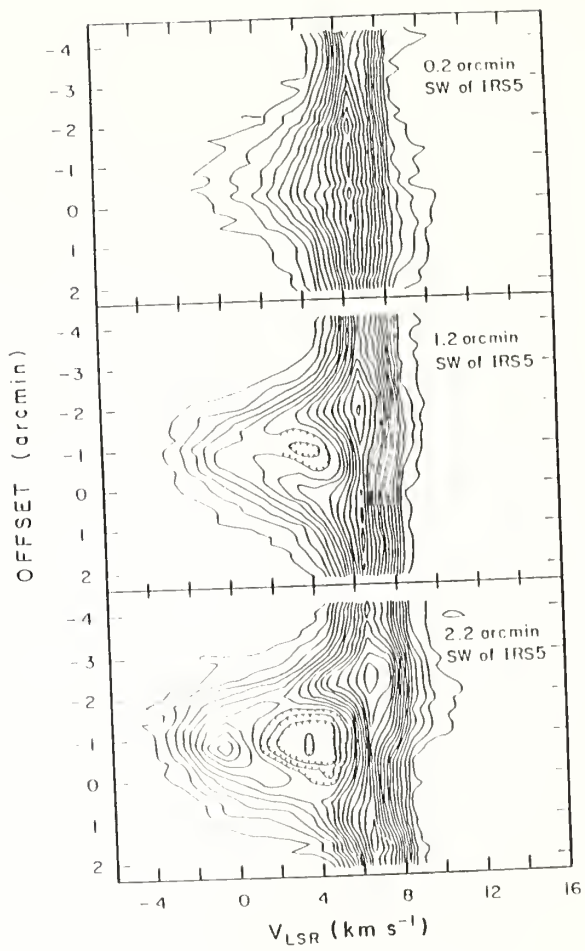
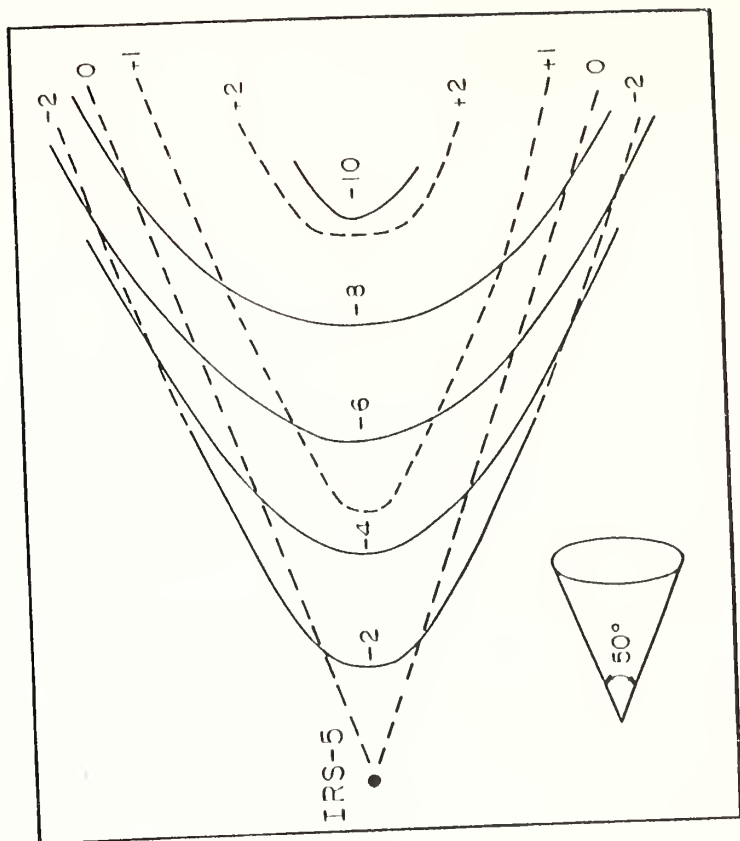


Figure 2.12

A simple model was generated in which material was constrained to move along the walls of a cone with opening angle 50° and whose axis was inclined 15° out of the plane of the sky. The material accelerates uniformly from rest to a terminal velocity of 16 km s^{-1} . Shown are iso-velocity contours for the front face of the cone (solid lines) and the back-side of the cone (broken lines). This simple model seems to account for the systematic increase in outflow velocity along the flow axis away from IRS5, the segregation into parabolic shells of emission at different velocities, in which the HV gas is found closest to the flow axis and LV found closest to the limb of the outflow, the separation of the BLV and RLV emission from IRS-5, and the absence of strong red-shifted emission in the blue lobe and blue-shifted emission in the red lobe.



Chapter 3

The Dense Core of the L1551 Molecular Cloud

I. Introduction

L1551/IRS-5, with its associated optical and radio jets, Herbig-Haro objects, and large-scale collimated molecular outflow, has served as a focal point for observational and theoretical studies of early stellar evolution and the origin and collimation of energetic mass outflows from young stellar objects. In their discovery paper, Snell, Loren and Plambeck (1980) suggest that the molecular outflow is confined and collimated by a circumstellar disk. Kaifu *et al.* (1984) claimed to have detected a 0.1 pc, rotating toroid with a mass of $2 M_{\odot}$ based on observations of the J=1-0 transition of CS obtained with an angular resolution of $33''$. This disk, oriented perpendicular to the molecular outflow, was found to have a rotation speed of 0.35 km s^{-1} . Batrla and Menten (1985), on the other hand, obtained observations of the same CS transition with similar angular resolution and claimed to find no evidence for rotation. Thus, the evidence for a large ($>0.1 \text{ pc}$) rotating disk around IRS-5 is at present uncertain. To resolve this confusing situation we have made a high angular resolution map of the J=2-1 CS emission over a much larger region surrounding IRS-5 than had previously been mapped. Our data surprisingly agrees with both Kaifu *et al.* (1984) and Batrla and Menten (1985). However, our more complete and thoroughly sampled CS maps cannot be interpreted in terms of a rotating disk.

II. Observations

The observations presented in this paper were obtained with the 14m telescope of the Five College Radio Astronomy Observatory in March through May, September and October of 1986. At the frequency observed (the CS J = 2-1 transition at 98 GHz), the telescope beamwidth is well fit by a gaussian profile with full width at half power of $60''$, which was found by observations of planets. The spectra for the L1551 cloud core map were obtained by position switching between the on-source position and the reference

position (located 60' west of IRS-5). Typical total integration times were 60 seconds for the on-source spectra and 120 seconds for the reference spectra. One reference spectrum was shared among ten on-source spectra. Spectra were obtained every 12 arcsec along rows oriented east-west in the sky (position angle 90°). The 1654 spectra thus obtained cover an area of $\sim 10' \times 7'$ approximately centered on IRS-5. The data were recorded using a 256 channel filterbank spectrometer with a resolution of 100 kHz ($.3 \text{ km s}^{-1}$). The double sideband receiver temperature of the cooled mixed receiver, measured at the feed horn, was 70 K. The calibration was accomplished using the standard chopper wheel method with an image sideband rejection filter in place throughout the observations. The antenna temperatures were corrected to the T_R^* temperature scale recommended by Kutner and Ulich (1981) assuming $\eta_{\text{FSS}}=0.7$.

A map of the CS emission was made by determining the average antenna temperature (T_R^*) over the narrow ambient cloud spectral feature (5.5 km s^{-1} to $8 \text{ km s}^{-1} V_{\text{LSR}}$) at each position. In addition, high velocity CS emission was found in the same two regions where it had previously been detected by Snell and Schloerb (1985). A map of high velocity red-shifted emission (8 km s^{-1} to $10 \text{ km s}^{-1} V_{\text{LSR}}$) and blue-shifted emission (3.5 km s^{-1} to $5.5 \text{ km s}^{-1} V_{\text{LSR}}$) were made in like manner. Each of these maps was reconstructed using the maximum entropy algorithm described in Chapter 2, to improve its angular resolution. Figure 3.1 is the reconstructed map of the ambient cloud emission (a) and the high velocity emission (b). Because of the non-linearity of the maximum entropy algorithm, the effective resolution of the reconstruction is a function of source strength and is not constant throughout the image. A number of point sources, with strengths chosen to represent typical strengths in the map, were convolved with a 60" gaussian beam and were then reconstructed using maximum entropy. The full-width at half maximum (FWHM) or effective resolution of the reconstructed point sources was determined. The effective resolution within the image is shown in Figure 3.2 as a function of reconstructed intensity

(in units of K). The strength of a feature (*ie.* the average antenna temperature at a feature peak) in the map in Figure 3.1 can thus be directly compared to Figure 3.2 to determine the effective resolution of the feature. From Figure 3.2, it can be seen that a point source with a similar intensity to the strongest features in the map has an effective resolution of approximately $30''$, an increase in resolution over the original data by a factor of two.

Maps at each of the 0.3 km s^{-1} channels were reconstructed to an effective angular resolution of approximately $30''$ using the technique described above. A total of 10 maps were made between 5 and 8 km s^{-1} . The spectra were then reassembled from these reconstructed maps and were used to generate the spatial-velocity diagrams of Figures 3.3 and 3.4.

III. Results

The reconstructed map of the CS emission distribution is shown in Figure 3.1a. Offsets are in arcminutes from IRS-5, and the map is oriented with north at the top and east to the left. The solid lines represent the average antenna temperature over the velocity interval of the ambient cloud line, 5.5 to 8.0 km s^{-1} , and Figure 3.1b shows the high velocity red-shifted emission (8.0 to 10.0 km s^{-1} , solid contours) and high velocity blue-shifted emission (3.5 to 5.5 km s^{-1} , broken contours). Most striking in this figure are the two peaks straddling IRS-5, similar to those reported by Kaifu *et al.* (1984). Our larger coverage shows additional features not seen by Kaifu *et al.*, including a ridge of emission which extends south-west from the northernmost peak near IRS-5 and which follows very closely the north-west limb of the blue-shifted lobe of the CO outflow, as well as the outside edge of the optical reflection nebula, HH102. The relationship between these features is shown in Figure 3.1c which contains a map of the inner part of the lowest velocity red- and blue-shifted CO lobes from Moriarty-Schieven *et al.* (1987b), and in Figure 3.1d which shows the optical reflection nebulae and Herbig-Haro objects. Although not forming as obvious a ridge, the bright CS emission east of IRS-5 is

coincident with the rim of the low velocity red-shifted CO emission.

High velocity blue-shifted CS emission (see Figure 3.1b) is found only in one small area within the south-westerly ridge, and is nearly coincident with the brightest clump of low velocity CO blue-shifted emission. The velocities of the CO and CS emission at this location are nearly the same: CO is at 3 to 5 km s⁻¹ and CS is at 3.5 to 5.5 km s⁻¹. This knot of high velocity CS emission is unresolved in the reconstructed map. It is interesting to note from Figure 3.1 that the barely resolved high velocity red-shifted CS emission (8 to 10 km s⁻¹) is also found nearly coincident with the brightest clump of low velocity CO red-shifted emission (8 to 9 km s⁻¹).

In order to address the question of rotation, spatial-velocity diagrams were generated, using the spatially enhanced spectra, in two cuts through IRS-5, one running north-south (position angle 0°) and the other running north-west to south-east (position angle -45°). These are shown in Figure 3.3. The spatial-velocity diagram in Figure 3.3a is oriented in the same direction as that of Kaifu *et al.* (1984) (*ie.* position angle 0°) and shows similar features to their Figure 3.4; between the north clump and south clump a velocity shift of 0.5 km s⁻¹ is found over a distance of 1.8 arcmin (.08 pc at a distance of 160 pc). The axis of the spatial-velocity map in Figure 3.3b is close to the axis of the disk proposed by Kaifu *et al.* (*ie.* at position angle -45°), and shows a velocity shift of -.4 km s⁻¹ over a distance of 2.5 arcmin (.12 pc), *ie. in the opposite direction*. Observations of Batrla and Menten (1985), who presented measurements showing no velocity gradient along an axis at position angle -30° (which is intermediate between the two maps in Figure 3.3), may be consistent with our data since the direction they chose falls between the direction in which we see a positive and then a negative velocity gradient.

It should be pointed out that velocity shifts are also seen in the raw spectra, *ie.* those whose angular resolution has not been enhanced by maximum entropy. Figure 3.4 shows the same spatial-velocity diagram as in the upper panel of Figure 3.3, except that in Figure

3.4 the raw spectra are used. It can be seen by comparing Figures 3.3 and 3.4 that by improving the angular resolution, maximum entropy has sharpened and elevated the two peaks, and has emphasized the velocity shift which is already visible in the raw spectra.

IV. Discussion

From Figure 3.3 it is clear that the velocity structure does not represent rotation of a massive disk around IRS-5. It is difficult to provide a limit on a rotational velocity since the motion is so chaotic. A massless disk orbiting a star of $1 M_{\odot}$ (believed to be roughly the mass of IRS-5) would produce a rotational speed at .05 pc from the star of $\sim 0.3 \text{ km s}^{-1}$. The velocity shear would then be $.6 \text{ km s}^{-1}$, which could easily be seen in our data, if present.

We must conclude from our data that we can find no evidence for a rotating disk. If a disk does exist, it must either be much smaller than $\sim 30 \text{ arcsec}$ (.024 pc) across (for example, a structure associated with the 2" disk reported recently by Strom *et al.* (1985) and Keene and Masson (1986)), or it may be large, but non-rotating. A difficulty with the former model is that peak emission is found on either side of IRS-5, and not toward the star. We have made measurements of the C^{34}S emission at eight positions around and on IRS-5 which show a similar morphology to that shown by the C^{32}S emission. Thus we believe that more molecular material is found in the location on either side of IRS-5 than toward the star. However, the beam size of a single dish measurement is 60 arcsec, so if a rotating disk is very small, it may not have been detected.

What, then, is the nature of the velocity structure seen in Figure 3.3? One possibility is that we are seeing shear within clumps in the L1551 cloud caused by the interaction of a supersonic wind moving past the denser, subsonic ambient cloud. A spatial-velocity map was made through a cut running east-west (position angle -90°) through the peak 0.8 arcmin south of IRS-5. This spatial-velocity map, shown in Figure 3.5, reveals a $\sim 1 \text{ km s}^{-1}$ gradient over the one arcmin size of this clump. Similar large velocity gradients are

also seen in the northern peak. These large velocity gradients seem better interpreted as shear motion rather than rapid rotation within each of the CS emission peaks. However, what appears as a smooth gradient may instead be multiple velocity components which have not been spatially resolved, though still suggestive of shear within this clump. As further evidence for shear, the high velocity blue-shifted CS emission is found nearly coincident with the brightest CO low velocity blue-shifted emission which itself is near a sharp bend in the CO shell structure, and the high velocity red-shifted CS emission is found nearly coincident with the brightest red-shifted CO clump. These clumps and bends in the CO emission may be manifestations of Kelvin-Helmholtz instabilities, as discussed in Chapter 2 and by Moriarty-Schieven *et al.* (1987b).

The ridge of CS emission tracing the outside edge of the blue-shifted lobe of the CO outflow (and coincident with HH 102), and the bright CS emission coincident with the bright red-shifted CO limb, indicate that high density gas borders the molecular outflow. It is at the size scale of this ridge that the molecular outflow seems to be recollimated (Snell, Bally, Strom and Strom 1985), and the dense CS emitting gas may be playing a role in confining the molecular outflow. It is interesting to note that the optical (Mundt and Fried 1983) and radio continuum (Cohen, Bieging and Schwartz 1982) jets are oriented nearly east-west, and are pointed almost directly into the bright north limb of the blue-shifted CO lobe and the bright south limb of the red-shifted CO lobe. These are also the locations of the high velocity CS emission, of the CS ridge, and the eastern CS clump. That these regions may be in the direct line of fire of the jets may explain the large velocity dispersion of the gas seen in both the CS and CO emission.

A question remains to be addressed about whether the density structure seen represents the primordial structure of the cloud or if it has been created by the outflow itself. A way to answer this is to ask if the present high density gas surrounding IRS-5 would be sufficient to collimate an initially isotropic flow. If we assume that the two dense

clumps on either side of IRS-5 are the two extremities of a torus, then the torus has an outer radius of ~ 1 arcmin (.05 pc) and an internal radius of $\sim .5$ arcmin (0.023 pc). If we further assume that the density within the torus is 10^5 cm^{-3} , then the total mass of material in the torus is $\sim 1 M_{\odot}$. If the present momentum flux of molecular material ($3 \times 10^{-4} M_{\odot} \text{ km s}^{-1} \text{ yr}^{-1}$, Snell and Schloerb 1985) were isotropic, then the momentum flux on the torus would be about $10^{-4} M_{\odot} \text{ km s}^{-1} \text{ yr}^{-1}$. During the lifetime of the wind, 4×10^4 years (Snell and Schloerb 1985), the present torus would itself have been accelerated to $\sim 4 \text{ km s}^{-1}$. Thus an initially isotropic wind could not have been collimated by the present "disk".

Thus it seems most likely that the present structure is *not* part of a rotating, collimating disk surrounding IRS-5. Instead, this structure may represent the remains of the dense gas from which IRS-5 was formed and which has been significantly altered over time by the L1551/IRS-5 outflow.

Figure 3.1

- (a) A contour map of the reconstructed CS emission from the narrow ambient cloud spectral line, averaged over the interval 5.5 km s^{-1} to $8 \text{ km s}^{-1} V_{\text{LSR}}$ is shown. Contours are every 0.3 K . The cross marks the location of IRS5. The coordinates represent the offset from IRS5 in arcmin. The region which was mapped is indicated by a thin line surrounding the contours. Note the two emission peaks straddling IRS5 and the south-westerly ridge of emission which corresponds closely to the limb of the low-velocity CO outflow emission, seen in (c).
- (b) The reconstructed high velocity CS emission is shown in this panel. Contours are every 0.3 K . The solid contours represent the average antenna temperature over the interval 8 km s^{-1} to 10 km s^{-1} , and the broken lines over the interval 3.5 km s^{-1} to 5.5 km s^{-1} . The lowest contour of the CS ambient cloud emission, shown in panel (a), is also indicated. Note that the high velocity emission is found only at the location of the brightest clumps of the low velocity CO red- and blue-shifted emission, seen in panel (c).
- (c) The reconstructed maps of the lowest velocity component of the bipolar molecular outflow are shown here from Moriarty-Schieven *et al.* (1987b). Solid contours represent the reconstructed red-shifted CO emission, integrated over the velocity interval from 8 km s^{-1} to 9 km s^{-1} , and the broken contours are the reconstructed blue-shifted emission, integrated over the interval 3 km s^{-1} to 5 km s^{-1} . Contours are every 2 K km s^{-1} .
- (d) This schematic diagram shows the location of some of the optical features of the IRS5 bipolar outflow, including the optical jet extending west-south-west from IRS5, the emission feature HH 29, and the reflection nebula HH 102, which may represent the wind/cloud interface. The outline of the CS emission is also shown.

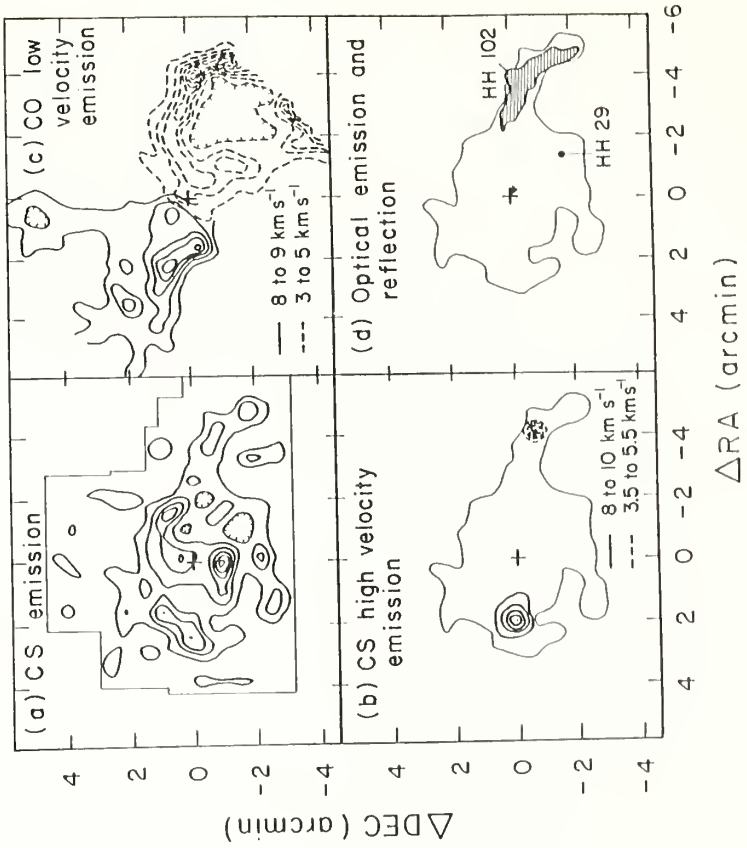


Figure 3.2

Three artificial point sources with strengths similar to those found for features in the CS maps and with relative strengths 1, 2 and 4, were convolved with a 60 arcsec gaussian beam profile and were then reconstructed using the maximum entropy technique described in the article. The effective angular resolution of the reconstructed point sources was found as a function of the reconstructed strength (in units of K) and is plotted above. The effective resolution of a feature in the reconstructed CS maps whose peak strength is 1.5 K is thus ~ 30 arcsec.

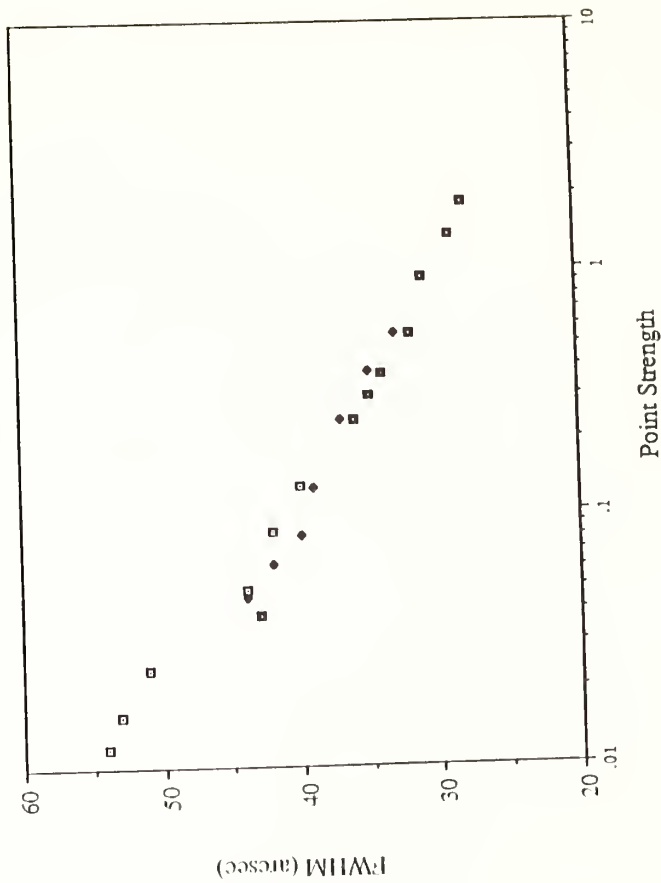


Figure 3.3

These spatial-velocity diagrams were generated using spectra whose angular resolution was enhanced by maximum entropy. The contours are at every 0.3 K. The offsets are in arcmin from IRS5. The top panel (a) represents a cut through IRS5 running north-south, *ie.* at position angle 0° , the same orientation as that presented by Kaifu *et al.* (1984). The lower panel (b) represents a cut through IRS5 running at position angle -45° , which is roughly through the axis of the proposed disk of Kaifu *et al.* Note that while (a) shows a velocity shift of 0.5 km s^{-1} over a distance of 1.8 arcmin, (b) shows a velocity shift of -0.4 km s^{-1} over a distance of 2.5 arcmin, *ie.* in the opposite direction.

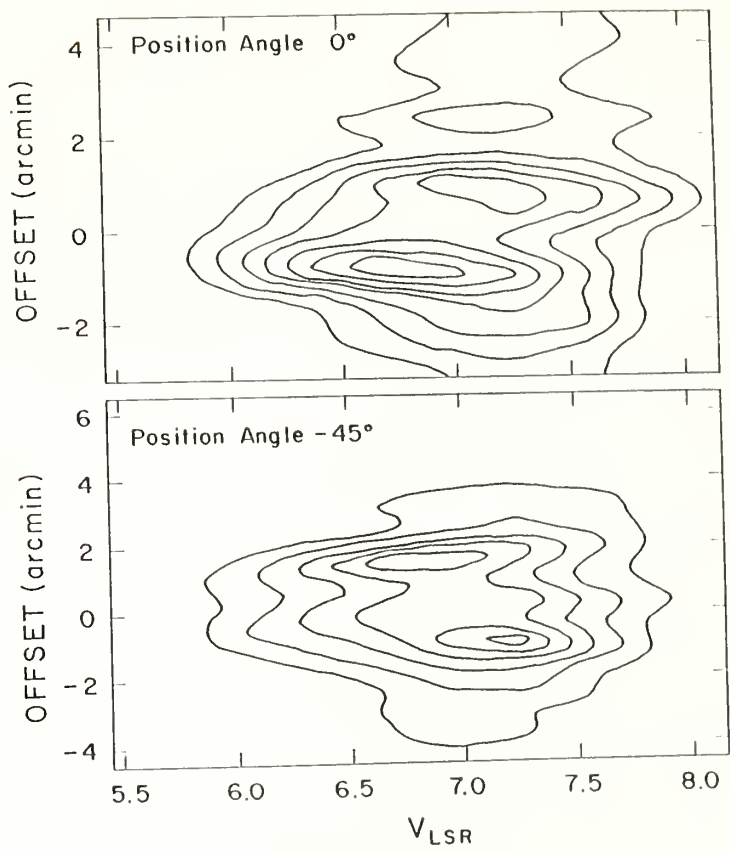


Figure 3.4

This spatial-velocity diagram was generated using the raw spectra (*ie.* those whose angular resolution has not been enhanced by maximum entropy). The orientation of this diagram is the same as that of the upper panel of Figure 3.3, *ie.* position angle 0° . Contours are every 0.3 K. A similar velocity shift to that seen in Figure 3.3a is also visible here. The RMS noise in the individual spectra is typically 0.2 K per channel.

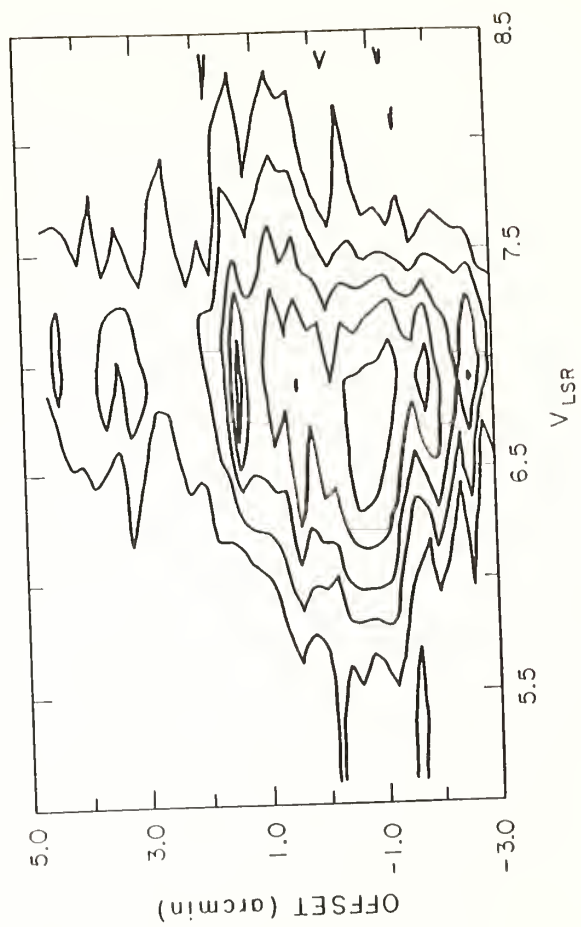
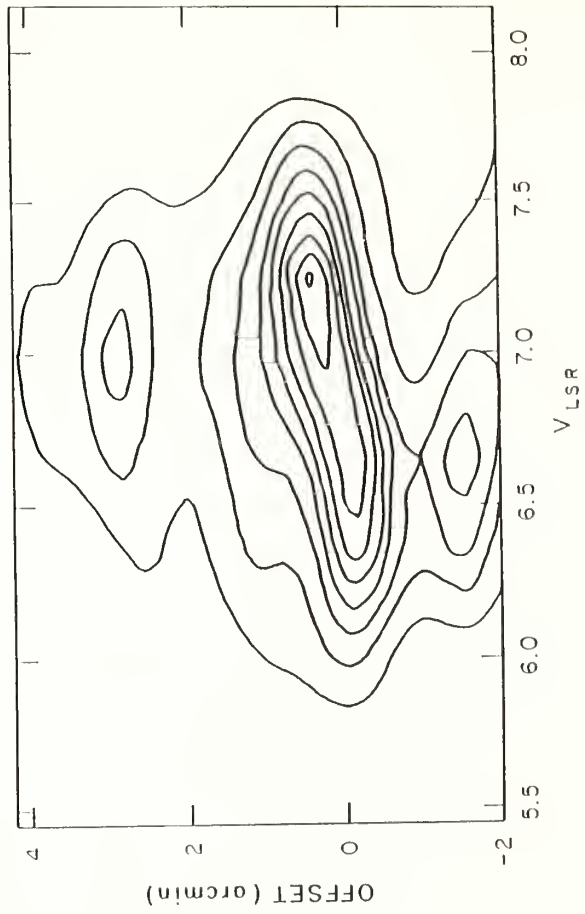


Figure 3.5

This spatial-velocity diagram represents a cut running east-west (position angle -90°) through the peak located 0.8 arcmin south of IRS-5. Offsets are in arcmin from the position (0.0,-0.8), and contours are at every 0.3 K. This figure clearly shows the large velocity gradient of $\sim 1 \text{ km s}^{-1}$ over the small size ($< 1 \text{ arcmin}$) of the clump. A similar gradient is seen in the other clump north-west of IRS-5.



Chapter 4

Structure and Kinematics of the L1551 Bipolar Molecular Outflow

I. Introduction

In Chapter 2, maps of the inner few arcminutes of the L1551 outflow were presented and discussed. In this chapter, maps of the entire outflow will be presented. In addition, ^{13}CO observations of the entire cloud and of specific locations within the outflow will be presented. These observations will be used to determine the structure of the entire outflow, its mass, and the effect of the outflow on the molecular cloud in which it is embedded.

II. Observations

a) ^{12}CO Observations

The observations presented in this paper were obtained at the 14m telescope of the Five College Radio Astronomy Observatory in 1984 through 1986. The entire outflow, a region covering roughly $10' \times 30'$, was mapped in the ^{12}CO J=1-0 transition at 115 GHz. The 6904 spectra covering the L1551 outflow were obtained as described in Chapter 2.

In order to understand better the velocity structure of the L1551 outflow, the high velocity emission was broken up into six velocity intervals in each red-shifted and blue-shifted wing. These intervals were chosen somewhat arbitrarily, to enhance the different kinematic structures found within the outflow. For convenience, the intervals are labeled B1, R1, B2, R2, *etc.*, indicating the blue-shifted and red-shifted emission at successively higher velocities from line center, beyond the ambient cloud velocity range of 5 to 8 km s⁻¹. The intervals are: B1 (4 to 5 km s⁻¹), B2 (3 to 4 km s⁻¹), B3 (1 to 3 km s⁻¹), B4 (-1 to 1 km s⁻¹), B5 (-4 to -1 km s⁻¹), B6 (-9 to -4 km s⁻¹), R1 (8 to 9 km s⁻¹), R2 (9 to 10 km s⁻¹), R3 (10 to 12 km s⁻¹), R4 (12 to 14 km s⁻¹), R5 (14 to 17 km s⁻¹), R6 (17 to 23 km s⁻¹). The integrated antenna temperature, T_R^* , was found within each velocity interval at each position, and a map was made for each interval. Each map was then reconstructed

using a maximum entropy algorithm, described in more detail in Chapter 2, to enhance the angular resolution. As is discussed in Chapter 2, the reconstructed angular resolution of the strongest features in our maps is approximately 20 arcsec. These reconstructed maps are presented in Figure 4.1, while the unreconstructed maps are shown in Figure 4.2. The long axis of these maps is oriented north-east to south-west, *ie.* along position angle 45° . The offsets are measured in arcmin from the position of IRS-5, located at $\alpha(1950)$ $4^{\text{h}}28^{\text{m}}40.1^{\text{s}}$, $\delta(1950)$ $18^\circ01'41.2''$, which is indicated on the maps by a large cross. Right ascension and declination offsets in arcminutes from IRS-5 can be calculated from the X and Y offsets in arcminutes in the maps using the simple transformation:

$$\alpha(\text{offset}) = (X\text{offset} + Y\text{offset}) \sin(45^\circ) \quad (4.1)$$

$$\delta(\text{offset}) = (X\text{offset} - Y\text{offset}) \sin(45^\circ) \quad (4.2).$$

These maps show the average antenna temperature within each velocity interval, rather than the integrated antenna temperature. The integrated intensity in each velocity interval can be found by multiplying the average antenna temperature by the velocity width of each interval.

Maps of the total integrated intensity in the blue (-9 to 5 km s^{-1}) and in the red (8 to 23 km s^{-1}) are presented in Figure 4.3. The maps were produced by adding up the emission in the twelve reconstructed velocity intervals.

b) ^{13}CO Observations

The entire L1551 molecular cloud (covering approximately $40' \times 40'$) was mapped in the ^{13}CO J=1-0 transition at 110 GHz. The 1400 spectra covering the molecular cloud were spaced by 1 arcmin along rows oriented east-west (position angle 90°) in the sky. The total integration time per point was 30 seconds, sharing one reference integration with several on-source integrations as was done for the ^{12}CO outflow data. The data were recorded using a 256 channel filterbank spectrometer with a resolution of 100 kHz (0.27 km s^{-1}). An integrated intensity map (5 to 8 km s^{-1}) of the L1551 molecular cloud is

shown in Figure 4.4. The horizontal axis of this map is oriented east-west (position angle 90°), unlike the ^{12}CO maps, and the offsets are in arcmin from the position of IRS-5, located on the map by a cross. The emission west of R.A. offset ~ -20 and north of Dec. offset $\sim +4$ is moving at a velocity approximately 1.5 km s^{-1} greater than the L1551 cloud, and may be a separate cloud.

A series of high signal-to-noise spectra were obtained in the ^{13}CO $J=1-0$ transition at 110 GHz along a line running perpendicular to the outflow axis and located 2.4 arcmin south-west of IRS-5. For these spectra the total integration time was 8 minutes per point. The same reference position was used for all observations of L1551.

III. Results

A number of the features visible in the maps in Figures 4.1 and 4.3 have already been discussed in Chapter 2, which showed only the inner part of the outflow extending to $\pm 4'$ from IRS-5. In Chapter 2 it was pointed out the "shell-like" structure seen in the low velocity outflowing gas (see maps of the B1, B2, R1 and R2 velocity intervals in Figure 4.1) and the apparent acceleration of material away from IRS-5 (manifested as a monotonic increase in velocity away from IRS-5). In Chapter 2 these structures were interpreted as indicating that the molecular material is located in a thin expanding shell that is being accelerated as it moves away from IRS-5. Such structure has also been seen in maps made of this outflow in the $J=1-0$ transition by Uchida *et al.* (1987) and in the $J=2-1$ transition by Rainey *et al.* (1987). Both Uchida *et al.* and Rainey *et al.* have also modeled the outflow as a shell-like structure. Also seen in the inner part of the outflow is low velocity redshifted gas on the northern boundary of the blue lobe and blueshifted low velocity gas located on the southern edge of the red lobe (see maps of the R1 and B1 velocity intervals). This structure has been interpreted by Uchida *et al.* (1987) as evidence for rotation of the lobes as predicted by the hydromagnetic models of Uchida and Shibata (1985) and Pudritz and Norman (1983). An alternative explanation will be discussed later.

The maps of the total integrated intensity in the red- and blue-shifted gas (Figure 4.3) show an overall extent to the outflow of 29' or 1.3 pc at the distance of L1551 of 160 pc (Snell 1981). The blue lobe of the outflow extends about 18' (0.8 pc) south-west from IRS-5 and the red lobe about 11' (0.5 pc) north-east of IRS-5. The "shell-like" structure is not so obvious in the total integrated intensity maps but is quite apparent in the maps of the lower velocity emission. The low velocity emission which traces the "shell" is found at the periphery of the outflow and surrounds the emission at the higher velocities (B4, B5, B6, R4, R5, and R6). The emission seen in the velocity interval B1 is also coincident with the bright edge of the optical reflection nebula (see Chapter 2, Moriarty-Schieven *et al.* 1987b, and Snell *et al.* 1985), which is thought to represent the interface between the outflow and the ambient molecular cloud.

In the blue lobe, low and medium velocity emission (B1, B2, B3, and B4) extend to the end of the outflow, but the highest velocity emission (B5 and B6) extends only to about 6' (0.2 pc) from IRS-5. All velocities in the red lobe, however, extend to the end of the outflow at about 9' from IRS-5. Low velocity emission extends across the end of the outflow, completing the shell of low velocity emission that surrounds the presumed cavity and probably represents the point where the molecular shell is presently being driven into the cloud. The abrupt end of the outflow marking this interface with the cloud is especially evident in the spatial-velocity maps of Figure 4.5, where at Y offset = -2.4', -1', and 0', the outflow is seen to extend to an X offset -13' and +9' for the blue and red lobes after which emission at all high velocities abruptly vanishes.

The spatial-velocity map for Y offset +1.6', however, does not show an abrupt edge in the blue lobe, and in fact, emission beyond 7' from IRS-5 appears to be undergoing a gradual acceleration. It is noteworthy that beyond 7' from IRS-5, the ambient emission becomes much weaker, and beyond 15' nearly disappears even though high-velocity emission is still present. The map of the total (reconstructed) intensity in the blue-shifted

line wing in Figure 4.3 shows the large extent of the weak high velocity emission at a Y offset of +1.6'.

The overall morphology of the outflow can be traced in the R1 and B1 velocity maps which determines of the outer boundary of the flow. In the inner few arcminutes of both the red and blue lobes, the outflow appears to have a nearly constant opening angle of about 70° . In the blue lobe, this opening angle decreases slowly out to about 4' to 6' from IRS-5, after which the sides become parallel and, in fact, the outflow becomes narrower. The red lobe, on the other hand, displays no such recollimation and appears to have a nearly constant 70° opening angle to the end of the outflow. The apparent acceleration, which in both the red and blue lobes seems to be confined to the region where the outflow is opening outward, can clearly be seen in the spatial-velocity maps presented in Figure 4.5. The upper-right panel in Figure 4.5 shows a spatial-velocity map made along a slice through the symmetry axis at a Y offset of -1'. This figure shows the nearly linear increase in velocity away from IRS-5 reaching a maximum velocity roughly 5' from IRS-5 in both directions. At roughly this distance in the blue-shifted emission, the maximum velocity drops abruptly. As can be seen in Figure 4.1, the location of the abrupt velocity decrease occurs exactly where the outflow sharply narrows. It is beyond this velocity discontinuity that the outflow becomes recollimated. A few of the contours of the Figure 4.3 maps have been drawn to scale on the inset of Figure 4.4, which shows a map of the entire L1551 molecular cloud as traced by ^{13}CO . The entire outflow takes up a significant fraction of the cloud; the red lobe appears to end close to the edge of the cloud, as does the blue lobe, but the weak emission extending to X offset -19' is beyond the edge of the cloud as seen in ^{13}CO . The highest column density emission of the cloud (as traced by the integrated antenna temperature of ^{13}CO , which, assuming the emission is optically thin, is proportional to the column density of the molecular gas in the cloud) is located along a ridge extending to the west of IRS-5, and is coincident with the north-west limb of the blue

lobe of the outflow. Another region of large column density to the east of IRS-5 is similarly coincident with the south-east limb of the outflow's red lobe. These regions are also the locations of the red-shifted emission which is found in the blue lobe, and the blue-shifted emission in the red lobe. As reported in Chapter 3 (and by Moriarty-Schieven *et al.* 1987a), CS emission is also found in a ridge along the north-west limb of the blue lobe, indicating that this high column density ridge has also a high spatial density. A column density minimum in the molecular cloud is located coincident with the interior of the blue lobe

Another region of blue-shifted emission in the red lobe around X offset +5.5, Y offset -2.5 is possibly not associated with the L1551/IRS-5 outflow, but instead with either HL or XZ Tau (located in Figure 4.1 by crosses at X and Y offsets (+4.9,-3.4) and (+5.2, -3.2) respectively) as first suggested by Calvet, Canto and Rodriguez (1983). If this emission does originate from HL or XZ Tau, then the blue-shifted emission is oriented toward the south-east (position angle $\sim 135^\circ$), close to the direction of the red-shifted optical jet. This finding is in agreement with the results of Levreault (1985) and Torrelles *et al.* (1987). It is interesting to note that the highest velocity molecular wind (seen in B3) is distinctly separated from HL Tau and from XZ Tau by approximately 1 arcmin. It is difficult to distinguish the red-shifted emission from the L1551/IRS-5 outflow from that of HL and XZ Tau because of the overlap of the two flows. This is especially evident in the spatial-velocity maps of Figure 4.5, where in the Y offset = -2.4 map, the high velocity blue-shifted emission from HL/XZ Tau, and the much more extended red-shifted emission principally from IRS-5, can be seen at X offset +5'.

IV. Optical Depths, Mass, and Energetics

We can make an estimate of the mass of the L1551 molecular cloud based on our ^{13}CO observations. From a number of C^{18}O spectra obtained in the central few arcminutes of the cloud where the strongest ^{13}CO emission is found, the ratios of $^{13}\text{CO}/\text{C}^{18}\text{O}$ are

consistent with optically thin emission assuming terrestrial abundances of the isotopic species. Assuming an abundance of molecular hydrogen relative to ^{13}CO of 10^6 , an excitation temperature of $T_{\text{ex}} = 10\text{K}$, and using the method described in Snell *et al.* (1984), we have calculated the mass of the L1551 molecular cloud to be $49 M_{\odot}$. This is consistent with the mass of $42 M_{\odot}$ for the L1551 molecular cloud found by Snell (1981). Assuming a spherical geometry for the cloud and a radius of $15'$ (0.7 pc at 160 pc), the average density of the cloud would be $n \sim 800 \text{ cm}^{-3}$. In reality, the density peaks near IRS-5 and appears to decrease roughly as the square of the distance (Snell, 1981; and see Figure 4.4).

The mass of molecular gas involved in the bipolar outflow has also been estimated assuming the emission is optically thin and in LTE. Mass estimates assuming an excitation temperature of 25K (Phillips *et al.* 1982, Rainey *et al.* 1987) are presented in Table 4.1, although values assuming $T_{\text{ex}} = 35\text{K}$, 15K , and 10K are also tabulated. An uncertainty in T_{ex} results in a large range of column densities, and for the extremes in T_{ex} tabulated in Table 4.1, the column density (and hence mass) varies by nearly a factor of three. Table 4.1 illustrates the effect of T_{ex} on the mass determined. The mass of red-shifted wind is approximately $.6 M_{\odot}$, of blue-shifted wind is $\sim .7 M_{\odot}$, and the total mass of molecular wind is $1.3 M_{\odot}$. Taking into account the higher T_{ex} used in these calculations, this value for the mass is consistent with the value of $\sim 0.9 M_{\odot}$ found by Snell and Schloerb (1985).

The assumption that the emission from the outflow is optically thin is, however, not a good one. A number of ^{13}CO spectra were obtained with sufficiently high signal to noise to detect the high velocity emission, along a cut made through the outflow perpendicular to the outflow axis, and situated 1.8 arcminutes south-west of IRS-5 (X offset $-1.8'$). In Figure 4.6 they are shown compared to the ^{12}CO spectra at the same location. These spectra were used to obtain estimates of the optical depths within the spectral line wings, by assuming that the ^{13}CO spectra were optically thin and that the isotopic ratio of $^{12}\text{CO}/^{13}\text{CO}$

Table 4.1: Mass of the L1551 Molecular Outflow

<u>Velocity Interval</u>	<u>Mass</u> <u>35 K</u> <u>(thin)</u>	<u>Mass</u> <u>25 K</u> <u>(thin)</u>	<u>Mass</u> <u>15 K</u> <u>(thin)</u>	<u>Mass</u> <u>10 K</u> <u>(thin)</u>	<u>Mass</u> <u>25 K</u> <u>($\tau=2.6$)</u>
B1 (4 to 5 km s ⁻¹)	.27 M _⊙	.21 M _⊙	.14 M _⊙	.11 M _⊙	.58 M _⊙
B2 (3 to 4 km s ⁻¹)	.17	.13	.09	.07	.36
B3 (1 to 3 km s ⁻¹)	.20	.15	.11	.09	.43
B4 (-1 to 1 km s ⁻¹)	.12	.09	.06	.05	.25
B5 (-4 to -1 km s ⁻¹)	.08	.06	.04	.03	.17
B6 (-9 to -4 km s ⁻¹)	.03	.03	.02	.01	.07
R1 (8 to 9 km s ⁻¹)	.30 M _⊙	.23 M _⊙	.16 M _⊙	.13 M _⊙	.65 M _⊙
R2 (9 to 10 km s ⁻¹)	.13	.10	.07	.06	.28
R3 (10 to 12 km s ⁻¹)	.14	.11	.07	.06	.30
R4 (12 to 14 km s ⁻¹)	.09	.07	.05	.04	.20
R5 (14 to 17 km s ⁻¹)	.07	.06	.04	.03	.16
R6 (17 to 23 km s ⁻¹)	.04	.03	.02	.02	.09
Total -9 to 5 km s ⁻¹	.87 M _⊙	.66 M _⊙	.46 M _⊙	.37 M _⊙	1.85 M _⊙
Total 8 to 23 km s ⁻¹	.79 M _⊙	.60 M _⊙	.42 M _⊙	.33 M _⊙	1.68 M _⊙
Total Mass of Outflow	1.66 M _⊙	1.26 M _⊙	.88 M _⊙	.70 M _⊙	3.54 M _⊙

is 60. Then

$$\frac{\sum T_{R_{12CO}}^*}{\sum T_{R_{13CO}}^*} = \frac{60}{\tau_{12CO}} \left(1 - e^{-\tau_{12CO}} \right) \quad (4.3).$$

The optical depths were so calculated as a function of velocity and Y offset position and are presented in Figure 4.7. It is apparent from Figure 4.7 that the emission in the high velocity line wings is not optically thin, and is in fact quite large, especially at the periphery of the outflow at the lower velocities (3 to 5 km s⁻¹). If the ratio of the ¹²CO to ¹³CO abundance is not 60, as assumed, but closer to the terrestrial ¹²CO/¹³CO ratio of 89, then the optical depth will be somewhat greater.

From Figure 4.7 it can be seen that the optical depth for the low velocity emission (B1 and B2) is greater than at higher velocities and greater at the limb of the outflow. Thus, the shell structure would be more pronounced than is indicated by the maps in Figure 4.1 and 4.3 if it were not for optical depth effects. From the ratio of the ¹³CO column densities at the center of the outflow to the edge, an estimate of the thickness of the shell at this position can be made. Using this ratio of column densities derived from the ¹³CO spectra over the entire line wing (-5 to 5 km s⁻¹) of ~3, and assuming a cylindrical geometry, then the thickness of the shell is only about 0.2 that of the radius of the shell. At X offset -1.8', the shell thickness would be about 0.026 pc. This is probably an upper limit to the shell thickness, since we are limited by the resolution of the telescope in determining this ratio.

Because of the large optical depths, the mass of high velocity gas has been significantly underestimated in the past (Snell, Loren and Plambeck 1980; Snell and Schloerb 1985). A better estimate of the mass would take into account the optical depth as a function of velocity and position. However, because we have such optical depth

information only along one particular cut through the outflow, and these values vary so significantly even within one velocity interval along the cut, that such a treatment would be hazardous. Instead we have estimated an average optical depth of $\tau=2.6$ from the median value over the -5 to 5 km s^{-1} interval, and have applied a correction to the calculated mass over the entire outflow at all velocity intervals using this value. The corrected masses are summarized in Table 4.1. The total mass of molecular wind in the outflow, based on this correction, is over $3.5 M_{\odot}$, nearly three times as much mass as when calculated assuming an optically thin emission. Since most of the mass is found in the limb of the outflow at low velocities where the optical depth is much greater, the total mass of the outflow could be as much as ten times greater than previously estimated. Conversely, the optical depth could be much lower through a large fraction of the outflow, and so the mass of $3.5 M_{\odot}$ could also be an upper limit. Nevertheless, it is difficult to conceive how so much mass could have originated from even as large a disk as the one of $2 M_{\odot}$ proposed by Kaifu *et al.* (1984). Instead the vast bulk of the molecular wind could only be material which has been swept out of the cavity.

The mass of molecular gas which is involved in the outflow is not an insignificant fraction of the mass of the entire L1551 cloud. Even assuming that the emission is optically thin, the outflow mass is nearly 3% of the mass of the cloud, and when the optical depth of the outflow emission is taken into account, this fraction increases to 7% or more. It is more difficult to estimate the fraction of the volume of the cloud taken up by the outflow, since the third dimension of the map of the cloud is unknown. Assuming, however, a spherical geometry for the cloud (and the ^{13}CO map in Figure 4.4 supports such an assumption) with a radius of $15'$, and that the outflow is a cylinder of radius $3'$ extending through the centre of the cloud, then the outflow takes up about 6% of the volume of the cloud. The similarity in the fraction of the cloud taken by the outflow in terms of mass and volume supports the hypothesis that the molecular wind is largely

material which has been swept out of a cavity the size of the outflow. The large fraction of mass and volume in the outflow suggests that the outflow must be having a major disruptive effect on the cloud. This disruption can be witnessed in the map of the molecular cloud in Figure 4.4, where the column density minimum surrounded by the ridge of high column density material, which is coincident with the blue lobe of the outflow, shows how material has been swept out of a cavity into a shell. The molecular cloud core shows even greater signs of being disrupted by the outflow (Moriarty-Schieven *et al.* 1987a; Chapter 3).

The energy and momentum content of the outflow can be estimated for each velocity interval, and these values are presented in Table 4.2, assuming optically thin emission, and using only the radial component of the outflow velocity. In addition, the kinetic energy of the molecular cloud has also been estimated using the mean turbulence velocity of the ambient gas from the ^{13}CO line profiles and assuming a mass of $49 M_{\odot}$; this value is also presented in Table 4.2. The total momentum and energy in the outflow was found to be $5.6 M_{\odot} \text{ km s}^{-1}$ and 3.6×10^{44} ergs respectively. The outflow kinetic energy, uncorrected for the inclination of the outflow and for optical depth effects, is half that of the entire cloud, 7.3×10^{44} ergs, and when the optical depth correction of $\tau=2.6$ is made, the energy in the outflow becomes of the same order of magnitude or greater than that of the molecular cloud, at 1.0×10^{45} ergs. Taking into account the inclination of the outflow to the line of sight, the energy in the outflow will be almost certainly greater than that of the entire L1551 molecular cloud. The total (optical depth corrected) momentum in the outflow is probably not sufficient to entirely disperse the cloud, since the escape velocity from the molecular cloud is $\sim 0.8 \text{ km s}^{-1}$ while the total momentum of the outflow, if conserved and shared by all the mass, could accelerate the entire cloud to a velocity of 0.3 km s^{-1} . Nevertheless, this momentum is more than sufficient to disrupt the core of the cloud and delay further star formation, and much of the presently outflowing molecular gas has more than enough

Table 4.2: Momentum and Energy in Outflow

<u>Velocity Interval</u>	<u>Velocity^a</u> (km s ⁻¹)	<u>Mass^b</u> (M _⊙)	<u>Momentum</u> (M _⊙ km s ⁻¹)	<u>Energy</u> (ergs)
B1 (4 to 5 km s ⁻¹)	-2.2	.21	.46	1.02 x 10 ⁴³
B2 (3 to 4 km s ⁻¹)	-3.2	.13	.42	1.33 x 10 ⁴³
B3 (1 to 3 km s ⁻¹)	-4.7	.15	.71	3.31 x 10 ⁴³
B4 (-1 to 1 km s ⁻¹)	-6.7	.09	.60	4.04 x 10 ⁴³
B5 (-4 to -1 km s ⁻¹)	-9.2	.06	.55	5.08 x 10 ⁴³
B6 (-9 to -4 km s ⁻¹)	-13.2	.03	.40	5.23 x 10 ⁴³
R1 (8 to 9 km s ⁻¹)	1.8	.23	.41	0.75 x 10 ⁴³
R2 (9 to 10 km s ⁻¹)	2.8	.10	.28	0.78 x 10 ⁴³
R3 (10 to 12 km s ⁻¹)	4.3	.11	.47	2.03 x 10 ⁴³
R4 (12 to 14 km s ⁻¹)	6.3	.07	.44	2.77 x 10 ⁴³
R5 (14 to 17 km s ⁻¹)	8.8	.06	.53	4.65 x 10 ⁴³
R6 (17 to 23 km s ⁻¹)	13.3	.03	.40	5.31 x 10 ⁴³
Blue Lobe		0.66	3.1	2.0 x 10 ⁴⁴
Red Lobe		0.60	2.5	1.6 x 10 ⁴⁴
Entire Outflow		1.22	5.6	3.6 x 10 ⁴⁴
Optical Depth Corrected ^c		3.5	15.7	1.0 x 10 ⁴⁵
Ambient Molecular Cloud ^d		49		7.3 x 10 ⁴⁴

^aWith respect to ambient cloud velocity of +6.7 km s⁻¹, uncorrected for inclination of outflow out of plane of sky.

^bAssuming T_{ex}=25K, optically thin.

^cCorrected mass assuming $\tau=2.6$.

^dAssuming mass of cloud 49 M_⊙, average turbulence velocity 1.22 km s⁻¹.

velocity to escape from the cloud.

In order to calculate the mechanical luminosity of the outflow, an estimate for the lifetime must be made. A rough dynamical lifetime comes from the extent of the blue lobe of $\sim 19'$ (2.7×10^{18} cm) and the average radial velocity of the outflow of about 5 km s^{-1} , giving a time scale of about 10^5 years. Assuming this value, and that the energy in the outflow is 1.0×10^{45} ergs, the mechanical luminosity of the outflow is roughly 3.2×10^{32} erg s^{-1} or $0.08 L_{\odot}$. Alternatively, if we used the maximum outflow velocity of 15 km s^{-1} , we would have a dynamical timescale of 3×10^4 years and consequently a mechanical luminosity of $0.3 L_{\odot}$. Corrections for the inclination of the outflow, such as were made by Snell and Schloerb (1985) tend to shorten the dynamic timescale and increase the energy, which would further increase the mechanical luminosity. In any case the mechanical luminosity is still one to two orders of magnitude smaller than the infrared luminosity of the outflow, found by Edwards *et al.* (1986), of $7 L_{\odot}$.

If the extended far-infrared emission is the reprocessed shock energy at the wind/molecular outflow interface, then only 1-4% of the wind energy is converted to motion of the molecular shell. Thus the outflow is not in an energy conserving phase, and the vast majority of the wind energy is radiated away. If the outflow is momentum conserving, then roughly a fraction $V_{\text{outflow}}/V_{\text{wind}}$ of the total wind energy would be transmitted to the molecular shell. The wind velocity has been estimated to be 400 km s^{-1} (Stoche *et al.* 1987), which for a molecular outflow velocity of $5\text{-}15 \text{ km s}^{-1}$ would suggest that 2-5% of the wind energy is converted to motion of the molecular shell, a value consistent with the luminosity estimates. The energetics of the outflow are thus consistent with momentum conservation and not energy conservation, as in the interstellar "bubble" models of Castor, McCray and Weaver (1975). This is not surprising since the ambient molecular cloud is relatively dense, and so the cooling time in the shocked molecular gas should be short. In addition, the wind velocities are substantially less than those for

O-stars where the interstellar "bubble" models have been applied, and thus the molecular shell might be expected to remain in a momentum conservation phase.

A question which must still be addressed concerns the origin of the wind. In the models of Uchida and Shibata (1985) and Pudritz and Norman (1983, 1986), the molecular wind is being hydromagnetically launched directly from a rotating, magnetized disk surrounding IRS-5. Due to the large mass of material in the molecular outflow, the vast bulk of the emission cannot be due to the material which has been launched from the disk, but it is possible that it is this hydromagnetically launched wind which has swept out the cavity. On the other hand, in a review of energetic winds and circumstellar disks associated with young stellar objects, Strom *et al.* (1987) discuss the possibility that in L1551/IRS-5, the outflow is driven by a wind generated by accretion from a dense, viscous circumstellar disk onto the surface of the young stellar object. Torbett (1984) has modeled a situation where bipolar flows can be generated by accretion from a disk onto a young stellar object, and finds that only moderate accretion rates are necessary to create bipolar winds with sufficient momentum to drive a molecular outflow. It is interesting to note that, if the far infrared luminosity of the outflow of $7 L_{\odot}$ (Edwards *et al.* 1986) represents the total wind luminosity and if the luminosity of IRS-5 of $38 L_{\odot}$ (Emerson *et al.* 1984) is due to accretion, then the wind luminosity is 18% that of accretion. This is not unreasonable, according to Shu, Lizano and Najita (1987) who propose that a significant fraction of material accreted from a disk onto a rapidly rotating, magnetized protostar must be ejected as a high velocity, bipolar wind. The mass flux from such a wind which would be needed to drive the molecular outflow can be estimated from its momentum and by assuming a dynamical lifetime of 3×10^4 years to give a momentum flux of $5 \times 10^{-4} M_{\odot} \text{ km s}^{-1} \text{ yr}^{-1}$. Using the jet velocity of 400 km s^{-1} (Stocke *et al.* 1987) then means that a mass flux of about $10^{-6} M_{\odot} \text{ yr}^{-1}$ is necessary to drive the outflow, a value similar to that seen for other young stellar objects (Strom, Strom and Edwards 1987).

V. Structure and Kinematics

As has already been discussed in Chapter 2 and in previous sections of this chapter, the molecular outflow in L1551 can be modeled as a thin, expanding shell. If the emission were optically thin, then the column density contrast due to the shell structure would be even greater than is seen in Figures 4.1 and 4.3. Other arguments presented in Chapter 2, such as the coincidence of the low velocity ridge along the limb of the outflow with the bright optical reflection nebula, H-H 102, also support the shell hypothesis. In §IV it was also shown that, at least in the inner part of the outflow, the ratio of the thickness of the blue lobe shell to the radius of the lobe is at most 0.2.

The column density profile of the L1551 molecular cloud as traced by ^{13}CO in Figure 4.4, shows signs of the interaction of the outflow with the cloud. The highest column density in the cloud is not found coincident with IRS-5, but is located within a ridge of high column density which is nearly coincident with the north-west limb of the blue lobe of the outflow, and with a ridge of high density molecular gas as traced by CS emission (see Figure 3.1, and Moriarty-Schieven *et al.* 1987a). This column density ridge extends through IRS-5 and follows the south-west limb of the blue lobe. The region bounded by this ridge, coincident with the interior of the outflow, shows a significant column density minimum. A less distinct column density maximum is found along the south-east limb of the red lobe. This behavior is supportive of the hypothesis that molecular material has been swept out of a cavity, and presently makes up the accelerated molecular shell that surrounds the cavity.

This shell structure extends to the ends of the outflow. This can be seen in Figure 4.1, where in both the red and blue lobes, low velocity emission is found mostly along the limbs of the outflow until the outflow comes to an abrupt stop, where the low velocity emission is located across the entire end of the outflow. In the cavity wall which forms the end of the outflow, the velocity of the molecular gas would be nearly perpendicular to the

line of sight, and so the radial velocity of the emission would be very small along the entire end wall, as is seen in Figure 4.1. The spatial-velocity maps in Figure 4.5 also show the abrupt ends of the outflow. The red-shifted emission at all Y offsets shows an apparent acceleration until X offset = 9', where there is an abrupt end to the acceleration and emission at all velocities is seen. Beyond this point no wind emission is seen at any velocity. The same abrupt end to the high velocity emission is also found at the end of the blue lobe for Y offsets -2.4', -1', and 0'. The rapid decrease in velocity as seen in the spatial-velocity maps (Figure 4.5), and the structure of the low velocity emission seen in Figure 4.1, suggest that the shell of molecular wind has terminated within the molecular cloud. Presumably this low velocity shell is currently being driven into the cloud, extending the molecular outflow. Indeed, at Y offset +1.6', high velocity blue emission continues beyond where the ambient cloud emission begins to disappear, indicating that perhaps here alone, molecular wind has broken out of the cloud and is being accelerated as it meets less and less resistance.

The shape of the red lobe, best traced by the low velocity emission in Figure 4.1, indicates that the shell continues to expand until it reaches the wall forming the end of the outflow. There is no evidence for recollimation of the red lobe, which maintains a relatively constant opening angle of approximately 70° until the end of the outflow. The blue lobe, on the other hand, becomes highly collimated beyond X offset -5'. There is a striking coincidence between velocity changes and structural changes at the point of recollimation. The structural changes at this point (see Figure 4.1) include an abrupt narrowing or "pinch" in the outflow at X offset -4' to -5', and the presence of red-shifted emission in the blue lobe tracing the north-west bend and at offset (-4', -1.8') which is coincident with the edge of the south-west bend. Figure 4.5 shows the velocity changes associated with the point of recollimation. At X offset -4' to -5', the apparent acceleration of the emission ceases followed by a rapid velocity decrease. As the walls of the shell

become collimated and hence parallel, the velocity of the molecular wind in the shell should be parallel, and so the velocity structure should become relatively constant throughout the collimated portion of the lobe, showing only low and medium velocity emission. This would seem to be born out by the spatial-velocity maps in Figure 4.5 (for Y offsets -2.4', -1', and 0') and the maps in Figure 4.1.

Recollimation of the blue lobe, as pointed out by Snell *et al.* (1985), may be due to the ambient pressure of the molecular cloud. After an initial period of collimation (*ie.* the optical/radio continuum jet of Mundt and Fried (1983) and Bieging, Cohen and Schwartz (1984)), the wind from IRS-5 expands freely into the molecular cloud. When the expanding wind achieves pressure equilibrium with the ambient cloud, the outflow will become recollimated. Since the ambient cloud is dominated by turbulent rather than thermal motions and the thermal motion component within the outflow is also probably minor, perhaps a better estimate for the collimating effect of the ambient cloud is a comparison of the momenta in the wind and the cloud. When the instantaneous momentum of the high velocity wind from IRS-5 is approximately the same as the ambient gas momentum, then the wind can no longer expand freely into the cloud and will be deflected. The ambient cloud density needed for equilibrium can then be expressed as:

$$n_{cl} = n_w \frac{V_w}{V_{cl}} = \frac{\dot{M}}{\pi m_H d_w^2 V_w} \frac{V_w}{V_{cl}}, \quad (2)$$

$$n_{cl} = 4.7 \times 10^3 \left(\frac{\dot{M}}{10^{-6} M_\odot \text{ yr}^{-1}} \right) \left(\frac{d_w}{\text{arcmin}} \right)^{-2} \left(\frac{V_{cl}}{1.22 \text{ km s}^{-1}} \right)^{-1} \text{ cm}^{-3}, \quad (3)$$

$$(4.4)$$

where n_w , V_w , and d_w are the outflowing wind's density, velocity and diameter, V_{cl} is the

turbulence velocity of the ambient cloud, m_{H} is the mass of hydrogen, and \dot{M} is the mass loss rate from IRS-5. For a mass loss rate of $10^{-6} M_{\odot} \text{ yr}^{-1}$ (Snell *et al.* 1985) and a turbulence velocity within the cloud (from ^{13}CO observations) of 1.22 km s^{-1} , when the outflow reaches a diameter of $5'$, ambient densities $>200 \text{ cm}^{-3}$ are sufficient to deflect the wind. The density of the cloud as a function of radius established by Snell (1981) shows that the ambient density within the cloud is sufficient to collimate the outflow.

Alternatively, if the hydromagnetic wind models are correct, the recollimation of the molecular outflow may be due to the toroidal magnetic field generated which increases away from IRS-5 (Pudritz and Norman 1986).

A curious feature of the outflow is the presence of red-shifted emission in the blue lobe and blue-shifted emission in the red lobe (see R1 and B1 in Figure 4.1). This emission has been explained by Uchida *et al.* (1987) as evidence for the rotation of the outflow. It should be noted, however, that in addition to tracing the north-west limb of the blue lobe, red-shifted emission is also seen to trace the south-west limb of the blue lobe. This behavior is inconsistent with rotation of the outflow. What then is the origin of this emission? This emission may be better identified with the low velocity shell structure. For instance, the diffuse red emission in the blue lobe and blue emission in the red lobe trace the limbs of the outflow, and in addition, red-shifted emission peaks are found wherever the blue limb is brightest (*eg.* the red emission peak at X and Y offset $(-4', +2')$ is coincident with the B1 peak at the narrowing of the shell, the red "ridge" around offset $(-4', -1')$ traces the north-west "pinch" of the blue lobe and its associated emission peaks), and similarly with blue-shifted emission peaks (*eg.* the peak at offset $(+2', +1')$ is coincident with the R1 emission peak). Furthermore, the north-west limb of the blue lobe and the south-east limb of the red lobe are known to be peculiar. Here the column density of the cloud is highest (see Figure 4.4), the spatial density as traced by CS emission of the cloud is also very high (Chapter 3 and Moriarty-Schieven *et al.* 1987a), and it is in these

two regions where the density of the low velocity molecular wind is high enough ($n > 10^5 \text{ cm}^{-3}$) to excite CS emission. Unfortunately, material at velocities between +5 and +8 km s^{-1} is hidden by the ambient cloud emission, and so the precise coupling between the low velocity blue and red emission is unknown. However, this emission may indicate a region of unusually large velocity dispersion where the molecular shell has met with the most resistance in being driven into the cloud and is streaming around this impediment. Alternatively, it may be caused by the direct interaction of a nearly 400 km s^{-1} wind with the ambient molecular material at $\sim 7 \text{ km s}^{-1}$. In either case, if there is some dispersion in the velocity of the molecular material, the lowest velocity emission may have a component which manifests itself as red emission in the blue lobe and vice versa. There is some blue-shifted emission in the north-east limb of the red lobe, but this may only be due to contamination by HL Tau, or may reflect the fact that the velocity intervals chosen are not precisely symmetrical about the line center, and that 4-5 km s^{-1} (B1) is further from line center (6.7 km s^{-1}) than 8-9 km s^{-1} .

One of the most important features of the hydromagnetic models of Pudritz and Norman (1983, 1986) and Uchida and Shibata (1985) is the acceleration of the molecular wind after being launched from the disk as it moves away from IRS-5. As stated earlier, however, the vast bulk of the emission cannot be coming from the hydromagnetically launched wind itself, due to the large mass of outflowing material. Most of the emission must be coming from molecular material which has been swept out of a cavity; any signature of the hydromagnetic model, such as rotation and acceleration of the launched gas, will probably be obscured. Nevertheless, the molecular outflow shows a definite signature of acceleration (Chapter 2).

The apparent acceleration need not, however, be explained by molecular material actually being accelerated as it moves away from IRS-5, but may instead be a geometrical effect. We propose a simple model in which a high velocity, neutral wind emanating from

IRS-5 or its vicinity is blowing the molecular gas from the cloud into walls surrounding a cavity. Furthermore, the velocity or momentum of this wind is greatest along the axis of the outflow, and decreases with angle away from the axis. The several hundred km s^{-1} jet located near IRS-5 (Beiging, Cohen and Schwartz, 1984; Mundt and Fried, 1983) and the large proper motion of the Herbig-Haro objects H-H 28 and H-H 29 attest to the existence of such a high velocity wind. Such a latitude dependent wind has been suggested for R Mon by Herbig (1968), and in a study of the forbidden line emission from a number of T Tauri stars by Edwards *et al.* (1987), many were best modelled assuming a latitudinally dependent stellar outflow.

Figure 4.8 shows one such model of this geometry. For simplicity, the molecular wind is assumed to lie in a shell whose polar coordinates are $z = r^3$ and whose axis is inclined out of the plane of the sky by 25° (which is larger than the 15° estimated by Snell and Schloerb (1985), but which is not outside of the errors of the estimate), the direction of the molecular wind is radially away from the apex of the shell, and the velocity is greatest along the axis of the outflow, decreasing with $(\cos\theta)^2$ dependence away from the axis. Figure 4.8 shows the iso-velocity contours that would be seen from such an outflow. The solid contours represent the front face of the outflow and the dotted contours represent the back face.

The first feature of note is the nesting of successively higher velocity emission within the next lower velocity, and the separation of higher velocities from the origin of the outflow, which can also be seen in Figure 4.1, and which mimics the effects of acceleration of the outflow. The highest velocity emission appears only in a small region, while lower velocity emission extends much further along the outflow. On the back face, velocities away from the line of sight achieve only small values and then disappear further down the outflow, where low velocity blue-shifted emission appears nearly throughout the lobe. Thus it appears possible that the apparent acceleration of the outflowing molecular wind

may not be a true acceleration, but instead a projection effect of a latitudinally dependent wind. It should be mentioned, however, that the model of Pudritz and Norman (1986) provides an outflow which, if not precisely latitude dependent, may have a similar effect. The velocity of the outflowing wind decreases with distance from the axis of the outflow near IRS-5, and as the outflow expands into the cloud, this may translate into a pseudo-latitude dependence.

As briefly mentioned earlier, at one position at the end of the blue lobe, the high velocity molecular wind appears to have broken out of the cloud. This can best be seen in Figure 4.4, where a small extension at the end of the blue lobe extends beyond the edge of the molecular cloud as traced by ^{13}CO emission. The lower-right spatial-velocity diagram in Figure 4.5 for Y offset +1.6' shows that the high velocity emission, rather than coming to an abrupt stop as in the other three Y offsets, continues beyond where the ambient cloud emission becomes very weak, and indeed appears to be accelerating beyond around X offset -12'. This appears to be direct evidence that a high velocity wind is accelerating the now unimpeded molecular gas which has broken out of the cloud. Ultimately this breakout and disruption will happen to both lobes. We may indeed be witnessing the beginning of the disruption of the L1551 molecular cloud by an outflow which is far more energetic than the entire cloud.

VI. Summary

The molecular wind in the L1551 bipolar outflow is found in a thin, expanding shell which resulted from molecular gas being swept out of a cavity into the shell. This shell completely encloses the cavity, and forms a barrier at the ends of the outflow, which is presumably progressing into the cloud, extending the outflow. The blue lobe of the outflow appears to be just starting to break out of the molecular cloud. A small amount of molecular wind has broken out of the cloud and is being accelerated as it moves away from the cloud. This is direct evidence for a high velocity wind which is sweeping up molecular

material and accelerating the now unimpeded molecular wind. Breakout of the lobes from the cloud would seem to be the next stage in the disruption of the molecular cloud by the outflow.

Optical depth measurements have shown that low velocity emission is more optically thick than high velocity emission, and that the column density of high velocity molecular gas is much larger at the limbs of the outflow than at the center of the outflow along the axis. We have estimated the thickness of the shell at 1.8' south-west of IRS-5 to be about 0.2 that of the radius at that point (~ 0.03 pc). The large optical depths, especially at the limb of the outflow, indicate that the total mass of molecular material in the outflow has been underestimated by a factor of three to ten in the past. Assuming an average optical depth of $\tau=2.6$, we find the total mass to be $3.5 M_{\odot}$, which is about 7% of the molecular cloud mass of $\sim 49 M_{\odot}$, but the fraction could be much higher. The energy within the outflow (which has been uncorrected for the inclination of the outflow but which has been corrected for an optical depth of $\tau=2.6$) has been calculated to be 1×10^{44} ergs, which is greater than the total turbulence energy within the molecular cloud, calculated to be 7.4×10^{44} ergs. The mechanical luminosity of the outflow is much smaller than the extended infrared luminosity, indicating it is still in its momentum conserving phase.

The red lobe of the outflow continues to expand to the end of the outflow and shows no evidence for recollimation. The blue lobe, on the other hand, beyond an initial expansion for a few arcminutes during which there is apparent acceleration of the molecular wind, displays a sharp discontinuity where the outflow abruptly narrows and the velocity structure suddenly changes. Beyond this discontinuity the blue lobe becomes highly collimated. Collimation is likely due to the ambient cloud pressure.

The appearance of red-shifted emission in the blue lobe and blue-shifted emission in the red lobe which has previously been interpreted as rotation of the outflow is more likely to be due to a dispersion in the velocity of the molecular material which has been

accelerated by an ultra-high velocity wind from IRS-5.

Due to the large mass of the outflow, the vast bulk of the emission must be from ambient material which has been swept out of a cavity. The signatures of hydromagnetic models of Pudritz and Norman (1983, 1986) and Uchida and Shibata (1985), such as rotation and acceleration of the launched material, may not be transferred to the largely swept up mass in the molecular outflow. Direct observations of the wind which is launched from the disk may be necessary to confirm these models. The apparent acceleration in the inner region of the red and blue lobes need not be explained as a true acceleration of the molecular material as it moves away from IRS-5. Instead the molecular wind could have been swept up by a very high velocity, neutral wind from IRS-5 whose velocity is latitude dependent. The velocity structure of the molecular wind so swept up could mimic the apparent acceleration seen in the L1551 outflow. Our data is most consistent with a model in which molecular material is swept up by an ultra-high velocity wind originating directly from IRS-5, and which could have been generated by accretion from a disk onto the surface of IRS-5, although a hydromagnetically launched wind from a rotating, magnetized disk could also generate such a wind.

Figure 4.1

Shown are halftone/contour maps of the blue- and red-shifted emission of the L1551 molecular outflow at different velocity intervals. The average antenna temperature within each velocity interval was found, and then a maximum entropy reconstruction method was applied to each map to enhance the effective angular resolution to about $20''$ for the stronger features. The velocity intervals are indicated on each map. The contour intervals for the maps are as follows: intervals B1 (4 to 5 km s⁻¹), B2 (3 to 4 km s⁻¹), R1 (8 to 9 km s⁻¹), and R2 (9 to 10 km s⁻¹) have contours at 1, 2, 4, 6, 8, ... K; intervals B3 (1 to 3 km s⁻¹), B4 (-1 to 1 km s⁻¹), R3 (10 to 12 km s⁻¹), and R4 (12 to 14 km s⁻¹) have contours at 1, 2, 3, ... K; intervals B5 (-4 to -1 km s⁻¹) and R5 (14 to 17 km s⁻¹) have contours .3, .6, .9, ... K; and intervals B6 (-9 to -4 km s⁻¹) and R6 (17 to 23 km s⁻¹) have contours .1, .2, .3, ... K. The X axis is oriented along position angle 45° and is approximately parallel to the outflow axis. The offsets are in arcminutes from IRS-5, which is marked by a large cross, at r.a.(1950) 4^h28^m40.1^s and dec.(1950) +8°01'41.2". The filled diamond marks the position of H-H 28, the filled triangle that of H-H 29, and the filled square that of H-H 30. HL and XZ Tau are indicated on the maps by small crosses. The oddly shaped box in the lower panels represents the extent of the mapped region. X and Y offsets can be converted to right ascension and declination offsets in arcminutes from IRS-5 by using the following transformation: $\alpha(\text{offset})=(X\text{offset}+Y\text{offset})\sin(45^\circ)$ and $\delta(\text{offset})=(X\text{offset}-Y\text{offset})\sin(45^\circ)$. Note the shell structure of the emission in the red and blue lobes and the strong limb brightening, especially at low velocities, as well as the apparent acceleration of the higher velocity emission gradually away from IRS-5. At low velocities, the shell structure appears to close in on itself at the ends of the outflow, possibly indicating a wall at the outflow ends. The red lobe does not appear to become recollimated, while the blue lobe becomes highly collimated beyond X offset -4' to -5'. At this location, the blue lobe experiences a sharp narrowing or "pinch".

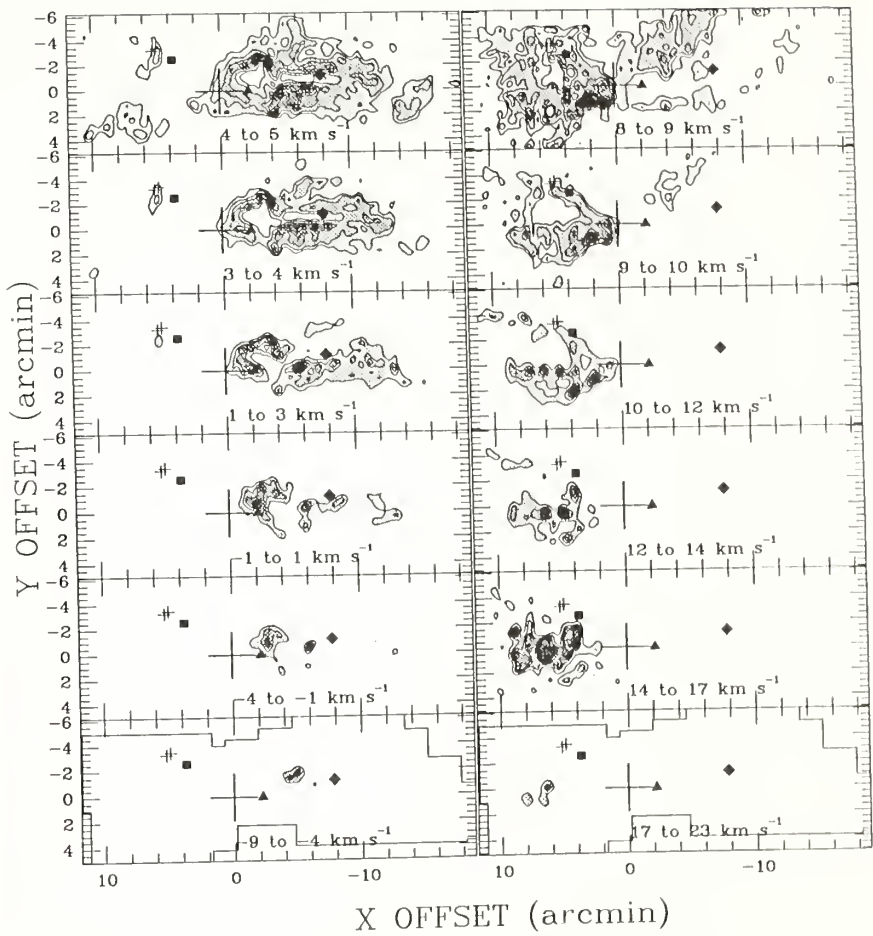


Figure 4.2

The unreconstructed maps of the L1551 outflow are presented here. Offsets, symbols, and contours are the same as in Figure 4.1.

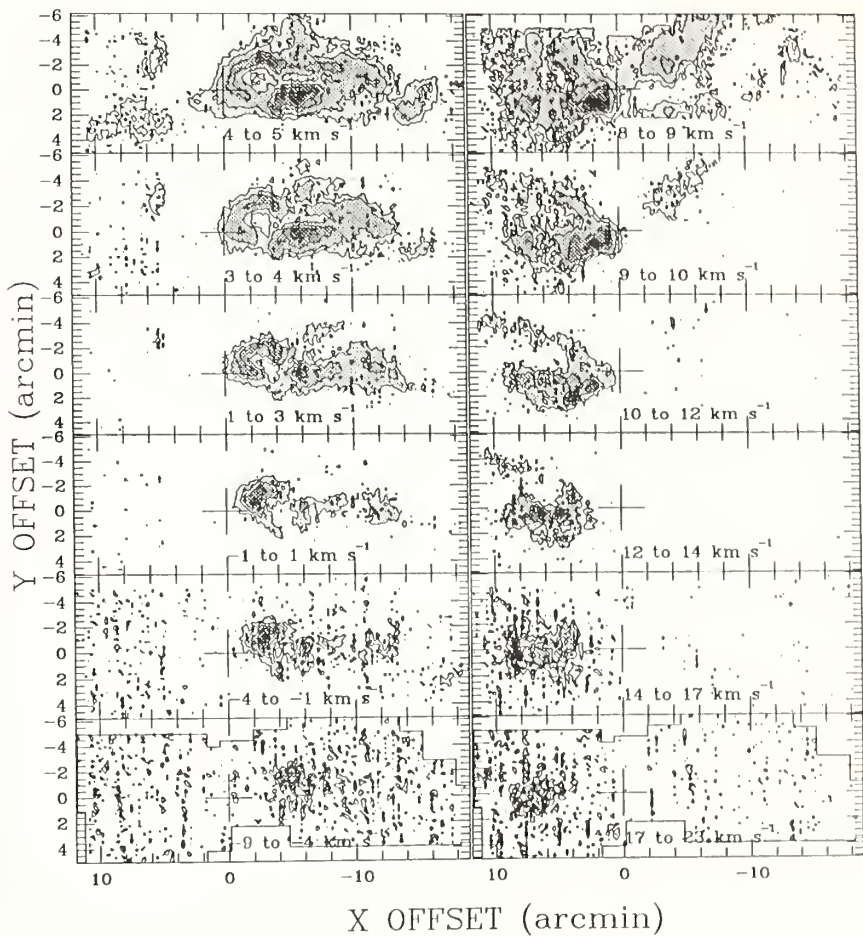


Figure 4.3

The reconstructed integrated antenna temperature (T_R^*) over the entire spectral line wing are displayed here as half-tone/contour maps. The upper panel shows the blue lobe over the velocity interval -9 to 5 km s^{-1} , and the lower panel shows the red lobe over the interval 8 to 23 km s^{-1} . Contours are at $2, 4, 8, 12, \dots \text{ K km s}^{-1}$. The offsets and symbols are the same as in Figure 4.1. The oddly shaped box represents the extent of the mapped region. Limb brightening due to the shell structure is still very evident in the blue lobe, although not as pronounced in the red lobe. Note the weak emission beyond X offset $-13'$, which was not as apparent in Figure 4.1 and which may indicate the blue lobe beginning to break out of the molecular cloud.

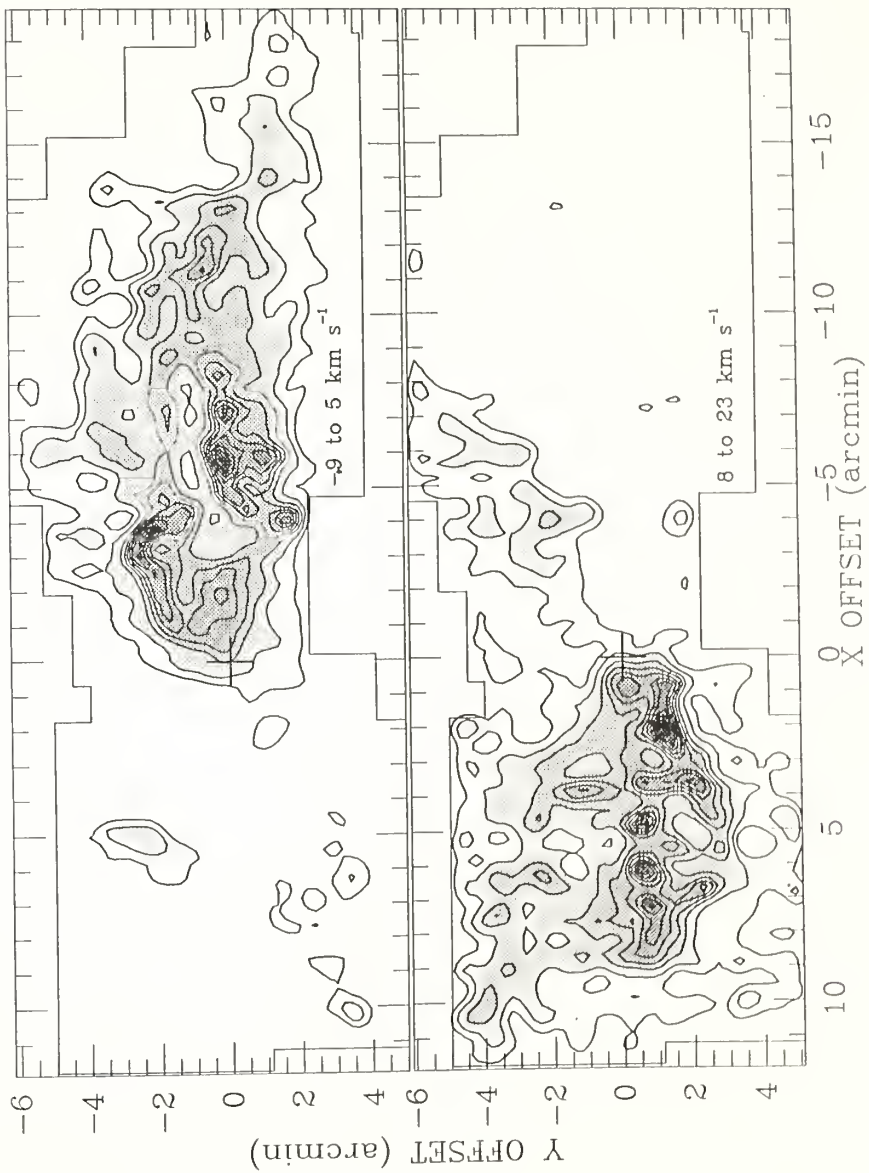


Figure 4.4

The entire L1551 molecular cloud was mapped in ^{13}CO . The ^{13}CO emission is mostly optically thin, so the integrated antenna temperature (T_R^*) over the interval 5 to 8 km s $^{-1}$ as mapped in this figure represents the column density structure of the molecular cloud. Contours are every K km s $^{-1}$. Unlike Figures 4.1 and 4.3, the X axis is parallel to right ascension, *ie.* along position angle 90°. Offsets are in arcminutes from IRS-5, which is indicated on the map by a large cross. The right panel of this figure shows, to the same scale, a few of the contours of the integrated antenna temperature maps of the red and blue lobes of the outflow (from Figure 4.3). Note, in the left panel, the ridge of high column density which is coincident with the limb of the blue lobe of the outflow, and the column density minimum which is surrounded by this ridge. This effect is not as strong in the red lobe. This suggests that cloud material has been swept out of a cavity and has been piled up in a shell. Also note that blue-shifted outflow emission has apparently broken out of the south-west edge of the molecular cloud.

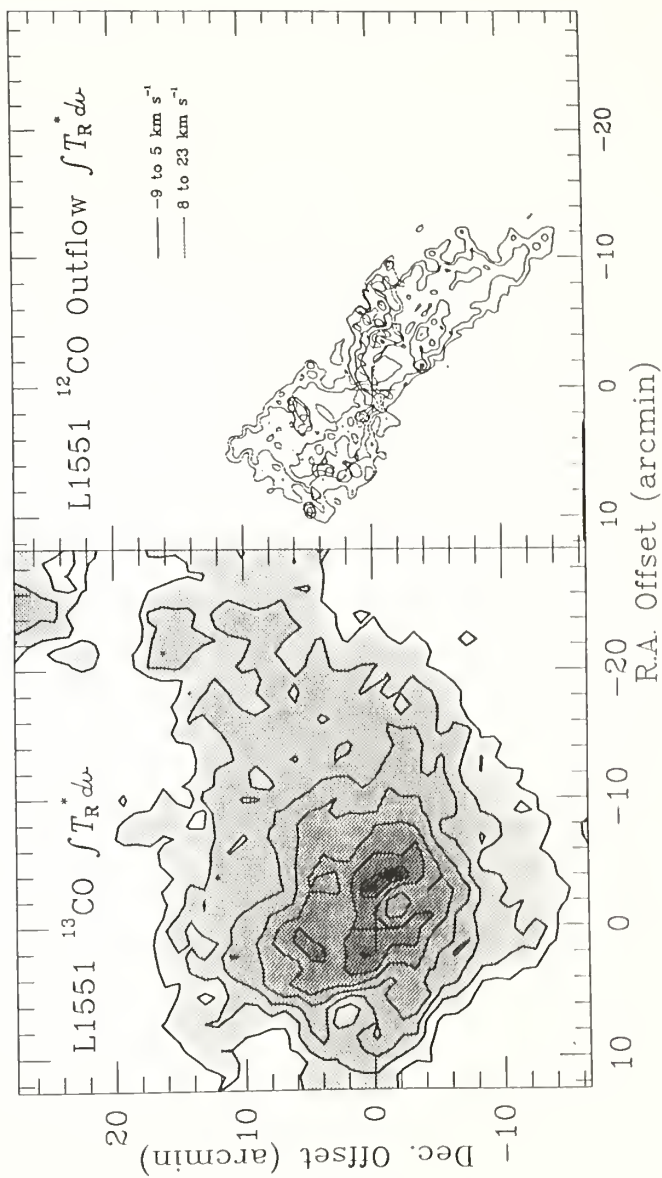


Figure 4.5

Shown here are four spatial-velocity diagrams which have been generated from unreconstructed spectra of the outflow. Each was made along a cut parallel to the outflow (X) axis at Y offsets -2.4', -1', 0', and +1.6'. The contour levels are .5, 1, 2, 3, ... K. The inner few arcminutes of both the red- and blue-shifted line wings both show a similar apparent acceleration. The red lobe ends abruptly at about X offset +9', and no more high velocity emission is seen beyond that point. The blue lobe at Y offsets -2.4' and -1' also end abruptly at X offset -13' to -14', beyond which no high velocity is found. At Y offset +1.6', on the other hand, the emission does not come to an abrupt end, and in fact shows acceleration beyond X offset -9', and the high velocity emission at the end of the outflow is as strong or stronger than the ambient emission. This indicates that the molecular outflow has broken out of the cloud, and that the molecular wind is being accelerated after escaping the confines of the cloud. Also of note is the velocity discontinuity at X offset -4' to -5', visible at all Y offsets, where the outflow becomes recollimated.

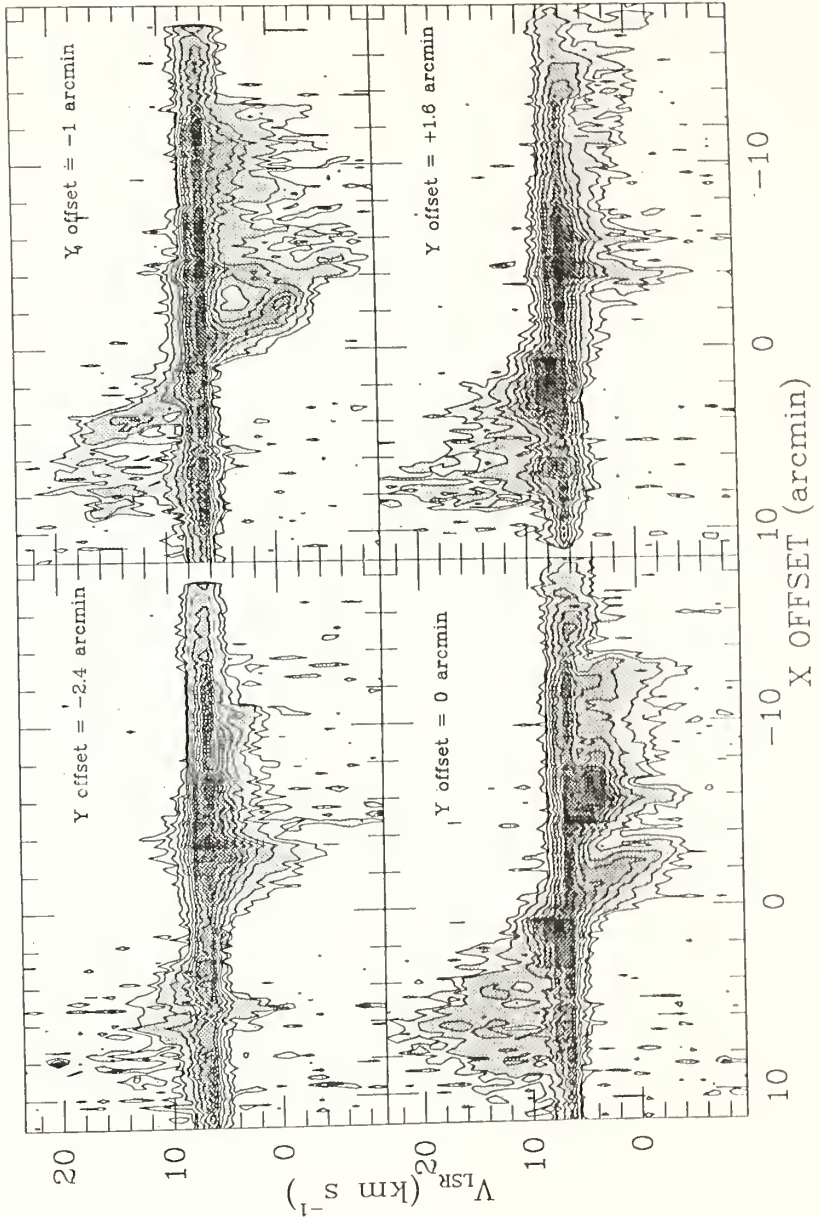


Figure 4.6

This figure presents a comparison of ^{13}CO spectra with ^{12}CO spectra taken at the same position. The ^{13}CO spectra were obtained along a row perpendicular to the outflow axis at X offset $-1.8'$. The Y offset of each spectrum is indicated. The dark, heavy lines represent the ^{12}CO spectra while the thin lines define the ^{13}CO spectra. Antenna temperatures have been scaled to the T_R^* temperature scale.

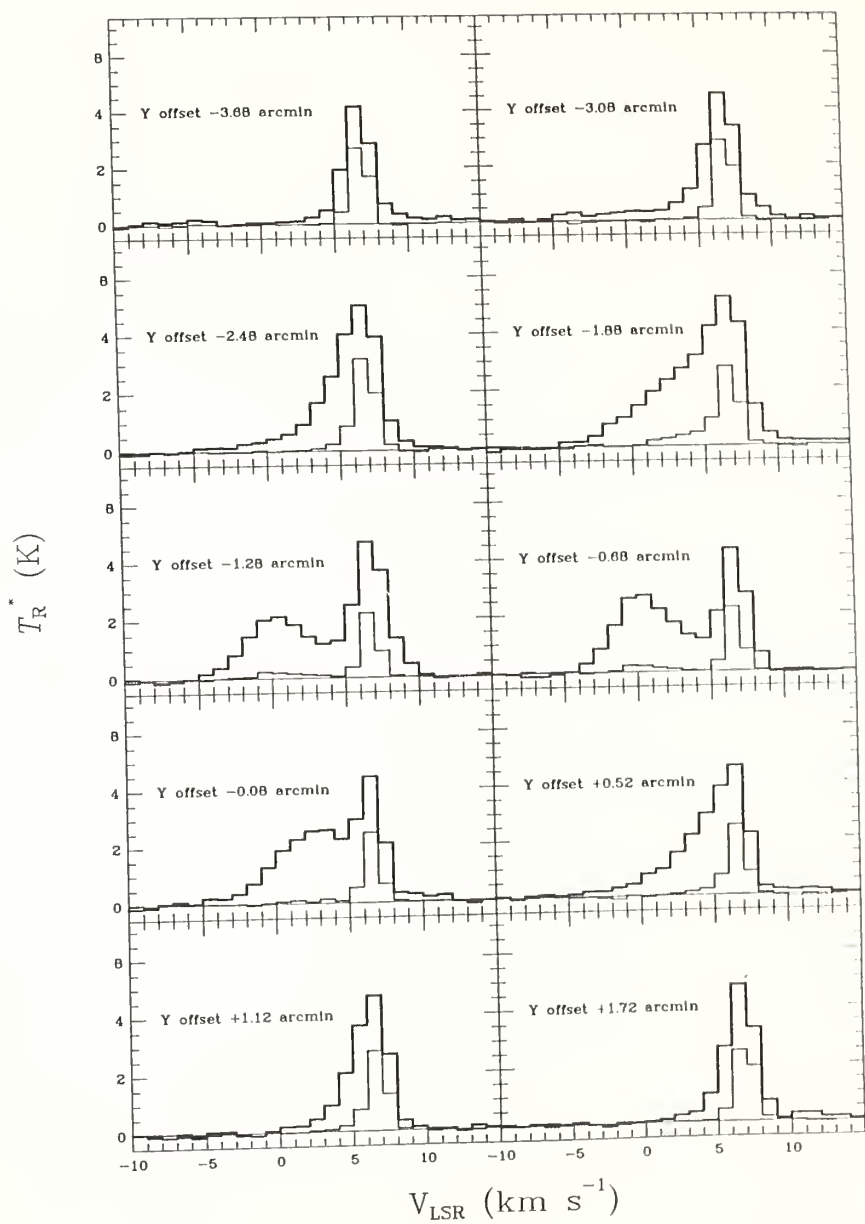


Figure 4.7

The optical depths within the spectral line wings were calculated using the spectra presented in Figure 4.6 and are shown here, along with their standard errors, as a function of velocity interval and Y offset position. The optical depths were calculated under the assumption that the ^{13}CO emission is optically thin and that the ratio of ^{12}CO to ^{13}CO abundance is 60. The spectral line wings, even at high velocities, are much more optically thick than previously suspected. In addition, the optical depths are higher for lowest velocity emission, and greatest along the limb of the outflow, emphasizing the limb brightening.

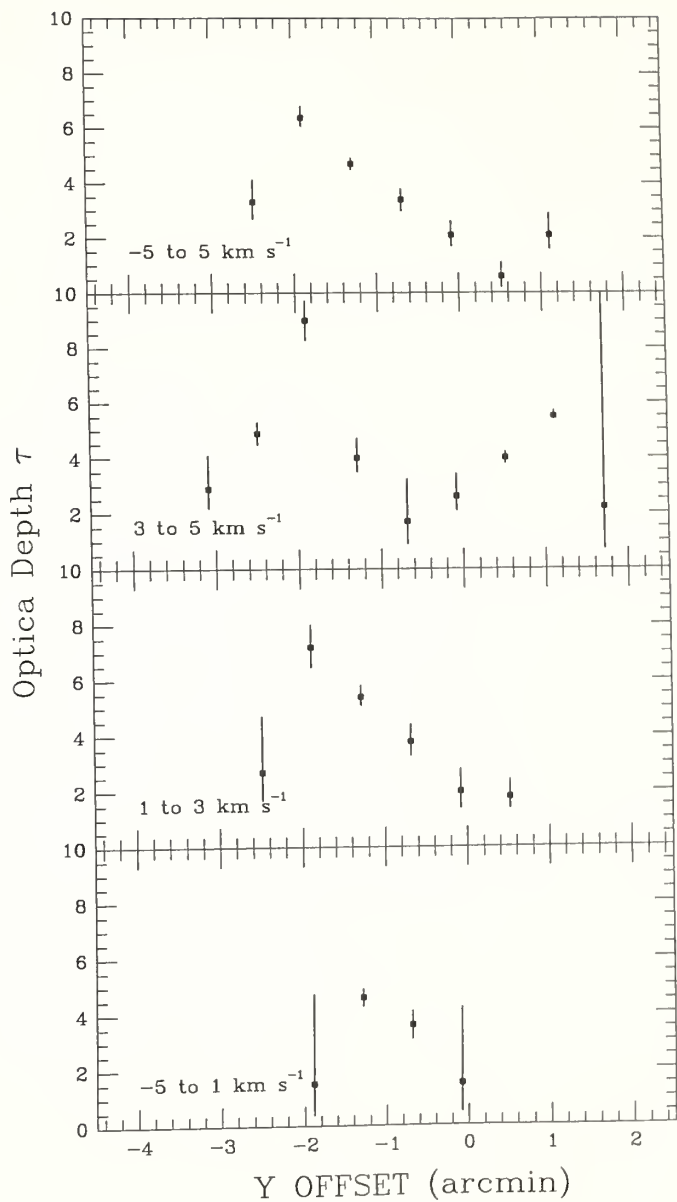
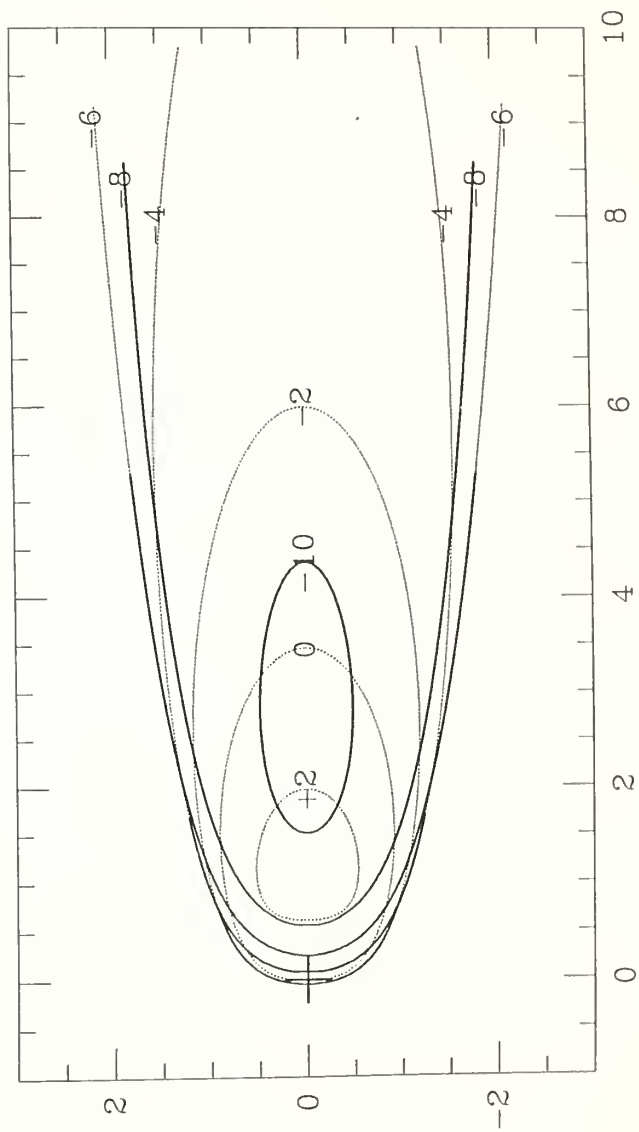


Figure 4.8

A simple kinematic model of the outflow is presented, where the molecular wind is being driven by a high-velocity, latitude dependent neutral wind. It is assumed that the molecular outflow is concentrated in a thin shell, whose shape for convenience is given by $z=r^3$, and that the velocity of the molecular wind is radially away from the $(0,0)$ point. The velocity of the wind is maximum along the axis of the outflow, and decreases with increasing angle away from the axis, *ie.* with a $(\cos\theta)^2$ latitude dependence. The inclination of the outflow axis is 25° out of the plane of the sky. Solid contours refer to the iso-velocity contours for the front side of the outflow, and the dotted contours are the iso-velocity contours for the back side of the outflow. This model duplicates the kinematic structure seen in Figure 4.1 (*ie.* higher velocities found toward the center of the outflow and nested within lower velocity emission, the lack of large positive-velocity emission from the backside of the cloud, and the apparent acceleration of high velocity emission away from IRS-5) without requiring that the molecular wind is actually being accelerated as it moves away from IRS-5.



Chapter 5

The B335 and L723 Bipolar Molecular Outflows

I. Introduction

In Chapters 2 and 4 the structure and kinematics of the L1551 bipolar molecular outflow have been discussed, based on the high resolution maps we obtained. It was suggested that this particular outflow exhibits an expanding shell structure which completely surrounds a cavity in the molecular cloud, which has been swept out by a high velocity, and perhaps latitude dependent, neutral wind from IRS-5. Although the ambient cloud "downwind" of IRS-5 has sufficient pressure to recollimate the blue lobe, the outflow has significantly more energy than the entire cloud and will eventually disrupt a substantial fraction of the molecular cloud, as was also discussed in Chapter 3.

Although we feel that our understanding of the molecular outflow associated with L1551/IRS-5 has improved significantly from this study, it is important to observe additional outflows to see how applicable this model is to other molecular outflows. Two outflows were chosen for this comparison - number 723 in Lynd's catalogue of dark nebulae (L723), and the Bok globule B335 - because of their similarity to L1551. These two outflows have well separated and well collimated lobes so that kinematic and morphological structure should be discernable as in L1551. L723 shows detached spectral line wings (Goldsmith *et al.* 1984) similar to those seen in L1551 (see Figures 2.10 and 4.6). Each possesses a star visible only in the infrared at the geometrical center of the outflow, and is presumably responsible for the outflow. All are of relatively low luminosities; the infrared source in L723 has an infrared luminosity of $6.5 L_{\odot}$ (Vrba *et al.* 1987) and IRS-1 in B335 has an infrared luminosity of $3 L_{\odot} (d/250\text{pc})^2$ (Keene *et al.* 1983), both somewhat less than that of the the infrared luminosity of $39 L_{\odot}$ for IRS-5 in L1551 (Emerson *et al.* 1984). L723 is located at a distance estimated by Goldsmith *et al.* (1984) of 300 pc. From the absence of foreground stars to the cloud core, Bok and

McCarthy (1974) estimated the distance to B335 to be 400 pc. However, using the sudden increase in reddening of background stars compared to foreground stars measured by Tomita *et al.* (1979), and by an apparent association of the B335 cloud with the Lindblad ring (Frerking, Langer and Wilson 1987), its distance is believed to be closer to 250 pc (Frerking, Langer and Wilson 1987), the value adopted in this work.

II. Observations

The data for these observations were obtained at the Five College Radio Astronomy Observatory 14m telescope in 1985 and 1986, using a similar method to that discussed in Chapter 2. Spectra were obtained every 12" along rows oriented north-south (position angle 0°) in the sky. Integration times were typically 40 seconds per point for L723 and 60 seconds per point for B335. The reference position was 150' east of the central position for L723, and for B335 was 30' east of the central position of that map. An area covering approximately 11' x 6.2' of the L723 outflow was mapped with 1588 spectra, while 1312 spectra were obtained of the B335 outflow covering 11.4' x 4.6'. As with the L1551 outflow, the high-velocity spectral line wings were broken up into several velocity intervals in order to examine the velocity structure of the outflows in more detail. Maps of the integrated intensity ($\int_R^* dv$) within each velocity interval were made and each map reconstructed using the maximum entropy algorithm described in Chapter 2. Our reconstructions were progressed to a value of $\lambda=12$, which, from Figure 2.2, yields an effective resolution of about 25" for the stronger features in the maps.

III. Results

a) B335

The red- and blue- shifted high velocity line wings were divided into six velocity intervals. In the blue wing the intervals are 7 to 8 km s⁻¹, 6 to 7 km s⁻¹, and 3 to 6 km s⁻¹, and the red wing intervals are 9 to 10 km s⁻¹, 10 to 11 km s⁻¹, and 11 to 14 km s⁻¹. Maps were made of the integrated intensity ($\int_R^* dv$) in each velocity interval; the maximum

entropy reconstructed maps are shown in Figure 5.1, and the unreconstructed images in Figure 5.2. The cross indicates the position of IRS-1, which is listed in the IRAS point source catalogue as IRAS PSC 19345+0727 at R.A.(1950) = $19^{\text{h}}34^{\text{m}}35.3^{\text{s}}$ and Dec.(1950) = $+7^{\circ}27'24''$. Offsets are in arcminutes from this position. In Figure 5.3, maps of the total integrated (reconstructed) intensity over the red and blue line wings (3 to 7 km s^{-1} and 10 to 14 km s^{-1}) are presented.

The symmetry in the shape of the outflow as seen in Figures 5.1 and 5.3 is very striking. Both lobes of the outflow show a constant and nearly equal opening angle of about 45° . There is no hint of recollimation of either lobe, and both lobes continue to the ends of the outflow with the same opening angle. In the red lobe (9 to 10 km s^{-1} , 10 to 11 km s^{-1} and 11 to 14 km s^{-1}), there is a strong suggestion that the emission is located in three or four clumps preferentially at the edges of the lobe. Such limb brightening would be seen if the molecular outflow is a shell structure, so that the column density of the high velocity molecular gas is greatest at the edges of the outflow lobe and smaller in the interior of the lobe. This is similar to the L1551 outflow, which has emission strongest at the limbs of the outflow (see Figure 2.6, 2.7, 4.1 and 4.2) as well as the largest optical depths along the periphery of the lobes (see Figure 4.6) indicating a shell structure. The limb brightening apparent in the red lobe of B335 indicates that this outflow also exhibits a shell structure. In the blue lobe, this structure is not so evident. Low velocity blue-shifted emission (7 to 8 km s^{-1}) is somewhat contaminated by emission from the ambient molecular cloud (which has a velocity of 8.2 km s^{-1}), and so any limb brightening may be obscured. Emission at 6 to 7 km s^{-1} shows a ridge of column density maximum along the north limb of the blue lobe, but the rest of the emission is somewhat diffuse. The highest velocity blue-shifted emission (3 to 6 km s^{-1}), however, again shows a structure similar to the red lobe, in that the emission is found in clumps located along the periphery of the blue lobe. From the other similarities between the two lobes, the blue lobe would also seem to

exhibit a shell structure.

A striking feature of the B335 outflow is the presence of red-shifted emission in the center of the blue lobe and blue-shifted emission in the center of the red lobe. The lowest velocity (7 to 8 km s⁻¹ and 9 to 10 km s⁻¹) emission shows a distinct, symmetric double lobe structure in both the red and blue lobes. At medium velocities (6 to 7 km s⁻¹ and 10 to 11 km s⁻¹) the red-shifted emission in the blue lobe is weaker than the red-shifted emission in the red lobe (and vice versa), and the highest velocity emission is very weak. The presence of red-shifted emission in the center of the blue lobe and vice versa can be best explained by a similar expanding shell model proposed for the L1551 outflow. The red-shifted emission in the blue lobe is emission from the back side of the shell, and the blue-shifted emission in the center of the red lobe is emission from the front face of the red lobe. Cabrit and Bertout (1986) have modeled the emission seen from such a geometry, and show that if the molecular wind is concentrated in an expanding shell, then at any position in the interior of the lobe one is seeing emission from two locations, from the front and back face of the outflow lobe. Each of these faces, by projection, should be moving at different velocities. For an outflow which is oriented precisely in the plane of the sky, emission from the front face will be blue-shifted while the back face will be red-shifted. If the outflow is oriented very slightly out of the plane of the sky, the lobe which is inclined toward the observer will have a small amount of red-shifted emission located in the center of the lobe, while the other lobe will have a small amount of blue-shifted emission in its center. The structure seen in Figures 5.1 and 5.3 seems to show this behavior quite markedly. In the case of L1551, the outflow would seem to be oriented at a still greater inclination out of the plane of the sky, so that emission from the back side of the blue lobe and front side of the red lobe are hidden by the ambient emission (see Figures 2.12 and 4.8). Particularly intriguing is the 9 to 10 km s⁻¹ interval, where the red (west) lobe shows limb brightening while the blue (east) lobe is most intense in the center of the lobe.

The outflow axis of B335 must be nearly in the plane of the sky for the emission in the two lobes at the lowest velocities to appear so symmetrical. It is possible to make an estimate for the inclination of the outflow out of the plane of the sky using the near symmetry of the red and blue lobes. Assuming that the front and back surfaces of the shell are moving at the same velocity, then the apparent differences in the maximum red-shifted and blue-shifted velocities seen in a shell must be due to the inclination of the outflow lobe. In the red lobe, the maximum red-shifted velocity seen is about 14 km s^{-1} while emission blueward of 6 km s^{-1} becomes very weak. If the velocity of the ambient emission is $+8.6 \text{ km s}^{-1}$, this means that the extremes in relative velocity are $+5.4 \text{ km s}^{-1}$ and -2.6 km s^{-1} , which, assuming an opening angle of 45° , implies an inclination of 9.7° . The blue lobe has extreme velocities of -5.3 km s^{-1} and $+2.9 \text{ km s}^{-1}$, implying an inclination of 8.2° . We adopt an inclination of $i = 9^\circ \pm 1^\circ$. If this value is correct, the maximum velocity of the outflow would be about 11 km s^{-1} .

The L1551 outflow shows a gradual increase in velocity away from IRS-5, which could be due to the acceleration of the molecular wind as it moves away from IRS-5, or perhaps to a geometric effect as discussed in Chapter 4. B335 may also show a velocity increase away from IRS-1, but the effect is much less apparent, if indeed it is present. The medium velocity emission (6 to 7 km s^{-1} , 10 to 11 km s^{-1}) seems to overlap slightly the position of IRS-1, while the high velocity emission (3 to 6 km s^{-1} , 11 to 14 km s^{-1}) is offset slightly by as much as a half arcminute from IRS-1 (which is the effective angular resolution of the reconstructed maps). In addition, the medium velocity red-shifted emission in the blue lobe and the blue-shifted emission in the red lobe are both offset by about an arcminute from the infrared star, implying that it is not until well away from the star that the velocity of the back (or front) face of the outflow becomes large enough to be seen in this velocity interval. Figure 5.4 shows a spatial-velocity map made at different declination offsets. The red-shifted line wing east of r.a. offset $0'$ shows a gradual

increase in the maximum velocity emission as one progresses eastward away from the infrared star, although the blue-shifted line wing to the west of r.a. offset 0' does not show this behavior.

More prominent is the high velocity emission found at the ends of the outflow. Beyond $\pm 4'$, the medium velocity emission becomes very weak and disappears, while the high velocity emission extends at least another arcminute and becomes quite strong. As can be seen from Figure 5.4, the ambient emission beyond $\pm 4'$ is itself becoming very weak so that the high velocity emission has become stronger than the ambient emission. Just as in the L1551 outflow, where at a single location the blue lobe extends beyond the edge of the molecular cloud (see Figure 4.4), the ends of both the red and blue lobes of the B335 outflow may have broken out of the cloud core, and the molecular shell, now unimpeded by the dense ambient molecular gas, is being reaccelerated by a high velocity wind from IRS-1. Frerking, Langer and Wilson (1987) have mapped the ^{13}CO distribution of the B335 molecular cloud and have found that the column density of the cloud peaks at about the position of the infrared star, then traces a ridge which extends north-east and then south-east. Langer, Frerking and Wilson (1986) discovered what they interpreted as another outflow to the east of the outflow mapped in Figure 5.1, and separated from it by a void in the molecular cloud. Cabrit (1987, private communication) has found a bridge of outflowing molecular gas connecting the two outflows, and has postulated that both are part of the same outflow, *ie.* after the wind escapes from the cloud at the east end of the main outflow, it reenters the cloud still further east to create a partly detached continuation of the outflow. This would suggest that all of the high velocity molecular material near B335 is powered by high-velocity winds from IRS-1.

b) L723

The high velocity spectral line wings of the L723 bipolar outflow have been broken up into seven velocity intervals. Over the red lobe: 13 to 14 km s⁻¹, 14 to 16 km s⁻¹, 16 to 18

km s⁻¹, and 18 to 22 km s⁻¹. Over the blue lobe: 4 to 6 km s⁻¹, 2 to 4 km s⁻¹, and -2 to 2 km s⁻¹. Unfortunately, a weak extended feature, possibly a background molecular cloud (Goldsmith *et al.* 1984) contaminates the emission from 6 to 8 km s⁻¹, while the L723 molecular cloud itself has an ambient velocity of ~11 km s⁻¹. Maps of the reconstructed integrated intensity ($\int I_R dv$) within each velocity interval is shown in Figure 5.5, and the raw, unreconstructed images are presented in Figure 5.6. Figure 5.7 displays two maps showing the integrated reconstructed intensity over the entire spectral line wing (13 to 22 km s⁻¹ and -2 to 6 km s⁻¹).

In contrast to the B335 bipolar outflow, the structure of the L723 outflow is quite different from that of L1551. Both the red and blue lobes are very narrow and highly collimated. L723 is very clumpy, but unlike B335 and L1551, signs of limb brightening are conspicuously absent. In the red lobe, the lowest velocity (13 to 14 km s⁻¹ and 14 to 16 km s⁻¹) emission appears to be strongest, not at the periphery of the outflow as would be expected for a shell, but at the center of the lobe. In addition, the brightest clumps in the red lobe show emission at all velocities. At lower velocities in the blue lobe (4 to 6 km s⁻¹) the brightest emission is found along the southern limb, although the rest of the lobe is quite diffuse. Higher velocity emission in the blue lobe (2 to 4 km s⁻¹ and -2 to 2 km s⁻¹), except for the immediate vicinity of the infrared star (indicated by a cross), is found predominantly down the axis of the outflow. A very curious feature of the red lobe which has not previously been noted, but of which indications can be seen in the maps of Hayashi *et al.* (1987), is a long, narrow and sinuous ridge of emission at 13 to 14 km s⁻¹ and 14 to 16 km s⁻¹ which very closely traces the south periphery of the blue lobe out to a distance of 2.5' east of the central star. This feature is reminiscent of structure found in the L1551 outflow and may, as in L1551, indicate a larger than average velocity dispersion at the interface of the molecular outflow with the ambient cloud.

Both the red and blue lobes are very narrow and much more highly collimated than

previously suspected (Goldsmith *et al.* 1984). The average width of the red lobe is about 1.5' (0.13 pc at 300 pc), so if any shell structure is present, it may not be resolvable, even with the $\sim 25''$ reconstructed resolution of our maps. Hayashi *et al.* (1987) observed a much smaller region of the same outflow using a 45m telescope whose angular resolution is about 15'', and was also unable to resolve any of the bright features of the red lobe. The blue lobe is also highly collimated with average width of about 2' (0.17 pc at 300 pc). The dimensions of the blue lobe of the outflow are 6' x 2' and the red lobe 4' x 1.5', a collimation ratio of nearly 3:1.

The L273 outflow shows no systematic shift of higher velocity emission away from the central infrared star. High velocity red and blue emission is found in the immediate vicinity of the infrared star and show no apparent shift with velocity. In addition, high velocity emission extends to the ends of the outflow and stops at the same location as lower velocity emission. In Figure 5.8 are displayed spatial-velocity maps using the unreconstructed spectra made along cuts through the L723 outflow along rows oriented parallel to the east-west axis, at several declination offsets. The spatial-velocity diagram made at declination offset 0' again shows no signs of acceleration of the outflow. High velocity blue-shifted emission begins abruptly at r.a. offset -0.5, and high-velocity red-shifted emission begins equally abruptly at r.a. offset +0.5'. The gradual increase in high-velocity emission seen in the spatial-velocity map at declination offset -1' cannot be interpreted as acceleration since that particular cut misses the high-velocity emission until r.a. offset 2' and is just grazing the edge of the low velocity emission until that point.

The most peculiar feature of the L723 outflow was first noted by Goldsmith *et al.* (1984), and was again commented upon by Hayashi *et al.* (1987). This refers to the twin, nearly perpendicular axes of symmetry of the red and blue lobes through the infrared star; one axis of symmetry runs approximately along position angle 26° (roughly north-south) and joins the two smaller lobes in the immediate vicinity of the IR star, and the other joins

the two larger lobes running roughly east-west (approximately position angle 115°). The p.a. 26° blue "lobe" forms a narrow, unresolved linear feature which overlaps the central star and slightly overlaps the red "lobe". Two suggestions made by Goldsmith *et al.* (1984), is that either there are two separate, superimposed outflows at this location, or else that the outflow axis has precessed between two outflow events. Hayashi (1987, private communication) has mapped the CS J=1–0 structure at the center of the outflow at high angular resolution and has found an elongated, disk-like structure whose long axis is oriented nearly east-west, parallel to the local magnetic field. This suggests that the orientation of the outflow is now north-south, and that perhaps the east-west lobes, which are much larger and hence older, are a past phase of the outflow which has precessed to the current north-south orientation.

IV. Mass and Energetics

The mass of molecular gas within the B335 outflow was calculated in the manner described in Snell *et al.* (1984), assuming that the high velocity emission is optically thin and in LTE, and assuming an excitation temperature $T_{\text{ex}} = 10\text{K}$. These values are presented in Table 5.1. As noted in Chapter 4, if T_{ex} is as large as 35K, then the mass may be greater by a factor of three. In addition, if the emission is not optically thin, as was found by Goldsmith *et al.* (1984), then the mass may be again underestimated. Goldsmith *et al.* (1984) found the average optical depth in the line wings at a few locations to be 2.7 and 5.2 for the blue-shifted and red-shifted line wings respectively. The momentum and energy of the outflow within each velocity interval, assuming a distance of 250 pc, are also presented in Table 5.1. A correction for the projection of the velocity of the outflow out of the plane of the sky has also been applied, by assuming that the outflow has an opening angle of 45° and is inclined $i = 9^\circ$ out of the plane of the sky. If all of the molecular emission is moving at the same velocity, then the molecular outflow is moving at a velocity of 11 km s^{-1} . The total mass of outflowing molecular material is found to be $0.13 M_\odot$.

Table 5.1
Mass, Energy and Momentum of B335 Outflow

<u>Velocity Interval</u>	<u>Mass</u> (M_{\odot})	<u>Momentum</u>		<u>Energy</u>	
		(uncorr.) ^a (M_{\odot} km s ⁻¹)	(corr.) ^a	(uncorr.) ^a	(corr.) ^a (ergs)
7 to 8 km s ⁻¹	0.056	0.039	0.62	2.8×10^{41}	6.8×10^{43}
6 to 7 km s ⁻¹	0.012	0.020	0.13	3.5×10^{41}	1.5×10^{43}
3 to 6 km s ⁻¹	0.011	0.041	0.12	1.5×10^{42}	1.3×10^{43}
9 to 10 km s ⁻¹	0.030	0.039	0.33	5.1×10^{41}	3.6×10^{43}
10 to 11 km s ⁻¹	0.009	0.021	0.10	4.8×10^{41}	1.1×10^{43}
11 to 14 km s ⁻¹	0.010	0.043	0.11	1.8×10^{42}	1.2×10^{43}
Total Blue Lobe	0.079	0.10	0.87	2.1×10^{42}	9.6×10^{43}
Total Red Lobe	0.049	0.10	0.54	2.8×10^{42}	5.9×10^{43}
Total Outflow	0.13	0.20	1.4	4.9×10^{42}	1.6×10^{44}
B335 Cloud Core ^b	11 - 14				2×10^{44}

^aCorrected or uncorrected for inclination of outflow axis out of plane of the sky ($i = 8^{\circ}$).

^bFrom Frerking, Langer and Wilson (1987)

This value is consistent with the mass found by Goldsmith *et al.* (1984) after correcting for the different cloud distance assumed. The total mass of the B335 cloud core was estimated by Frerking, Langer and Wilson (1987) to be 11 to 14 M_{\odot} , and thus the mass of outflowing molecular material is about 1% that of the cloud core. If the turbulence velocity of the cloud core is $\sim 1.4 \text{ km s}^{-1}$ (from ^{13}CO line parameters in the cloud core taken by Frerking, Langer and Wilson), then the total energy of the cloud core is about 2×10^{44} ergs. The energy within the outflow, corrected for inclination, is about 1.6×10^{44} ergs, approximately the same as that of the molecular cloud core. The total corrected momentum of the outflow is $1.4 M_{\odot} \text{ km s}^{-1}$. If the total momentum of the outflow were conserved and shared by all of the mass of the cloud, the entire cloud would be accelerated to a velocity of about 0.1 km s^{-1} , which is insufficient to disperse the cloud (since it has an escape velocity of 0.5 km s^{-1}). Since the outflow is highly directed, it may, however, have a significant disruptive effect on the core and along the path of the outflow and may be responsible for the void in the molecular cloud found by Frerking, Langer and Wilson (1987) beginning about 5' west of IRS-1 and continuing to about 10' west, and beyond which the blue lobe of the outflow appears to resume (Cabrit 1987, private communication). If the maximum velocity of molecular emission is $\sim 6 \text{ km s}^{-1}$ (uncorrected) or 11 km s^{-1} (corrected for inclination), then the dynamical lifetime of the outflow can be estimated at 6×10^4 years (uncorrected) or 4×10^4 years (corrected). If the continuation of the blue lobe beyond the void which was found by Cabrit (1987) and Langer, Frerking and Wilson (1986) is part of the same outflow, then the lifetime is more likely 1.4×10^5 years or 9.4×10^4 years at 250 pc. From these values, the (corrected) mechanical luminosity can be estimated to be $0.013 L_{\odot}$. This value is about 0.4% the infrared luminosity of the central infrared star. Jarrett and Edwards (1988) have found an envelope of far infrared emission similar to that associated with the L1551 outflow and which may be associated with the B335 outflow. This extended emission has a total

luminosity of about $1.1 L_{\odot}$, or 37% of the luminosity of IRS-1. If it is indeed associated with the outflow, then $\sim 1\%$ of the wind energy is being converted to motion of the molecular shell, similar to the 1-4% seen for L1551.

It is interesting to compare the mass and energy of the B335 outflow with that of L1551, under the same assumptions of optically thin emission at $T_{\text{ex}} = 10\text{K}$. B335's outflow mass is about 19% that of L1551, its corrected momentum is 45% the (uncorrected for inclination) momentum of L1551, and the energy of the B335 outflow (corrected for inclination) is about 80% that for the L1551 outflow. Considering that the B335 outflow is oriented nearly in the plane of the sky and thus much of the mass of the outflow is hidden by ambient emission, the two outflows are not dissimilar. Indeed, both outflows have approximately the same length of 1.2 pc.

The mass of molecular gas within the L723 outflow was calculated, as in the case of B335, assuming $T_{\text{ex}} = 10\text{K}$ and that the outflow is in LTE and optically thin. The total mass within each velocity interval, as well as the momentum and energy of the outflow (uncorrected for optical depth and projection effects) are presented in Table 5.2. The total mass of the outflow of about $0.18 M_{\odot}$ is underestimated by perhaps 20% because of the contaminating emission at 6 to 9 km s^{-1} which hides the low velocity blue-shifted emission.

V. Summary

The B335 bipolar molecular outflow is a good candidate for possessing a similar expanding shell structure to that seen in the L1551 outflow. It exhibits significant limb brightening, which is indicative of a shell, and in addition, the backside of the blue lobe and front side of the red lobe are clearly visible. This latter indicates that the outflow axis is nearly perpendicular to the line of sight, and differences in the highest velocities seen in each lobe lead to an estimate that the outflow is inclined about 9° out of the plane of the sky. The slight shift of higher velocity emission away from IRS-1 and the larger separation of the red-shifted emission in the blue lobe (and vice versa) from IRS-1 suggest a possible

Table 5.2**Mass, Energy and Momentum within the L723 Outflow**

<u>Velocity Interval</u>	<u>Mass</u> <u>(M_{\odot})</u>	<u>Momentum</u> <u>($M_{\odot} \text{ km s}^{-1}$)</u>	<u>Energy</u> <u>(ergs)</u>
13 to 14 km s ⁻¹	0.035	0.09	2.2×10^{42}
14 to 16 km s ⁻¹	0.035	0.14	5.6×10^{42}
16 to 18 km s ⁻¹	0.015	0.09	5.4×10^{42}
18 to 22 km s ⁻¹	0.010	0.09	8.1×10^{42}
4 to 6 km s ⁻¹	0.042	0.25	1.5×10^{43}
2 to 4 km s ⁻¹	0.019	0.15	1.2×10^{43}
-2 to 2 km s ⁻¹	0.021	0.23	2.5×10^{43}
Total Red Lobe	0.10	0.41	2.1×10^{43}
Total Blue Lobe	0.08	0.63	5.2×10^{43}
Total Outflow	0.18	1.04	7.3×10^{43}

apparent acceleration, such as that seen in L1551, but this effect is slight, if present. The outflow does not become recollimated and appears to have broken out both ends of the cloud, and the emission at the very ends of the outflow show some signs of being reaccelerated, possibly by high velocity wind from IRS-1 driving the now unimpeded molecular wind. To the east of the outflow, this high velocity wind is apparently travelling through a void in the molecular cloud and then pushing into another part of the same cloud, creating an extension of the blue lobe. About 1% of the mass of the molecular cloud is involved in the outflow, which contains as much energy as the entire cloud and which may have sufficient momentum to disrupt the cloud core.

The L723 bipolar outflow, on the other hand, shows very little evidence for a shell structure. The red and blue lobes are narrow and highly collimated, and we may have insufficient angular resolution, even using the maximum entropy technique, to resolve the structure. Another peculiarity in the structure of L723 lies in the twin axes of symmetry of the outflow, with a small, very narrow, red and blue lobe aligned along position angle $\sim 26^\circ$ and another larger, highly collimated red and blue lobe aligned along position angle $\sim 105^\circ$. These two axes of symmetry may indicate two separate outflows with the same origin or perhaps that the outflow axis has precessed by about 90° .

Figure 5.1

Displayed here are maps of the B335 bipolar outflow which were made by finding the integrated intensity ($\int I_p^* dv$) over the velocity interval indicated and were then reconstructed using maximum entropy. The contour intervals are .25, .5, 1, 1.5, 2, 2.5... K km s⁻¹, except for the 7 to 8 km s⁻¹ interval which has contours 1, 1.5, 2, 2.5,.... K km s⁻¹. The cross marks the position of IRS-1 which is listed in the IRAS point source catalogue as IRAS PSC 19345+0727 with coordinates R.A.(1950) = 19h34m35.3s and Dec.(1950) = +7°27'24". Offsets are in arcminutes from this position. The maps were fully sampled within the area bordered by the dotted line shown in the maps of the 3 to 6 km s⁻¹ and 11 to 14 km s⁻¹ velocity intervals. Note the symmetry of the two lobes at the lowest velocities (7 to 8 km s⁻¹ and 9 to 10 km s⁻¹), the presence of red-shifted emission in the center of the blue lobe and blue-shifted emission in the center of the red lobe at the two middle velocities (6 to 7 km s⁻¹ and 10 to 11 km s⁻¹), and the apparent limb brightening of the emission at most velocities, indicating a shell structure for the molecular outflow.

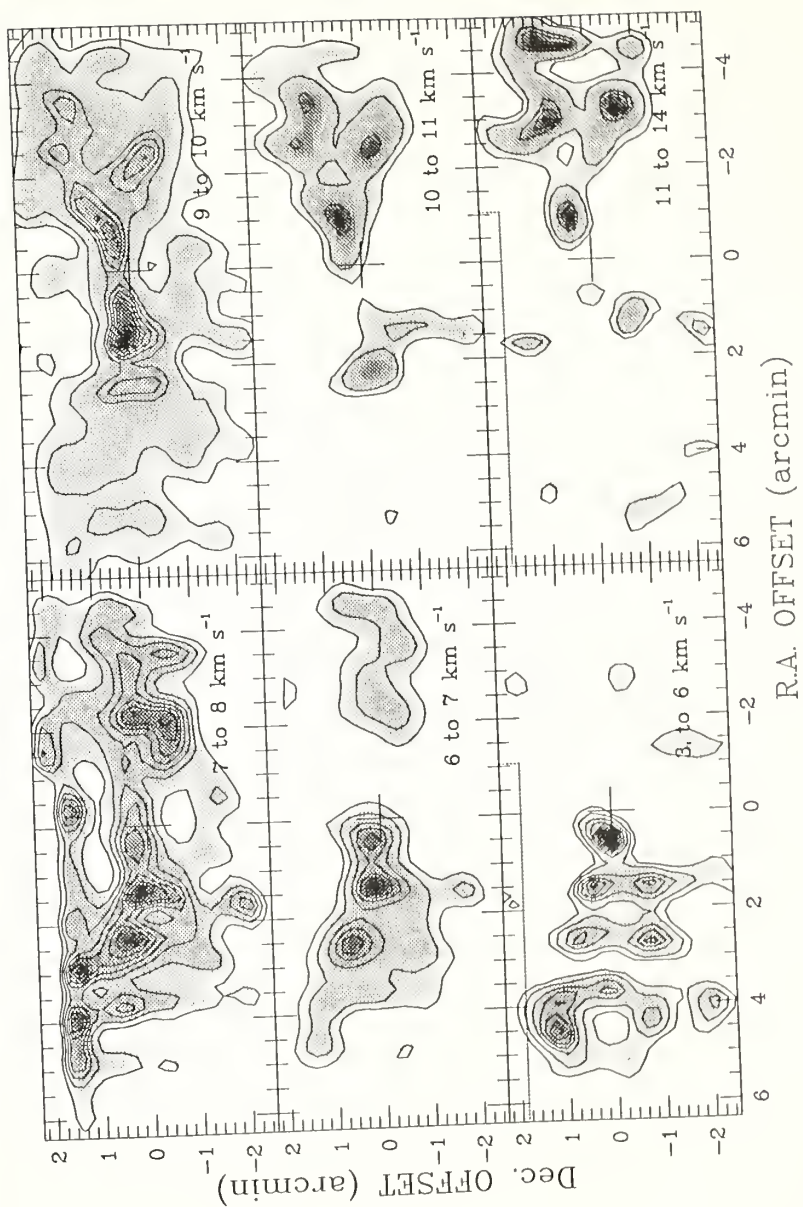


Figure 5.2

The raw, unreconstructed maps of the B335 outflow are shown in this figure. Offsets, symbols, and contours are the same as in Figure 5.1.

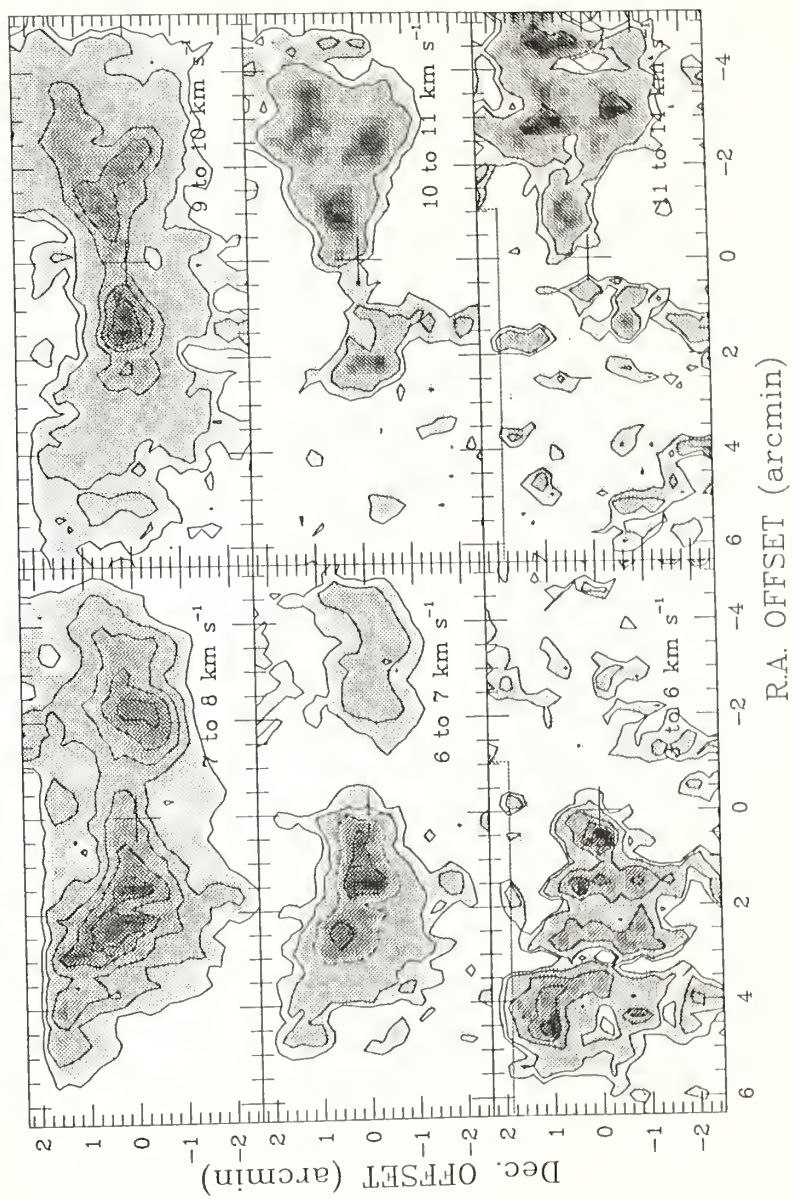


Figure 5.3

The integrated reconstructed intensity over the line wings from 3 to 7 km s⁻¹ and from 10 to 14 km s⁻¹ are presented. Offsets and symbols are the same as in Figure 5.1. The contours are at every 0.5 K km s⁻¹.

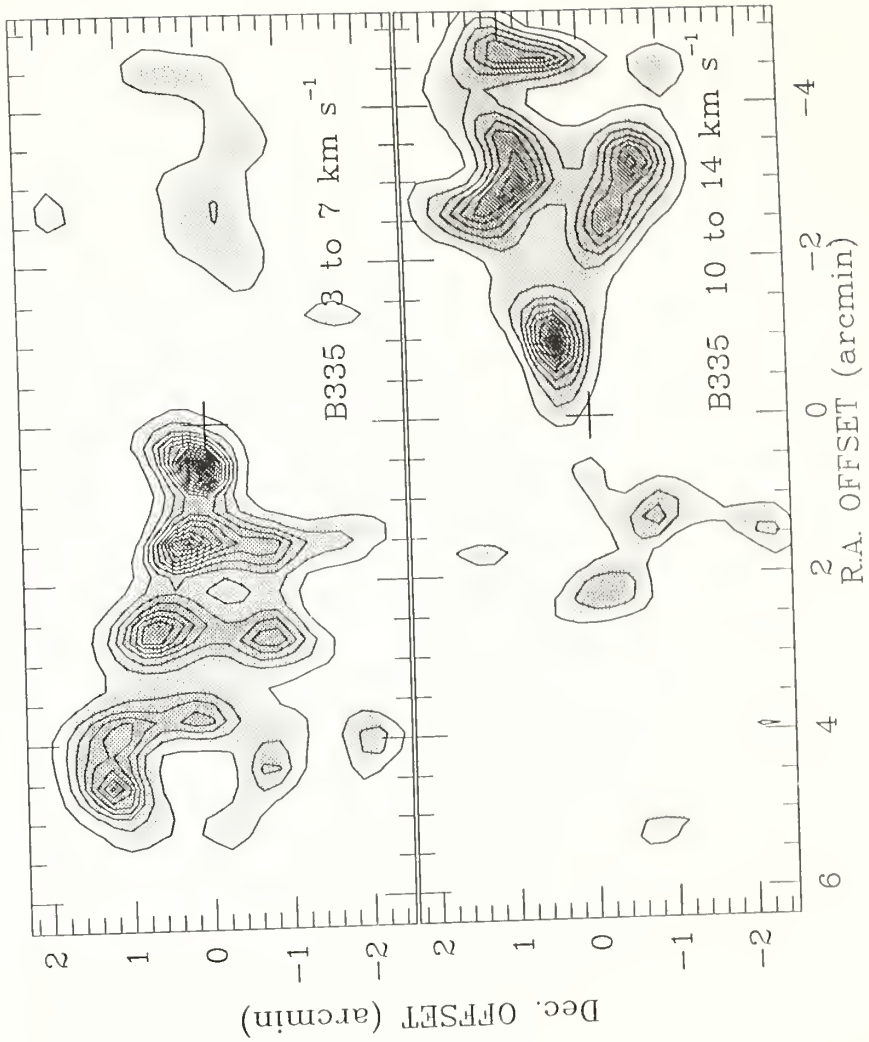


Figure 5.4

These spatial-velocity maps were made from the unreconstructed spectra along cuts through the outflow parallel to the outflow axis. Several adjacent spectra were averaged together centered at declination offsets $+1.2'$ (top panel), $0'$ (center panel) and $-1.2'$ (bottom panel). Note how the highest velocity emission is found at the point where the ambient emission disappears to the west of the outflow. Ambient emission is also seen to disappear to the east of the outflow. Contour levels are .25, .5, .75, 1, 1.5, 2, 2.5, ... K.

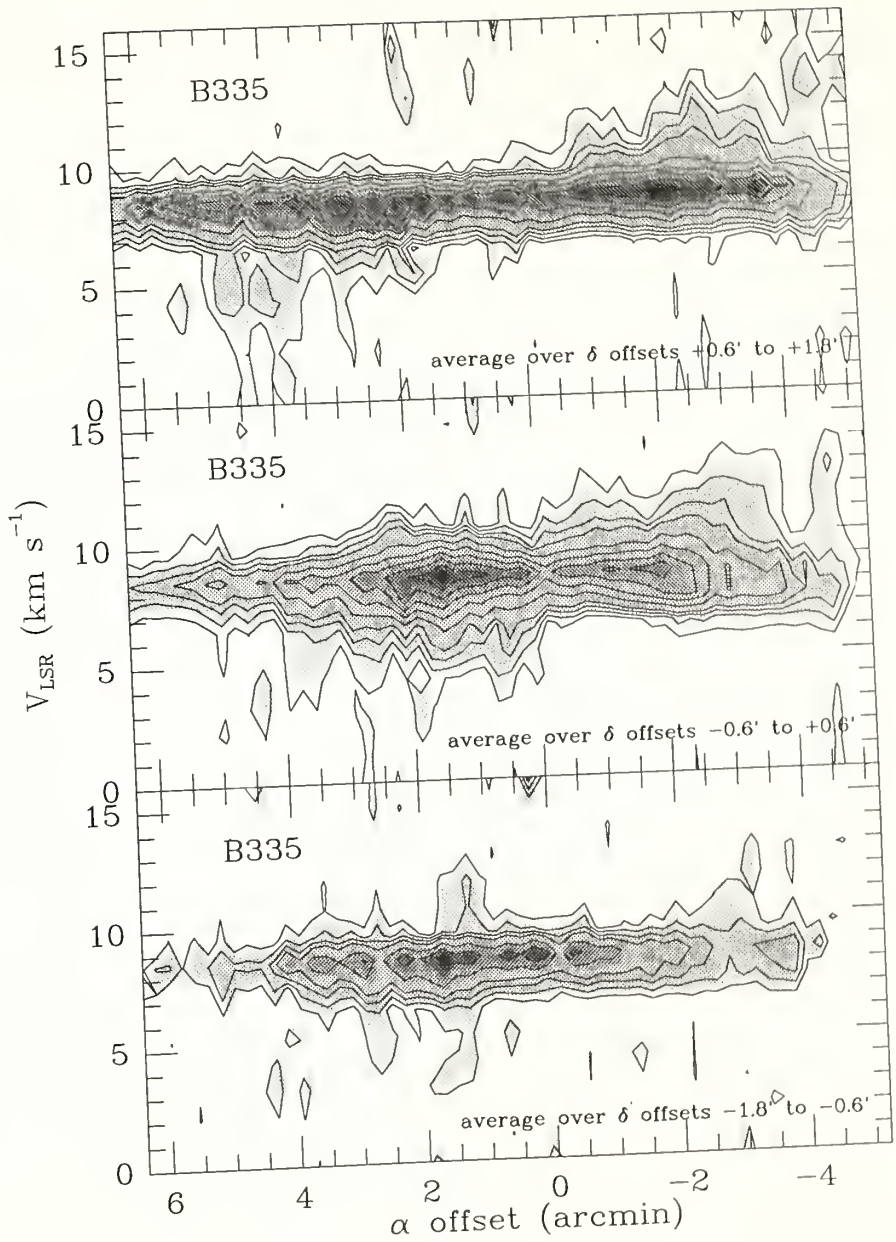


Figure 5.5

In this figure are presented half-tone/contour maps of the red-shifted and blue-shifted emission of the L723 molecular outflow at different velocity intervals. The integrated intensity ($\int I_R dv$) within each velocity interval (indicated on each map) was determined, and then each map was reconstructed using maximum entropy. The map was fully sampled within the region bordered by the dotted line shown on the maps of the -2 to 2 km s^{-1} and 18 to 22 km s^{-1} intervals. The contour levels are $.5, 1, 2, 3, \dots$ K km s^{-1} . The cross marks the position of the far infrared star discovered by Davidson (1983, private communication to Goldsmith *et al.* 1984) with coordinates R.A.(1950) = $19^h 15^m 42^s$, Dec.(1950) = $+19^\circ 06' 49''$. Offsets are in arcminutes from this position. Both the red and blue lobes of the outflow are very narrow highly collimated, and are not resolved. There is no indication of shell structure. There are two axes of symmetry of the outflow, one running roughly east-west and the other running roughly north-south.

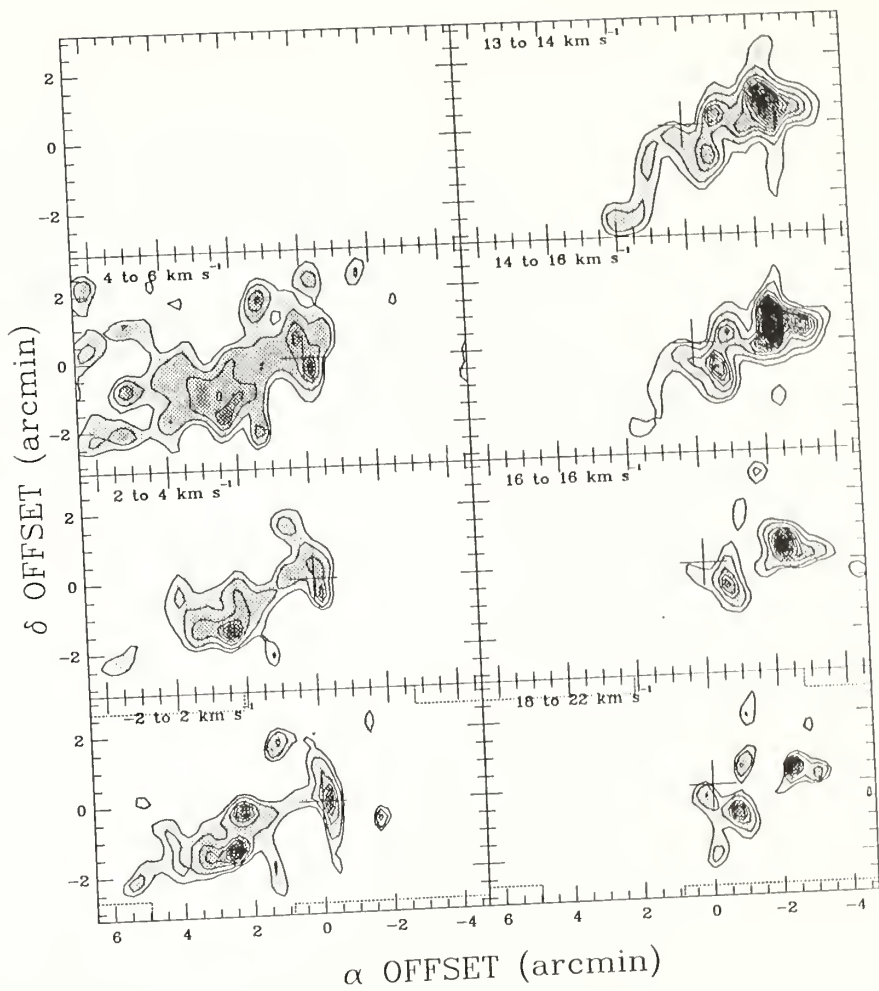


Figure 5.6

The raw, unreconstructed maps of the L723 outflow are shown in this figure. Offsets, symbols, and contours are the same as in Figure 5.5.

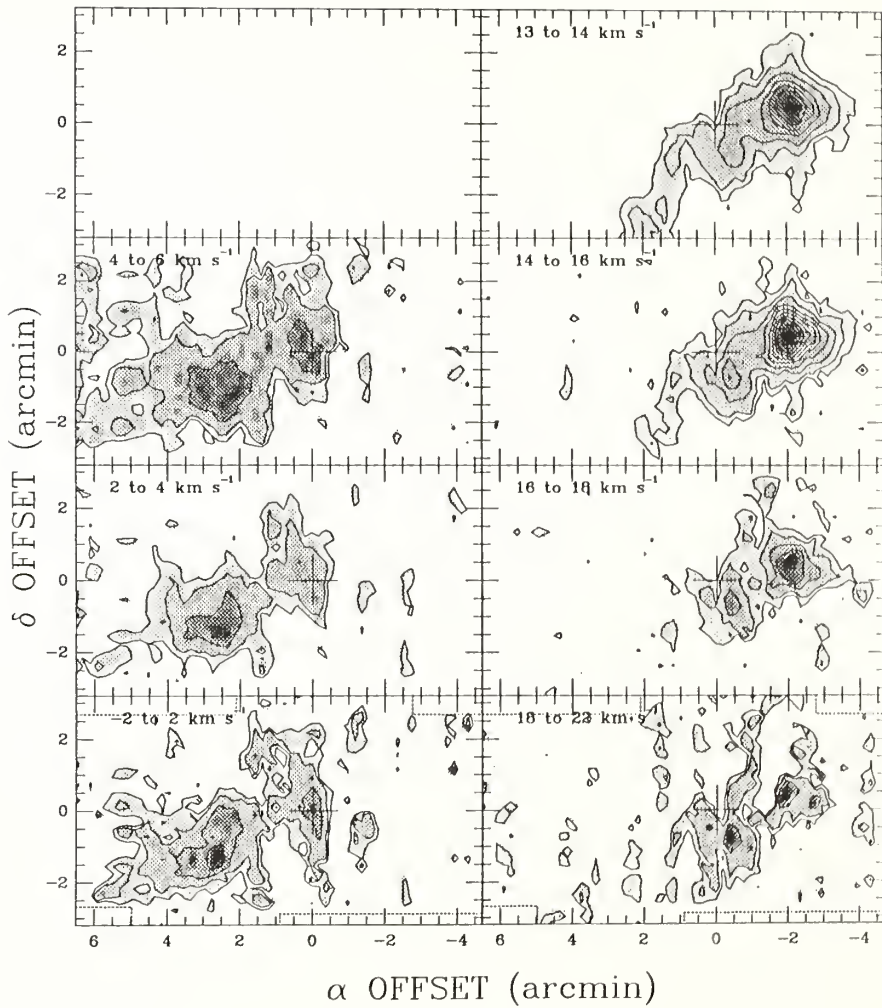


Figure 5.7

The integrated intensity over the entire red- and blue-shifted line wings are presented here. Offsets and symbols are as in Figure 5.5. Contours are .5, 1, 2, 4, 8, 12, 16,... K km s⁻¹. Note the curious sinuous feature in the red-shifted emission (13 to 22 km s⁻¹) extending east of the far infrared star and which traces the southern limb of the blue lobe.

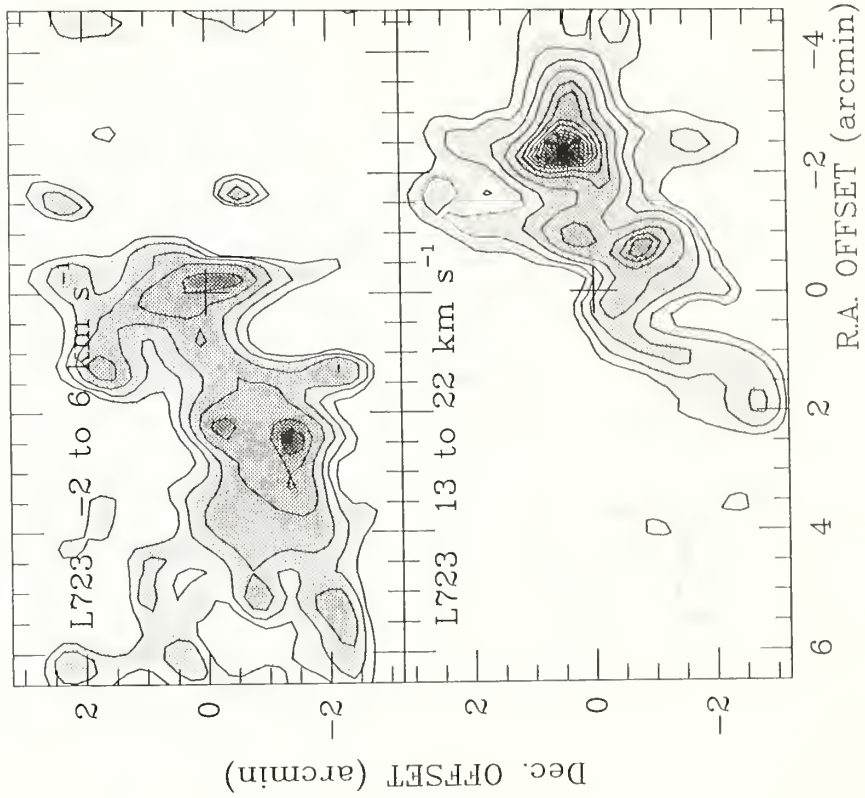
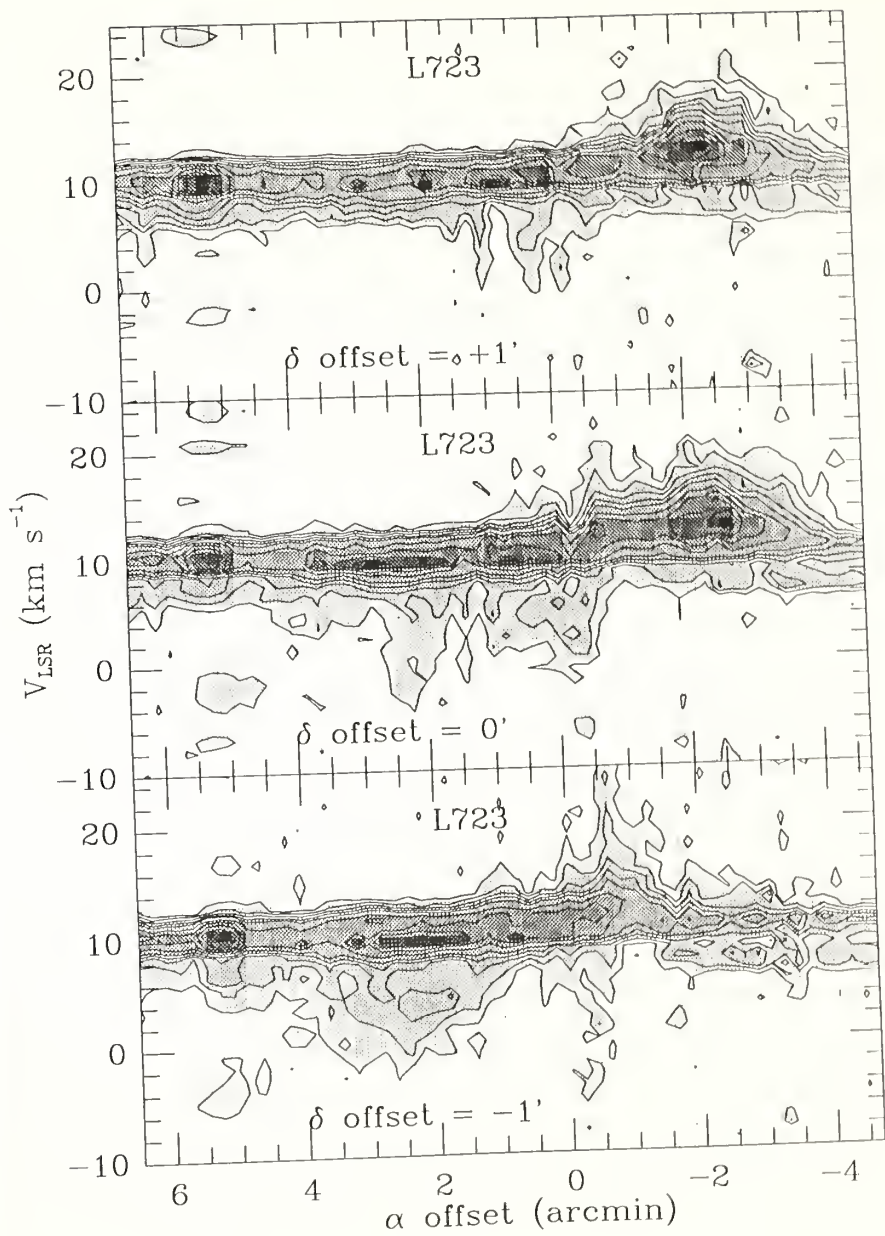


Figure 5.8

Shown here are three spatial-velocity diagrams which have been generated from unreconstructed spectra of the L723 outflow. Each was made along a cut through the outflow parallel to the right ascension axis at a declination offset of $+1'$ (top panel), $0'$ (center panel), and $-1'$ (bottom panel) from the central far infrared star. Right ascension offsets are the same as in Figures 5.5.



Chapter 6

Summary

I. Maximum Entropy

The most important question one can ask about the use of this technique is whether it is useful. Does the technique work? The best answer to this question can be provided by comparison of the reconstructed images with maps made of the same objects by other telescopes with intrinsically higher resolution. Such maps have been made at the Nobeyama Radio Observatory (which has an angular resolution of about 15" at the same frequency as that used for our maps) of most of the L1551 outflow (by Uchida *et al.* 1987) and of part of the L723 outflow (by Hayashi *et al.* 1987). We find that the same structures seen in their maps are found in ours, and our maps show no spurious features. The maps of the L1551 outflow from Uchida *et al.* (1987) are reproduced in Figure 6.1 at the same scale as Figure 4.1 for direct comparison. From this standpoint alone, the use of the maximum entropy technique would seem to be successful. However, there are some limitations to this technique. It is necessary to acquire many spectra covering the beam of the telescope, and the need for good signal-to-noise ratios means that large amounts of observing time are needed for such a project. In addition, maximum entropy is a non-linear technique, so that the effective resolution of a map changes over the image. It would therefore probably not be a useful tool in calculating optical depths, where the ratios of emission which are used to calculate such quantities might be altered by differing effective resolutions. Nevertheless, for a given telescope such as the Five College Radio Astronomy Observatory, MESM provides a useful and effective means of improving angular resolution and at the same time smoothing without loss of resolution where the signal-to-noise is moderate.

II. Bipolar Outflows

The L1551 molecular outflow is concentrated in a thin shell, which has a thickness of <0.03 pc, surrounding a cavity which has been mostly evacuated of molecular material. This shell is expanding, and has a constant opening angle of about 70° in the red and blue lobes. In the inner part of the outflow where the lobes show a constant opening angle, the molecular emission shows a apparent acceleration as it moves away from IRS-5, produced by a projection effect caused by the molecular shell moving radially away from IRS-5 with a latitude dependent velocity, or true acceleration caused by hydromagnetically driven winds (Pudritz and Norman, 1983 and 1986; Uchida and Shibata, 1985). The blue lobe becomes recollimated, but the red lobe expands to the end of the outflow. Although the hydromagnetic models do generate collimated outflows, the pressure of the ambient molecular cloud is itself sufficient to provide the force to recollimate the blue lobe. Where the blue lobe becomes recollimated, there is an abrupt velocity decrease and a sudden narrowing or "pinch" of the lobe. The ends of the outflow have walls of molecular material stopping the wind and which are still moving through the cloud. In one location at the end of the blue lobe, however, molecular wind appears to have broken out of the cloud, and is being reaccelerated.

The energy within the outflow is greater than the energy of the entire cloud. In addition, the momentum of the outflow is sufficient to disrupt the core of the cloud. Thus, such outflows may play a significant role in preventing the cloud from forming large numbers of stars at free-fall timescales. The L1551 molecular cloud core as traced by CS emission shows an elongated, dense structure alligned nearly perpendicular to the outflow axis which may be material left over in the core of the cloud after the outflow has swept away most of the dense material parallel to the flow axis. Dense "clumps" within this elongated structure show evidence for an east-west velocity gradient, indicated perhaps that the cloud core is in the process of being disrupted or sheared by the high energy outflow.

A high density ridge is seen to trace the north-west limb of the blue lobe, and is also seen in the column density profile of the cloud as traced by ^{13}CO emission. This dense ridge is coincident with red-shifted emission found along the limbs of the blue lobe, and blue-shifted emission along the south-east limb of the red lobe. This emission is unlikely to be related to rotation of the outflow, since there is weak red-shifted emission along both the north-west and south-west periphery of the lobe. Instead, perhaps the emission results from streaming (or "splash") of the molecular wind around the dense structures found at these locations, or perhaps is an unusually large velocity dispersion caused by the interaction of a high velocity wind from IRS-5 interacting with the molecular shell.

From these observations, it must be concluded that these data are most consistent with a model where the molecular wind has been swept up by a high velocity, neutral, perhaps latitude dependent wind from IRS-5. Indeed, the reacceleration of the molecular wind after it has escaped from the cloud seems to point directly at such a high velocity wind as far as 0.9 pc from IRS-5.

The B335 outflow seems to have a similar structure to L1551. It has significant limb brightening, and has red-shifted emission in the center of the blue lobe and blue-shifted emission in the center of the red lobe, all of which suggests a shell structure similar to that of L1551. The orientation of the outflow can be estimated to be $\sim 8^\circ$ out of the plane of the sky. The energy of this outflow is nearly the same as that of the cloud, and has momentum sufficient to disrupt the core of the cloud. At both ends of the outflow, the molecular wind may have broken out of the cloud and appears to have been reaccelerated. There is also evidence that wind has crossed a void in the cloud to the east of the outflow and has reentered the cloud further east, continuing the outflow. The structure of this outflow is consistent with the same model for L1551, that the molecular wind is being swept up by a high velocity wind originating from the central star, IRS-1.

L723, however, remains an enigma, largely, perhaps, because it has not been resolved

by our observations. It has no apparent shell structure and no apparent acceleration. The presence of high velocity emission down the center of the east blue lobe could be equally well explained as evidence for an expanding shell or as a sign of flow down a viscous pipe. Its most curious feature is the presence of two axes of symmetry which are oriented nearly perpendicular to each other, which might be due to precession of the outflow axis.

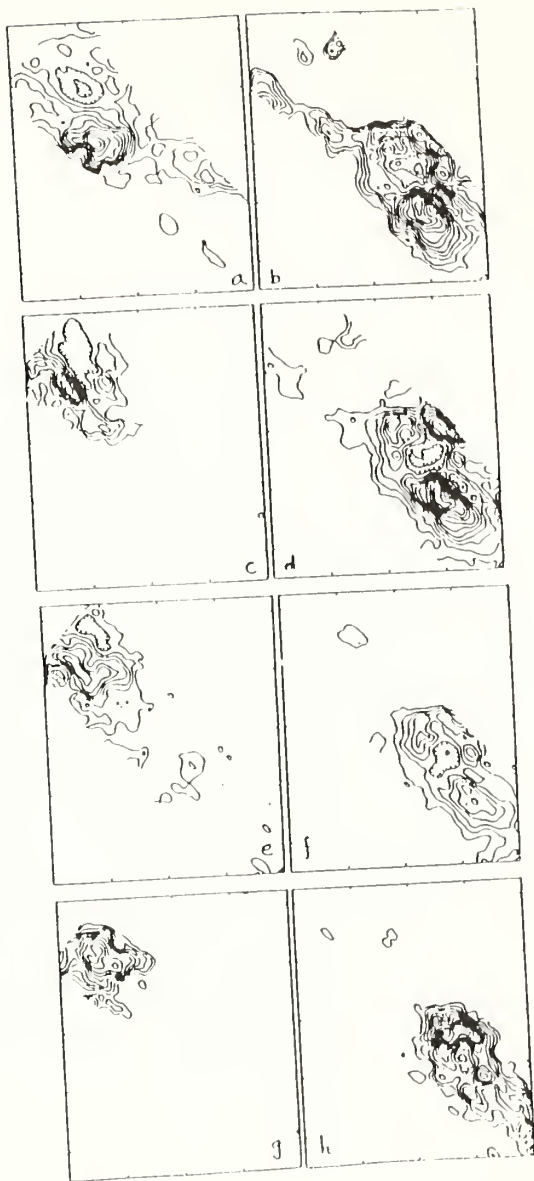
III. Further Observations

Most models explaining the origin of these outflow, whether the hydromagnetic acceleration model or wind generated near the protostar due to accretion, require the presence of a disk surrounding the central young stellar object; the former requires a large rotating disk (whose existence is now doubtful) and the latter a much smaller one. Continuum measurements of the L1551, B335 and L723 in at $1100\ \mu$ by Sandell (1987, private communication) show an elongated structure of size <1 arcminute perpendicular to the outflow axis, but it is not certain if these are disks in the accepted sense or not yet disrupted cores. The small-scale dynamics of such disk-like structures are needed in order to understand their role in the outflow stage of young stellar objects. Millimetre interferometers would provide the spatial resolution needed for such a study, but as yet lack the necessary velocity resolution. Higher transitions of density tracers (such as CS) using a sub-millimetre telescope may provide sufficient angular resolution to resolve the velocity structure of the warm, dense gas surrounding the protostar.

It is possible that the L723 outflow may have an as yet unresolved shell structure. Interferometer maps of this outflow may reveal such structure. The nature of the twin axes of symmetry remains an intriguing puzzle. If HCO^+ is a tracer of the denser wind in a warm, partly ionized medium, then observations of this molecule made at perhaps the Nobeyama Radio Observatory may reveal the current state of the outflowing wind. In other words, has the axis of the outflow precessed and is the wind driving the outflow oriented north-south, or is the wind blowing in two directions at once.

Figure 6.1

The L1551 outflow has also been mapped by Uchida *et al.* (1987) using the Nobeyama Radio Observatory which has an angular resolution of $15''$ at the $^{12}\text{CO J}=1-0$ transition. This figure reproduces the maps from Uchida *et al.* (1987). Figures a, c, e, and g are red-shifted contour maps with radial velocity $v_r = 1.5 \pm 0.5, 4 \pm 0.5, 7.5 \pm 0.5,$ and $11.5 \pm 2.5 \text{ km s}^{-1}$ relative to the rest velocity of the molecular cloud of 6.7 km s^{-1} , and b, d, f, and h are blue-shifted contour maps with $v_r = -1.5 \pm 0.5, -2.5 \pm 0.5, -4.5 \pm 0.5,$ and $-8.5 \pm 2.5 \text{ km s}^{-1}$ respectively. These figures can be compared to Figure 4.1 to show that our maximum entropy results are consistent with maps made at intrinsically higher angular resolution. All of the features visible here in Figure 6.1 can be seen in Figure 4.1, and vice versa.



Appendix A: Derivation of the Maximum Entropy Algorithm

The derivation of the maximum entropy algorithm used in this work follows that presented by Willingdale (1981) for use in X-ray image reconstruction. Some simplifying assumptions have been made, however (see also Grasdalen, Gehrz and Hackwell, 1983). The observations in this work were all made using a single detector so that all points in the map have equal weight. Furthermore, the astronomical signal at millimetre wavelengths is much smaller than the background noise from the sky and the telescope, so that the noise can be characterized by a gaussian distribution.

We define the entropy of an image:

$$S = -\sum_i f_i \ln f_i \quad (\text{A1.1})$$

where f_i is the flux detected in the i^{th} cell. An observed data point can be defined as:

$$d_i = \sum_j B_{ij} p_j + n_i \quad (\text{A1.2})$$

where B_{ij} is the point response of the system (*ie.* beam profile), p_j is the true flux at a point, and n_i is the noise. We also define:

$$\hat{d}_i = \sum_j B_{ji} \hat{f}_j \quad (\text{A1.3})$$

where \hat{f}_i is the estimate of p_i .

Because the statistics of the image are gaussian, the χ^2 statistic can indicate the "goodness of fit" of the estimate \hat{f} , while the entropy defines the most likely \hat{f} from those having a similar χ^2 . In addition, we require that the total flux be conserved. We can then define the so-called "Objective Function":

$$Q = -\sum_i \hat{f}_i \ln \hat{f}_i - \lambda \sum_i \frac{(\hat{d}_i - d_i)^2}{\sigma_i^2} \quad (\text{A1.4})$$

where the first term is the entropy, the second term is the χ^2 , and λ is a lagrange multiplier. To find the maximum entropy solution, the entropy must be maximized and the χ^2 minimized at the solution \hat{f} . We take the derivative of A1.4:

$$\frac{dQ}{d\hat{f}_i} = -\ln \hat{f}_i - 1 - \sum_k \frac{2\lambda B_{ki} (\hat{d}_k - d_k)}{\sigma_k^2} = 0 \quad (A1.5)$$

$$\ln \hat{f}_i = -1 - \sum_k \frac{2\lambda B_{ki} (\hat{d}_k - d_k)}{\sigma_k^2} \quad (A1.6)$$

$$\hat{f}_i = \exp(-1) \exp\left(\sum_j \frac{-2\lambda}{\sigma_j^2} B_{ji} (\hat{d}_j - d_j)\right) \quad (A1.7).$$

To preserve flux constancy, a normalization factor is applied to the equation. In addition, the factor $\frac{2\lambda}{\sigma_i^2}$ is constant over the image, so let $\frac{2\lambda}{\sigma_i^2} \equiv \lambda$. Then writing A1.7 in terms of two-dimensional arrays, we have the maximum entropy algorithm:

$$R = N \exp \left\{ \lambda (B * D - B * B * R) \right\} \quad (A1.8)$$

where * refers to the convolution operator, B is the beam profile, D is the raw data, and R is the maximum entropy solution.

Appendix B: Maximum Entropy FORTRAN Program

```
PROGRAM MESM
C.....IMAGE RECONSTRUCTION PROGRAMME. VERSION 85-01-21 BY
C.....GERALD MORIARTY-SCHIEVEN. MODIFIED 86-08-02, 86-11-08.
C.....THIS PROGRAM PERFORMS A MAXIMUM-ENTROPY STATISTICAL METHOD
C.....RECONSTRUCTION ON A TWO-DIMENSIONAL IMAGE.
C.....IT REQUIRES THE IMSL MATH LIBRARY TO BE ATTACHED.
C.....THE FOLLOWING FILES ARE READ BY THE PROGRAM AND MUST BE ATTACHED
C.....TO THE JOB:
C..... TAPE1 = FILE CONTAINING RAW DATA. BE SURE THE READ STATEMENTS
C..... REFLECT THE FORMAT OF THE STORED DATA. THIS TAPE FILE
C..... MUST BE ATTACHED FOR ALL RUNS OF THE PROGRAMME.
C..... TAPE6 = THIS TAPE FILE MUST BE ATTACHED FOR EVERY RUN OF THE
C..... PROGRAM *EXCEPT* THE FIRST ONE. IT CONTAINS CONSTANT
C..... ARRAYS SUCH AS B*B, B*D, ETC. WHICH THE PROGRAM USES IN
C..... THE CALCULATIONS.
C..... TAPE7 = THIS TAPE FILE MUST BE ATTACHED FOR EVERY RUN OF THE
C..... PROGRAM *EXCEPT* THE FIRST ONE. IT CONTAINS THE PREVIOUS
C..... MAXIMUM ENTROPY SOLUTION WHICH IS USED AS THE INITIAL
C..... TRIAL SOLUTION.
C.....THE FOLLOWING FILES ARE CREATED BY THE PROGRAM AND MUST BE SAVED
C.....AT THE END OF THE JOB.
C..... TAPE3 = CONTAINS INFORMATION ON EACH ITERATION AND CAN BE USED
C..... AS A DIAGNOSTIC IN CASE THE PROGRAM FAILS OR ABORTS.
C..... TAPE4 = CONTAINS THE NEW MAXIMUM ENTROPY SOLUTION.
C..... TAPE5 = CREATED DURING THE FIRST RUN OF THE PROGRAM *ONLY*.
C..... CONTAINS THE CONSTANT ARRAYS WHICH ARE LATER ACCESSED AS
C..... TAPE6.
C.....ALL OTHER TAPE FILES ARE SCRATCH FILES WHICH NEED NOT BE ACCESSED
C.....OR SAVED.
C.....SUGGESTIONS FOR PERFORMING MAXIMUM ENTROPY:
C..... START WITH ALAMDA=1, THEN INCREMENT ALAMDA BY 2 OR 4 FOR EACH
C..... SUBSEQUENT SOLUTION. DURING THE FIRST RUN (IE. ALAMDA=1), PUT
C..... IFIRST=1, AND LET
C..... IFIRST = 2 FOR THE REST OF THE SOLUTIONS.
C..... IF THE PROGRAM WON'T CONVERGE OR HITS A TIME LIMIT (SEE THE
C..... DAYFILE), TRY INCREASING THE CONVERGENCE TOLERANCE OR INCREASING
```



```

C....NROWS= NUMBER OF ROWS IN THE MAP OR IMAGE.
      NCOLS=56
C....NCOLS= NUMBER OF COLUMNS IN THE MAP OR IMAGE.
      NROWS=32
C....DATSPAC= DISTANCE BETWEEN SAMPLE POINTS IN ARC-SECONDS.
      DATSPAC=12.
C....HPBW= HALF-POWER BEAM-WIDTH OF THE GAUSSIAN BEAM PROFILE IN
C....      ARCSECONDS.
      HPBW=45.
C....ALAMDA= VALUE OF LAMDA DESIRED FOR THIS MAXIMUM-ENTROPY
C....      RECONSTRUCTION.
      ALAMDA=1.
C....WT= INITIAL VALUE OF WEIGHT PER ITERATION.
      WT=2.

C
C*****
C
C....ARMED WITH THIS DATA, READ IN THE REAL IMAGE DATA AND STORE IN A
C....COMPLEX ARRAY.
C
      READ(1,32) ITITLE
      READ(1,32) LABEL
      DO 2 I=1,NROWS
        DO 1 J=1,NCOLS
          READ(1,*) DALP(I,J),DDEC(I,J),DATUM
          IMAGE(I,J)=CMLX(DATUM)
1          CONTINUE
2          CONTINUE

C
C....IF THIS IS NOT THE FIRST TIME THIS PROGRAM HAS BEEN USED ON THIS
C....MAP TO GENERATE A MAXIMUM-ENTROPY SOLUTION, IE. IF IFIRST.NE.1,
C....THEN READ IN B, B*B, B*D, AND SOME NECESSARY CONSTANTS, FROM
C....      TAPE6.
C
      IF(IFIRST.EQ.1) GO TO 17

C
C....FIRST READ THE NECESSARY CONSTANTS.
C
      READ(6,*) AREA

```

```

C
C.....NOW INPUT THE FOURIER TRANSFORMED, COMPLEX BEAM ARRAY.
C
      DO 19 I=1,NROWS
          DO 18 J=1,NCOLS
              READ(6,*) BEAM(I,J)
18      CONTINUE
19 CONTINUE
C
C.....READ IN TRANSFORMED COMPLEX ARRAY BEAM*BEAM (B*B).
C
      DO 21 I=1,NROWS
          DO 20 J=1,NCOLS
              READ(6,*) BB(I,J)
20      CONTINUE
21 CONTINUE
C
C.....INPUT COMPLEX, UNTRANSFORMED ARRAY BEAM*DATA (B*D).
C
      DO 23 I=1,NROWS
          DO 22 J=1,NCOLS
              READ(6,*) BD(I,J)
22      CONTINUE
23 CONTINUE
C
C.....NOW READ IN PREVIOUS MAXIMUM-ENTROPY SOLUTION FROM TAPE7 AND
C.....CONVERT TO A COMPLEX ARRAY.
C
      READ(7,32) ITITLE
      READ(7,32) INFSOLN
      READ(7,32) LABEL
32 FORMAT(A80)
      DO 25 I=1,NROWS
          DO 24 J=1,NCOLS
              READ(7,*) DUMMY1,DUMMY2,DATUM
              RN(I,J)=CMLPX(DATUM)
24      CONTINUE
25 CONTINUE
C

```

```

C.....NOW WE CAN BEGIN THE ITERATIONS FOR THE NEXT SOLUTION.
C
      GO TO 9
C
C.....FIND AREA UNDER IMAGE FOR USE IN SCALING.
C
      17 AREA=0.0
         DO 4 I=1,NROWS
            DO 3 J=1,NCOLS
               AREA=AREA+REAL (IMAGE (I, J))
            3      CONTINUE
         4 CONTINUE
C
C.....WRITE THIS INFORMATION TO TAPES.
      WRITE (5, *) AREA
C
C.....GENERATE THE GAUSSIAN BEAM PROFILE.
C.....CALCULATE THE NUMBER OF POINTS PER HALF-BEAM-WIDTH OF GAUSSIAN
C.....BEAM PROFILE.
C
      SPBW=HPBW/DATSPAC
C
C.....NOW CALCULATE FACTORS (LIKE 2*SIGMA**2) USED IN CALCULATING THE
C.....TWO-DIMENSIONAL GAUSSIAN PROFILE.
C
      TSIGSQ=((SPBW/2.)**2)/ALOG(2.)
      TPSIGSQ=TSIGSQ*3.14159
C
C.....NOW GENERATE GAUSSIAN PROFILE.
C
      K=NROWS/2
      L=NCOLS/2
      ANORM=0.0
      DO 6 I=1,NROWS
         DO 5 J=1,NCOLS
            IF (I.LE.K) XX=FLOAT (I) -1.
            IF (I.GT.K) XX=FLOAT (NROWS-I) +1.
            IF (J.LE.L) YY=FLOAT (J) -1.
            IF (J.GT.L) YY=FLOAT (NCOLS-J) +1.

```

```

EFACT=(-1.*(XX**2 + YY**2)/TSIGSQ)
IF(EFACT.LE.(-30)) THEN
    RBEEM=0.0
ELSE
    RBEEM=EXP(EFACT)/TPSIGSQ
END IF
ANORM=ANORM+RBEEM
BEAM(I,J)=CMLX(RBEEM)
5     CONTINUE
6     CONTINUE
DO 41 I=1,NROWS
    DO 40 J=1,NCOLS
        BEAM(I,J)=BEAM(I,J)/ANORM
40     CONTINUE
41     CONTINUE
C
C.....CREATE B*B AND B*D.
C.....THE BEAM PROFILE IS ONLY EVER NEEDED IN FOURIER TRANSFORMED STATE.
C
    CALL FFT(BEAM,1)
C
C.....WRITE TRANSFORMED BEAM TO TAPE5.
C
    DO 31 I=1,NROWS
        DO 30 J=1,NCOLS
            WRITE(5,*) BEAM(I,J)
30     CONTINUE
31     CONTINUE
C
C.....THE IMAGE IS NEEDED IN ITS ORIGINAL FORM, SO TRANSFER THE IMAGE
C.....TO A TEMPORARY FILE IN ORDER TO DO CONVOLUTIONS.
C
    CALL BUFF(IMAGE,BUFR)
    CALL FFT(BUFR,1)
C
C.....NOW CONVOLVE BEAM WITH BEAM AND BEAM WITH IMAGE.
C
    CALL CONVOL(BEAM,BEAM,BB)
    CALL CONVOL(BEAM,BUFR,BD)

```

```
C
C.....WRITE TRANSFORMED B*B TO TAPES5.
C
  DO 27 I=1,NROWS
    DO 26 J=1,NCOLS
      WRITE(5,*) BB(I,J)
26    CONTINUE
27 CONTINUE

C
C.....TAKE INVERSE TRANSFORMS OF B*D. (B*B IS LEFT IN TRANSFORMED FORM.)
C
  CALL FFT(BD,-1)

C
C.....WRITE B*D TO TAPES5.
C
  DO 29 I=1,NROWS
    DO 28 J=1,NCOLS
      WRITE(5,*) BD(I,J)
28    CONTINUE
29 CONTINUE

C
C.....CREATE LAMDA=0 SOLUTION TO USE AS THE INITIAL TRIAL IMAGE.
C
  A=AREA/FLOAT(NROWS*NCOLS)
  DO 8 I=1,NROWS
    DO 7 J=1,NCOLS
      RN(I,J)=A
7    CONTINUE
8 CONTINUE

C
C.....INITIALIZE WEIGHT PER ITERATION.
C
9 PCNVG=1.E30
  NEVEN=1
  N=1
  NA=0

C
C.....ITERATION STARTS AT THE NEXT INSTRUCTION.
C.....CALCULATE B*B*RN. FIRST TRANSFER RN TO A TEMPORARY BUFFER.
```

```

C
  10 CALL BUFF(RN,BUFR)
C
C.....TAKE FOURIER TRANSFORM IN PREPARATION FOR CONVOLUTION.
C
  CALL FFT(BUFR,1)
C
C.....DO THE CONVOLUTION.
C
  CALL CONVOL(BB,BUFR,BBRN)
C
C.....TAKE THE INVERSE TRANSFORM OF BBRN.
C
  CALL FFT(BBRN,-1)
C
C.....NOW CALCULATE RPRIME.
C
  CALL RPRIME
C
C.....CALCULATE THE DIFFERENCE BETWEEN RPRIM AND RN TO TEST FOR
C.....  CONVERGENCE.
C
  CNVG=RMSDIF()
C
C.....BEFORE TESTING FOR CONVERGENCE, CALCULATE R(N+1)
C
  CALL RNPLUS(WT)
C
C.....WRITE ITERATION INFORMATION TO TAPE3.
C
  WRITE(3,11) N,ALAMDA,WT,CNVG
  11 FORMAT(1X,'N=',I5,2X,'LAMDA=',F10.0,2X,'WT=',F10.2,
  *      2X,'CNVG=',E11.4)
C
C.....IS THE TEST FOR CONVERGENCE DECREASING WITH EACH ITERATION?
C.....IF NOT, INCREASE WEIGHT AND TRY AT NEXT ITERATION.
C
  IF(CNVG.GT.PCNVG) THEN
    NEVEN=NEVEN+1

```



```

        IF (NEVEN.GT.3) THEN
            NEVEN=1
            WT=WT*SQRT(2.)
            NA=NA+1
        END IF
    END IF
C
C.....IF WE HAVE TO INCREASE THE WEIGHT TOO OFTEN, SOMETHING IS WRONG.
C
    IF (NA.GT.56) THEN
        CALL REMARK('MESM WONT CONVERGE')
        STOP 2
    END IF
C
C.....LET THE PRESENT VALUE OF CNVG NOW BE THE PREVIOUS VALUE.
C
    PCNVG=CNVG
    N=N+1
C
C.....NOW TEST FOR CONVERGENCE. IF THE RMS DIFFERENCE IS LESS THAN 0.5%,
C.....THE ITERATIONS ARE FINISHED.
C
    IF (CNVG.GE.(0.005)) GO TO 10
C
C.....NOW CALCULATE CHI-SQUARE DIFFERENCE BETWEEN B*RN AND D.
C
    CHSQR=CHISQR()
C
C.....WRITE SOLUTION TO TAPE4.
C
    WRITE(4,32) ITITLE
    WRITE(4,16) N,ALAMDA,WT,CHSQR,CNVG
16 FORMAT(1X,'N=',I5,2X,'LAMDA=',F10.0,2X,'WT=',F10.2,
*        'CHISQR=',E11.4,2X,'CNVG=',E11.4)
    WRITE(4,32) LABEL
    CALL DATAPR
C
C.....ALL FINISHED.
C

```

END

C
C
C
C
C

SUBROUTINE DATAPR

C.....PRINTS TO TAPE4 THE REAL PART OF RPRIM.

COMMON /ASIZE/NROWS,NCOLS

COMMON /COORD/DALP,DDEC

COMMON /RD/ RPRIM,RN

COMPLEX RPRIM,RN

DIMENSION RPRIM(56,32),RN(56,32),DALP(56,32),DDEC(56,32)

C

DO 2 I=1,NROWS

DO 1 J=1,NCOLS

DAT=REAL(RN(I,J))

WRITE(4,3) DALP(I,J),DDEC(I,J),DAT

1 CONTINUE

2 CONTINUE

3 FORMAT(1X,3(E12.5,1X))

RETURN

END

C
C
C
C
C

SUBROUTINE RNPLUS(WT)

C.....CALCULATES THE VALUE OF R(N+1).

C

COMMON /ASIZE/ NROWS,NCOLS

COMPLEX RPRIM,RN

DIMENSION RPRIM(56,32),RN(56,32)

COMMON /RD/ RPRIM,RN

C

C.....CALCULATE WEIGHTS.

C

W1=WT/(WT+1.)

```

      W2=1./(WT+1.)
C
C.....NOW CALCULATE NEXT ITERATION
C
      DO 2 I=1,NROWS
        DO 1 J=1,NCOLS
          RN(I,J)=W1*RN(I,J) + W2*RPRIM(I,J)
1      CONTINUE
2 CONTINUE
      RETURN
      END
C
C
C
C
C
      FUNCTION RMSDIF()
C.....CALCULATES THE RMS DIFFERENCE BETWEEN RPRIM AND RN.
C
      COMMON /ASIZE/ NROWS,NCOLS
      COMPLEX RPRIM,RN,A,B
      DIMENSION RPRIM(56,32),RN(56,32)
      DIMENSION A(56,32),B(56,32)
      COMMON /RD/ RPRIM,RN
      COMMON /RP/ A,B,AREA,C
C
      VOL=0.0
      DO 2 I=1,NROWS
        DO 1 J=1,NCOLS
          VOL=VOL + SQRT(REAL(RPRIM(I,J)-RN(I,J))**2)
1      CONTINUE
2 CONTINUE
      VOL=VOL/AREA
      RMSDIF=VOL
      RETURN
      END
C
C
C

```

```

C
C
SUBROUTINE RPRIME
C.....CALCULATES THE CORRECTION TO THE MAXIMUM ENTROPY ITERATION.
C.....      RPRIM=N*EXP(LAMDA*(BD-BBRN))
C
COMMON /ASIZE/ NROWS,NCOLS
COMMON /COMPLEX/ BD,BBRN,RPRIM,RN
COMMON /DIMENSION/ BD(56,32),BBRN(56,32)
COMMON /RPRIM/ RPRIM(56,32),RN(56,32)
COMMON /AREA/ AREA,ALAMDA
COMMON /VOL/ VOL
VOL=0.0

C
C.....CALCULATE UNSCALED RPRIM. IF WE GET EXP(X) OVERFLOWING, CALCULATE
C.....RPRIM IN A DIFFERENT WAY.
C
DO 2 I=1,NROWS
  DO 1 J=1,NCOLS
    X=ALAMDA*(BD(I,J)-BBRN(I,J))
    IF(X.GT.(40.)) GO TO 5
    RPRIM(I,J)=EXP(X)
    VOL=VOL+RPRIM(I,J)
1     CONTINUE
2     CONTINUE

C
C.....SCALE RPRIM.
C
S=AREA/VOL
DO 4 I=1,NROWS
  DO 3 J=1,NCOLS
    RPRIM(I,J)=S*RPRIM(I,J)
3     CONTINUE
4     CONTINUE
RETURN

C
C.....IF WE WOULD HAVE HAD AN OVERFLOW WITH 'EXP(X)', REDO CALCULATING
C.....RPRIM USING LOGARITHMS. USE LN(RPRIM)=LAMDA*(BD-BBRN)
C

```

```

5 AMAX=0.0
  DO 7 I=1,NROWS
    DO 6 J=1,NCOLS
      RPRIM(I,J)=ALAMDA*(BD(I,J)-BBRN(I,J))
      IF (REAL(RPRIM(I,J)).GT.AMAX) AMAX=RPRIM(I,J)
6     CONTINUE
7 CONTINUE

```

C
C.....WE ALREADY KNOW THAT AMAX IS GREATER THAN 40. NOW LET'S FIND
C.....WHAT FACTOR WILL REDUCE LN(RPRIM) TO A MANAGEABLE LEVEL.
C

```

      DIVFAC=2.
8     DIV=(DIVFAC-1.)/DIVFAC
      IF ((AMAX-DIV).LE.40) GO TO 9
      DIVFAC=DIVFAC+1.
      GO TO 8

```

C
C.....SCALE LN(RPRIM) BY THIS FACTOR AND FIND RPRIM.

C

```

9     VOL=0.0
      DO 11 I=1,NROWS
        DO 10 J=1,NCOLS
          RPRIM(I,J)=RPRIM(I,J)-DIV
          IF (REAL(RPRIM(I,J)).LT.(-40.)) THEN
            RPRIM(I,J)=0.0
            GO TO 10
          END IF
          RPRIM(I,J)=EXP(RPRIM(I,J))
          VOL=VOL+RPRIM(I,J)
10     CONTINUE
11 CONTINUE

```

C
C.....NORMALIZE THIS PRE-SCALED RPRIM.

C

```

      S=AREA/VOL
      DO 13 I=1,NROWS
        DO 12 J=1,NCOLS
          RPRIM(I,J)=S*RPRIM(I,J)
12     CONTINUE

```

```

13 CONTINUE
   RETURN
   END

```

```

C
C
C
C
C

```

```

FUNCTION CHISQR()

```

```

C.....CALCULATES THE CHI-SQUARE DIFFERENCE BETWEEN B*RN AND D.
C

```

```

COMMON /ASIZE/ NROWS,NCOLS
COMMON /COMPLEX/ RN,D,B,BF,RPRIM,CWK
COMMON /REAL/ CHISQR,Z
COMMON /DIMENSION/ D(56,32),B(56,32),BF(56,32)
COMMON /DAT/ D
COMMON /RD/ RPRIM,RN
COMMON /BEEM/ B,BF

```

```

C
C.....CALCULATE B*RN. FIRST, TO PROTECT RN, TRANSFER TO A BUFFER FILE.
C

```

```

CALL BUFF(RN,BF)

```

```

C
C.....NOW CALCULATE FOURIER TRANSFORM OF BF.
C

```

```

CALL FFT(BF,1)

```

```

C
C.....CONVOLVE BF WITH THE BEAM PROFILE.
C

```

```

CALL CONVOL(B,BF,BF)

```

```

C
C.....TAKE INVERSE TRANSFORM.
C

```

```

CALL FFT(BF,-1)

```

```

C
C.....NOW WE CAN COMPARE B*RN WITH D.
C

```

```

Z=0.

```

```

DO 2 I=1,NROWS
  DO 1 J=1,NCOLS
    Z=Z+(REAL(BF(I,J)-D(I,J)))**2
1    CONTINUE
2 CONTINUE
CHISQR=Z
RETURN
END

```

C
C
C
C
C

```

SUBROUTINE BUFF(PFILE,TFILE)
C....TRANSFERS FROM AN ARRAY WHICH IS TO BE SAVED, TO A TEMPORARY FILE
COMMON /ASIZE/ NROWS,NCOLS
COMPLEX PFILE(56,32),TFILE(56,32)
DO 2 I=1,NROWS
  DO 1 J=1,NCOLS
    TFILE(I,J)=PFILE(I,J)
1    CONTINUE
2 CONTINUE
RETURN
END

```

C
C
C
C
C

```

SUBROUTINE CONVOL(ARRAY1,ARRAY2,CONV)
C....MULTIPLIES TWO COMPLEX FOURIER TRANSFORMED ARRAYS TOGETHER TO
C....OBTAIN THE FOURIER TRANSFORM OF THE CONVOLUTION OF THE TWO ARRAYS.
COMMON /ASIZE/ NROWS,NCOLS
COMPLEX ARRAY1(56,32),ARRAY2(56,32),CONV(56,32)

```

C

```

DO 2 I=1,NROWS
  DO 1 J=1,NCOLS
    CONV(I,J)=ARRAY1(I,J)*ARRAY2(I,J)
1    CONTINUE

```

```
2 CONTINUE
   RETURN
   END
```

```
C
C
C
C
C
```

```
      SUBROUTINE FFT (ARRAY, KDIRN)
```

```
C.....CALCULATES THE FAST FOURIER TRANSFORM OF AN ARRAY.
```

```
C.....IF KDIRN = 1 , THE DIRECT TRANSFORM IS TAKEN.
```

```
C.....IF KDIRN = -1 , THE INVERSE TRANSFORM IS MADE.
```

```
      COMMON /ASIZE/NROWS,NCOLS
```

```
      COMMON /WKFL/IWK,RWK,CWK
```

```
      COMPLEX ARRAY(56,32),CWK(56)
```

```
      DIMENSION RWK(486),IWK(486)
```

```
C
```

```
      CALL FFT3D (ARRAY,NROWS,NCOLS,NROWS,NCOLS,1,KDIRN,IWK,RWK,CWK)
```

```
C
```

```
      RETURN
```

```
      END
```


References

- Batra, W., and Menten, K. M. 1985, *Ap. J. (Letters)*, **298**, L19.
- Bieging, J., Cohen, M., and Schwartz, P. 1984, *Ap. J.*, **282**, 699.
- Bok, B. J., and McCarthy, C. C. 1974, *A. J.*, **79**, 42.
- Cabrit, S., and Bertout, C. 1986, in *Protostars and Molecular Clouds*, eds. T. Montmerle and C. Bertout (Commissariat à l'Energie Atomique), 43.
- Calvet, N., Cantó, J., and Rodriguez, L. F. 1983, *Ap. J.*, **268**, 739.
- Castor, J., McCray, R., and Weaver, R. 1975, *Ap. J. (Letters)*, **200**, L107.
- Cohen, M., Bieging, J. H., and Schwartz, P. 1982, *Ap. J.*, **282**, 707.
- Cudworth, K. M. and Herbig, G. 1979, *Astron. J.*, **84**, 548.
- Draper, P. W., Warren-Smith, R. F., and Scarrott, S. M. 1985, *M. N. R. A. S.*, **216**, 7p.
- Edwards, S., Strom, S. E., Snell, R. L., Jarrett, T. H., Beichman, C. A., and Strom, K. M. 1986, *Ap. J. (Lett.)*, **307**, L65.
- Edwards, S., Cabrit, S., Strom, S. E., Heyer, I., Strom, K. M., and Anderson, E. 1987, *Ap. J.*, **321**, 473.
- Emerson, J. D., Harris, S., Jennings, R. E., Beichman, C. A., Baud, B., Beintema, D. H., Marsden, P. L., and Wesselius, P. R. 1984, *Ap. J. (Letters)*, **278**, L49.
- Freking, M. A., Langer, W. D., and Wilson, R. W. 1987, *Ap. J.*, **313**, 320.
- Fridlund, C. V. M., Sandquist, A., Nordh, H. L., and Oloffson, G. 1984, *Astr. Ap.*, **137**, L17.
- Goldsmith, P. F., Snell, R. L., Hemeon-Heyer, M., and Langer, W. D. 1984, *Ap. J.*, **286**, 599.
- Grasdalen, G. L., Hackwell, J. A., Gehrz, R. D., 1983. in *Topics in Information Processing in Astronomy and Optics* (Optical Society of America).
- Hayashi, S. S. 1987, private communication.
- Hayashi, S. S., Hayashi, M., Uchida, Y., Kaifu, N., and Shibata, K. 1987, in *IAU Symposium 115, Star Forming Regions*, ed. M. Peimbert and J. Jugku (Dordrecht: Reidel), p. 348.
- Herbig, G. H. 1968, *Ap. J.*, **152**, 439.
- Jarrett, T., and Edwards, S. 1988, preprint.

- Kaifu, N., Suzuki, S., Hasegawa, T., Morimoto, M., Inatani, J., Nagane, K., Miyazawa, K., Chikada, Y., Kanzawa, T., and Akabane, K. 1984, *Astron. Astrophys.*, **134**, 7.
- Keene, J., Davidson, J. A., Harper, D. A., Hildebrand, R. H., Jaffe, D. T., Loewenstein, R. F., Low, F. J., and Pernic, R. 1983, *Ap. J. (Letters)*, **274**, L43.
- Keene, J. B., and Masson, C. R. 1986, *BAAS*, **18**, 973.
- Kutner, M. L., and Ulich, B. L. 1981, *Ap. J.*, **250**, 341.
- Lada, C. J. 1985, *Ann. Rev. Astr. Astroph.*, **23**, 267.
- Langer, W. D., Frerking, M. A., and Wilson, R. W. 1986, *Ap. J. (Letters)*, **306**, L29.
- Levrault, R. 1985, unpublished PhD Dissertation, University of Texas, Austin.
- Moriarty-Schieven, G. H., Snell, R. L., Strom, S. E., and Grasdalen, G. L. 1987a, *Ap. J. (Letters)*, **317**, L95.
- Moriarty-Schieven, G. H., Snell, R. L., Strom, S. E., Schloerb, F. P., Strom, K. M., and Grasdalen, G. L. 1987b, *Ap. J.*, **319**, 742.
- Mundt, R., and Fried, J. W. 1983, *Ap. J. (Letters)*, **274**, L83.
- Narayan, R., and Nityananda, R. 1986, *Ann. Rev. Astr. Astroph.*, **24**, in press.
- Phillips, J. P., White, G. J., Ade, P. A. R., Cunningham, C. T., Richardson, K. J., Robson, E. I., and Watt, G. D. 1982, *Astr. Ap.*, **116**, 130.
- Predmore, C. R., Raisanen, A. V., Erickson, N. R., Goldsmith, P. F., and Marrero, J. L. R. 1984, *IEEE Trans. Microwave Theory Tech.*, **MTT-32**, 498.
- Pudritz, R. E., and Norman, C. A. 1983, *Ap. J.*, **274**, 677.
- Pudritz, R. E., and Norman, C. A. 1986, *Ap. J.*, **301**, 571.
- Rainey, R., White, G. J., Richardson, K. J., Griffen, M. J., Cronin, N. J., Monteiro, T. S., and Hilton, J. 1987, *Astr. Ap.*, **179**, 237.
- Sandell, G. 1987, private communication.
- Scoville, N. Z., Sargent, A. I., Sanders, D. B., Claussen, M. J., Masson, C. R., Lo, K. Y., and Phillips, T. G. 1986, in press.
- Shu, F. H., Lizano, S., and Najita, J. 1987, preprint.
- Snell, R. L. 1981, *Ap. J. Suppl.*, **45**, 121.
- Snell, R. L., Bally, J., Strom, S. E., and Strom, K. M. 1985, *Ap. J.*, **290**, 587.
- Snell, R. L., Loren, R. B., and Plambeck, R. L. 1980, *Ap. J. (Letters)*, **239**, L17.

- Snell, R. L., and Schloerb, F. P. 1985, *Ap. J.*, **285**, 490.
- Snell, R. L., Scoville, N. Z., Sanders, D. B., and Erickson, N. R. 1984, *Ap. J.*, **284**, 176.
- Strom, S. E., Strom, K. M., and Edwards, S. 1987, in *NATO Advanced Study Institute: Galactic and Extragalactic Star Formation*, ed. R. Pudritz and M. Fich, (Dordrecht: Reidel, Holland), in press.
- Strom, S. E., Strom, K. M., Grasdalen, G. L., Capps, R. W., and Thompson, D. A. 1985, *Astron. J.*, **90**, 2575.
- Tomita, Y., Saito, T., and Ohtani, H. 1979, *Pub. Astr. Soc. Japan*, **31**, 407.
- Torbett, M. V. 1984, *Ap. J.*, **278**, 318.
- Torrelles, J. M., Anglada, G., Rodríguez, L. F., Cantò, J., and Barral, J. F. 1987, *Astron. Astrophys.*, **177**, 171.
- Uchida, Y., Kaifu, N., Shibata, K., Hayashi, S. S., and Hasagawa, T. 1987, in *IAU Symposium 115, Star Forming Regions*, ed. M. Peimbert and J. Jugku (Dordrecht: Reidel), p. 287.
- Uchida, Y., and Shibata, K. 1985, *Publ. Astron. Soc. Japan*, **37**, 515.
- Vrba, F. J., Luginbuhl, C. B., Strom, S. E., Strom, K. M., and Heyer, M. H. 1987, *A. J.*, **92**, 633.
- Willingdale, R., 1981. *M. N. R. A. S.*, **194**, 359.

PHYSICAL SCIENCES
LIBRARY

DEC 16 1988

ACME
BOOKBINDING CO., INC.

DEC 16 1988

100 CAMBRIDGE STREET
CHARLESTOWN, MASS.

